# ELECTROSTATIC CONTROL OF THE ANOMALOUS HALL EFFECT IN $SrRuO_3$

HÉLÈNE SPRING

*A thesis submitted in partial fulfillment of the requirements for the degree of Master of Science in Applied Physics*
Quantum Nanoscience
Applied Physics
Delft University of Technology

May 23, 2019

SUPERVISORS:
Dr. Andrea Caviglia
MSc. Thierry van Thiel

COMMITTEE MEMBERS:
Dr. Andrea Caviglia
Dr. Anton Akhmerov
Dr. Toeno van der Sar

# ABSTRACT

In this study, ultrathin films of the itinerant 4*d* ferromagnet $SrRuO_3$ were epitaxially deposited on $SrTiO_3$ and capped with a thin $LaAlO_3$ layer. Top gates and a dielectric layer were patterned onto contacted films and magnetotransport properties were characterized at low temperatures as a function of top gate voltage. A particular focus was placed on the anomalous Hall resistivity. The magnitude of the Hall signal and the sheet resistance were shown to vary with top gate voltage. In particular, the anomalous Hall loops were compared to numerical tight-binding models. The model is proposed as an alternate explanation to the skyrmion picture and as a complement to the two-channel phenomenological model put forth to explain the unusual low-temperature anomalous signal of ultrathin $SrRuO_3$ . Model predictions were found to be valid at low temperatures in semiconducting *Ru*-deficient $SrRuO_3$ films.

# CONTENTS

---

# LIST OF FIGURES

# LIST OF TABLES

---

# ACRONYMS

| | |
|---|---|
| **OHE** | ordinary Hall effect |
| **AHE** | anomalous Hall effect |
| **QHE** | quantum Hall effect |
| **QAHE** | quantum anomalous Hall effect |
| **SOC** | spin-orbit coupling |
| **k-space** | (crystal) momentum space |
| **TRS** | time-reversal symmetry |
| **IS** | inversion symmetry |
| **ZBR** | Brillouin zone |
| **CN** | Chern number |
| **DOS** | density of states |
| **PDOS** | partial density of states |
| **LL** | Landau level |
| **PLD** | pulsed laser deposition |
| **ML** | monolayer |
| **TNT** | topologically non-trivial |
| **AFM** | atomic force microscopy |
| **XRD** | x-ray diffraction |
| **RHEED** | reflection high-energy electron diffraction |
| **EBL** | electron-beam lithography |
| **PMMA** | polymethyl methacrylate |
| **PCB** | printed circuit board |
| **DFT** | density functional theory |

**LSDA+U** local-spin-density approximation + Coulomb repulsion

**SQUID** superconducting quantum interference device

**DMI** Dzyaloshinskii-Moriya interaction

# Part I

# A THEORETICAL INTRODUCTION

# 1

# INTRODUCTION

In condensed matter systems, collective behavior of a lattice and its surroundings can lead to the manifestation of fascinating physical phenomena like quasiparticles. These excitations follow similar (but not identical) rules as their particle counterparts at different energy scales [4]. For example, the predicted energy of a magnetic monopole is estimated at about $10^{25}$ eV, whereas an emergent magnetic monopole exists in the 1 eV range [41]. As such, normally high-energy particles can be experimentally studied, albeit in a different form, at low energetic cost in lattice systems. The presence of such emergent phenomena are symptomatic of complex behavior; emergent monopoles can be found in the reciprocal space of ferromagnetic materials as a consequence of band topology and broken time-reversal symmetry. The intrinsic anomalous Hall effect arises from the presence of these magnetic monopoles [24], and can be measured in magnetotransport experiments.

$SrRuO_3$ , a transition-metal oxide with itinerant ferromagnetism, hosts an anomalous Hall effect (AHE) [36]. It has moderate electrical conductivity, [56]. Highly conductive ferromagnets typically has a dominant extrinsic contribution to the AHE stemming from disorder, whereas moderately conductive ferromagnets like $SrRuO_3$ , being labeled a 'bad metal', has a larger contribution from the intrinsic AHE [63].

Transition-metal oxides (TMOs) are a material class that exhibits rich and exotic behavior, due in no small part to their degrees of freedom being strongly interconnected; in $SrRuO_3$ alone, lattice strain affects magnetic and conducting properties [66], and the film thickness affects the magnetic moment [81] among other things. The reason underlying the behavior of TMOs lies in the transition metal atoms transferring their *s* electrons to the oxygen ions, leaving the strongly correlated *d* electrons to dictate transport and magnetic properties. Further, the effects experienced by the electrons like spin-orbit interaction, crystal field splitting and Coulomb repulsion are on the same energy scale, leading to a wide variety in behavior between TMOs, despite their similarity in structure and chemistry [13].

Creating layered epitaxial TMO structures opens a door to a new and still not fully explored range of physics. Interfacing $SrRuO_3$ with other transition-metal oxides was revealed to affect the shape of its AHE signal into unconventional shapes [45]. In recent years, the unusual behaviour of the anomalous Hall hysteresis loops of ultrathin $SrRuO_3$ films have raised a debate as to their origin. The topological Hall effect [75] [62] [64] [69] and coexisting uncoupled ferromagnetic domains [45] are postulated as possible explanations.

In this thesis, a tight-binding model for $SrRuO_3$ adapted from Ref.[45] is studied numerically and presented as an additional avenue for explanation of the exotic features of the AHE signal at $SrRuO_3$ interfaces. It posits that the low-energy band topology of $SrRuO_3$ can be used to explain the AHE signal at low temperatures, and is compared to low-temperature magnetotransport data of semiconducting $SrRuO_3$ in $SrTiO_3$ -$SrRuO_3$ -$LaAlO_3$ devices.

The structure of this thesis is as follows. In chapter 2, a literature review on the background information on the crystallographic, electronic and magnetic properties of $SrRuO_3$ is exposited, and an overview of the ordinary(OHE) and anomalous Hall effects (AHE), as well as a derivation of the quantal origin of the intrinsic AHE are given. Chapter 3 introduces the experimental techniques used for device synthesis and measurement. Chapter 4 reviews the methods used in obtaining and exploiting numerical models for $SrRuO_3$ monolayers, as well as $SrRuO_3$ -$SrTiO_3$ and $SrRuO_3$ -$SrIrO_3$ interfaces, with the results of the numerical analysis given in chapter 5. Experimental results are presented in chapter 6, and analysis is separated into quantitative and qualitative sections. In the qualitative section, the AHE signal is directly compared to the results of the numerical simulations. Concluding remarks and an outlook for future numerical models and transport experiments are given in Chapter 7.

# THEORY

## 2.1 COMPLEX OXIDES

### 2.1.1 *Perovskites*

A simple oxide is a family of materials that involves one element and oxygen together, in the form $A_xO_y$. The complex oxide family hosts materials that are composed of at least two elements and oxygen, in various forms, such as $AB_2O_4$ (spinel structure) or $ABO_3$ (perovskite structure) [27].

Due to the greater possibility of structural variety in complex oxides, they are bountiful grounds for exotic condensed matter phenomena. The interplay between competing energy scales like spin-orbit coupling and electron-electron interaction, and the lattice and electronic structure make them highly intriguing experimental subjects.

An example of perovskite structure $ABO_3$ can be seen in Fig.1. As opposed to ilmenite-related structures, also of the form $ABO_3$, the $A$, $B$ atoms in perovskites are always cations [27]. More complex combinations of elements have been discovered to

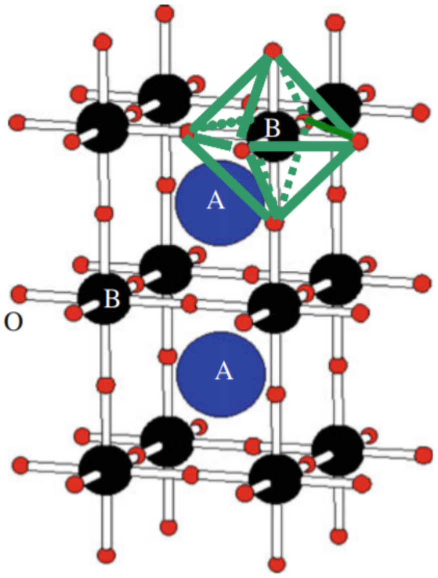

Figure 1: Perovskite structure of the Pm-3m (simple cubic structure) space group. A $BO_6$ octahedron is shown in green [3].

have perovskite structure (eg. $La(Ni_{1/2}Nb_{1/2})O_3$) [27], but the material which interests us, $SrRuO_3$ , is of the typical $ABO_3$ form.

The diversity of properties that exists within the perovskite structure group is astounding. For example, $SrRuO_3$ exhibits ferromagnetism, $BaTiO_3$ ferroelectricity, and $BaPb_{1-x}Bi_xO_3$ superconductivity [3]. These properties arise from the complex parameter interplay forged by the perovskite structure, and interesting emergent phenomena can be expected from most, if not all of these materials.

### 2.1.2 $SrRuO_3$

The focus of this work will be on thin films of $SrRuO_3$ . It exhibits itinerant ferromagnetism, with a magnetic moment of approximately $1.5\mu_B$ per $Ru$ atom [73]. The ferromagnetism is of a $4d$ nature, due to presence of the $4d$ $Ru$ bands at the Fermi level (cf. Fig.3). $4d$ ferromagnetism is quite rare [73], and has earned $SrRuO_3$ some interest, along with its promising applications in devices [53]. It has also gained interest due to its unusual anomalous Hall effect behavior (see section 2.3). This unusual behavior will be the focal point of our study.

## 2.2 $SrRuO_3$: BULK AND EPITAXIAL THIN FILM PROPERTIES

In this section, we lay the foundation for characterizing $SrRuO_3$ and understanding its base properties, as both a bulk and thin film sample.

### 2.2.1 Structural properties

#### 2.2.1.1 Lattice structure

$SrRuO_3$ is an $ABO_3$ perovskite compound. It has orthorhombic symmetry at room temperature. This structure is due to the $A-O$ bond being more than twice as short as the $B-O$ bond length, resulting in rotations of the $BO_6$ octahedra. In $SrRuO_3$ , the $RuO_6$ octahedral rotations lead to an orthorhombic structure with lattice parameters a=5.5670 Å, b=5.5304 Å, and c=7.8446 Å. This structure can alternatively be described as a pseudo-cubic perovskite structure, with a pseudocubic lattice constant a=3.93 Å, which we will associate with a cubic $ABO_3$ perovskite [56]. $SrRuO_3$ is structurally compatible with many complex oxides, making it a popular electrode in complex oxide-based devices [59]. As we will see, however, some of its properties are dependent on epitaxial strain, as it has a direct effect on the octahedral rotations.

The degree of orthorhombic distortion decreases with increasing temperature. The symmetry crosses over to tetragonal at 547 °C, then to cubic at 677 °C. These values are valid for bulk $SrRuO_3$ , but not for thin films. The reason for this is that the thin films are subjected to lattice mismatch with a substrate that brings about epitaxial strain. As

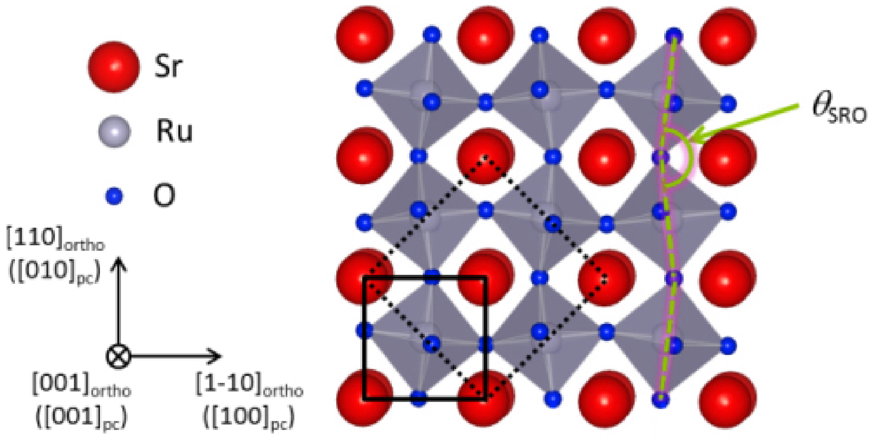

Figure 2: $SrRuO_3$ orthorhombic phase symmetry. The rotations of the $RuO_6$ octahedra are clearly visible. The rotation angle is given by $\theta_{SRO}$ [33].

such, transition temperatures being directly dependent on lattice strain, we expect to see differences for thin films [56].

Strain-induced octahedral rotations in $SrRuO_3$ are also linked to lowered longitudinal resistivity [50]

### 2.2.1.2 *Electronic structure*

Since we are most interested in understanding the properties of $SrRuO_3$ via its transport behavior, knowledge of its electronic structure is of capital importance. Understanding what bands are at the Fermi level can help explain the nature of the charge carriers that we expect to see in transport measurements. Koster et al [56] provide a schematic representation of what the orbital electronic structure of any $ABO_3$ perovskite resembles in Fig.3. We observe from this that $SrRuO_3$ is marked by a 4d $t_{2g}$ character from the $Ru$. The $Ru$ octahedral rotations create an electrostatic environment that breaks the crystal environment symmetry in such a way that the fivefold degenerate $Ru$ d bands are split into two groups, d($e_g$) and d($t_g$) levels [56]. The Fermi level lies at two-thirds occupation of the $d(t_g)$ bands.

We can seek theoretical confirmation for $SrRuO_3$ of the simple orbital picture we saw in Fig.3. In 1996, Allen et al. [31] used the self-consistent linear muffin-tin orbital (LMTO) method to glean some information concerning the band structure of $SrRuO_3$ . They calculate the electronic density of states (DOS) for an orthorhombic structure, pictured in Fig.4. A 1 eV Stoner splitting can be seen close to the Fermi level [34]. This allows us to put Fig.3 to the test. Fig.4 shows the same oxygen p orbitals from -8 to -3 eV, followed by a gap of approximately 1 eV and bands of primarily $Ru$ 4d parentage, which lie close to the Fermi level, along with orbitals of oxygen p origin. Above the Fermi level are the $Ru$ s, e orbitals and the $Sr$ orbitals. Allen et al. find a

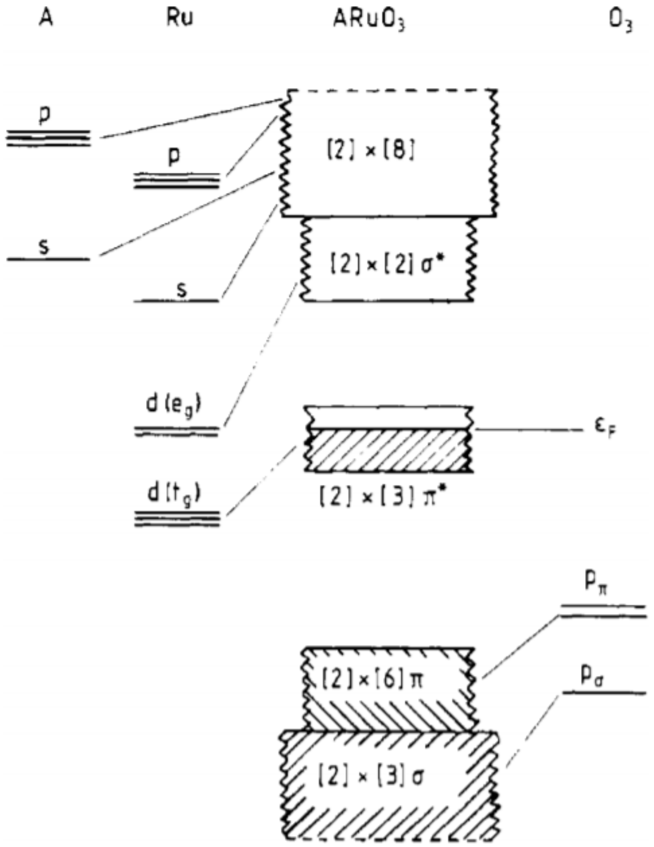

Figure 3: A generic orbital model for an $ABO_3$ perovskite, like $SrRuO_3$ . The factor 2 in each orbital block accounts for electron spin [56].

$1.45\mu_B$ magnetic moment per $Ru$ atom. The moment contributions from the $Sr$ and $O$ atoms are an order of magnitude smaller [31].

In the same year as Allen et al. above, Singh et al. [73] used a different first-principle calculation method (the linearized augmented plane-wave method, or LAPW) and found similar results. Their calculation for the orthorhombic lattice, spin-resolved DOS closely resembles Fig.4, and is pictured in Fig.5. The Stoner splitting that could faintly be noticed in Fig.4 is quite clear here.

The calculated moment per $Ru$ is $1.59\mu_B$ , similar to the result obtained by Allen et al. for orthorhombic $SrRuO_3$ , close to the modern accepted value [57].

Investigating the partial density of states (PDOS) of the 4$d$ electrons in $SrRuO_3$ could give some insights on its magnetic behavior, which we will see in greater detail in the next subsection. Kim and Min [20], using Density Functional Theory (DFT) and Dynamical Mean-Field Theory (DMFT), plot the PDOS of the 4$d$ electrons in Fig.6. We note that the high-spin states are less populated than the low-spin states, indicating

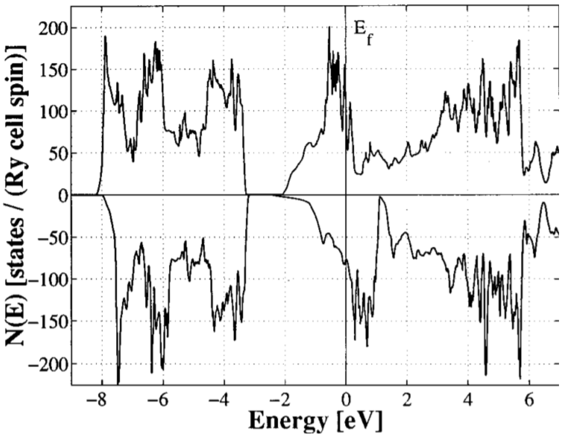

Figure 4: Spin-resolved DOS for $SrRuO_3$ : majority spin is plotted upward and minority spin downward. The calculation was performed for four formula units [31].

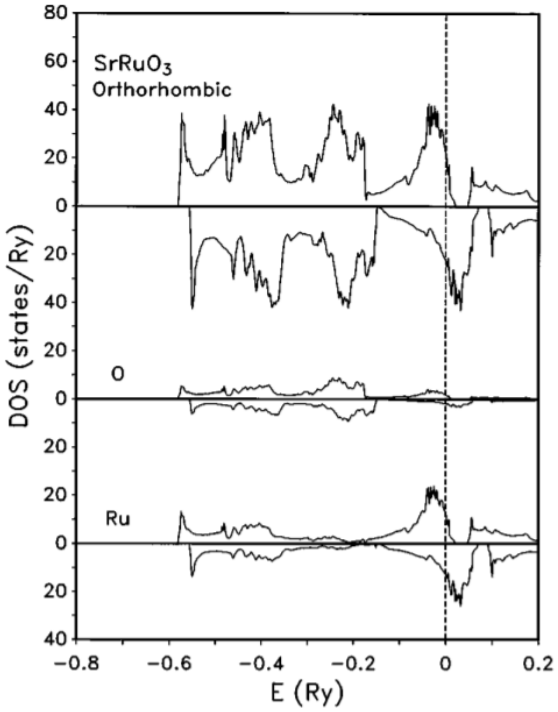

Figure 5: DOS, with majority spin plotted upwards, per formula unit. Top: $SrRuO_3$ DOS. The gap is closed, but the Fermi level states remain similar to Fig.4. Middle: the oxygen contribution. Bottom: the ruthenium contribution [73].

minority-band ferromagnetism, and that the $e_{2g}$ orbitals have a lower occupancy than the $t_{2g}$ orbitals.

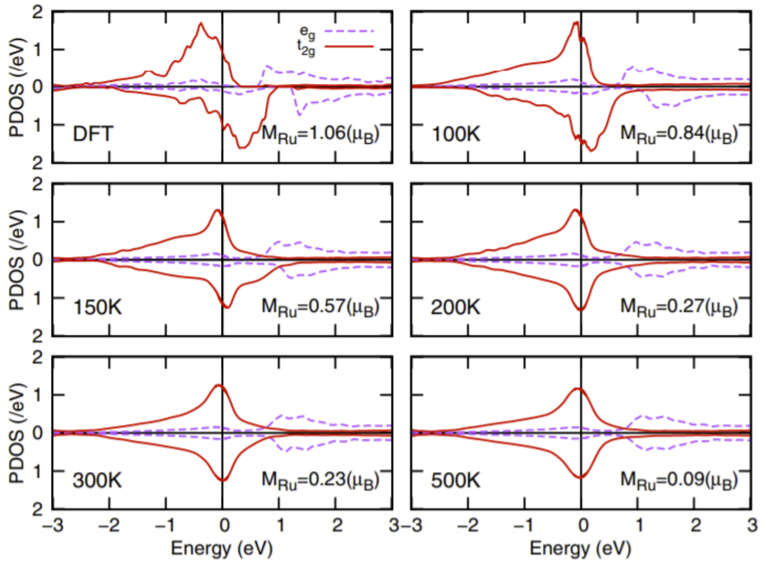

Figure 6: PDOS of the *Ru* 4*d* electrons, calculated with DFT and DFT+DMFT at different temperatures. Majority spin is plotted upwards, minority spin downwards [20].

### 2.2.2 *Magnetism*

Bulk $SrRuO_3$ is ferromagnetic, and undergoes a phase transition at a Curie temperature of about 160 K [59]. The ferromagnetism in $SrRuO_3$ is called itinerant, because the electrons whose spins are responsible for the ferromagnetic state are also the electrons involved in conduction [30].

Two models exist for the (anti-) ferromagnetism of transition metals: the itinerant and localized models. *d* electrons have been ruled to be itinerant [29], but the question of the existence of local moment contribution in *d* metals remains. Two limits exist in itinerant ferromagnetism. The weak ferromagnetic limit, where Stoner theory is obeyed below the critical temperature, and the magnetic susceptibility above this temperature is attributed to spin fluctuations in momentum space [25]. The local moment limit obeys Heisenberg theory, and the susceptibility above the critical temperature is explained with localized spins in real space. $SrRuO_3$ follows Stoner behavior below the critical temperature, and has residual local moments at higher temperatures: $SrRuO_3$ has a dual nature of both local and weak moment limits [20]. $SrRuO_3$ is a minority-band itinerant ferromagnet, which means that the spin polarization of the charge carriers at the Fermi surface are, on average, in the direction opposite to its magnetization [56].

$SrRuO_3$ has a similar $q$ value ($\sim$ 1.3) to elemental ferromagnets iron, nickel and cobalt. The $q$ value is a measure of the itinerancy of the magnetism, and is quantified as the ratio of the high-temperature moment and the zero-temperature saturated magnetization . A $1-2$ $q$ value indicates strong itinerancy [56]. Contrary to ”good” metallic $3d$ elemental ferromagnets, $SrRuO_3$ demonstrates ”bad” metallic behavior [54].

The magnetic moment of $SrRuO_3$ is of $\sim 1.6\mu_B$, the $Ru$ atom making up much of this contribution [57].

Tertagonal $SrRuO_3$ exhibits uniaxial magnetocrystalline anisotropy. It has been shown that the easy axis is close to the b axis, independently of the orientation of the orthorhombic unit cell relative to the $SrTiO_3$ substrate [56]. The angle between the easy axis and the normal to the film was also shown to vary with temperature, from 30°at low temperatures to about 45°close to the Curie temperature [54].

Contradictory results have been published about the magnetic easy axis orientation. Despite (or because of) this confusion, Kolesnik et al. [55] suggest a definitive answer: epitaxial, single-domain $SrRuO_3$ thin films have a magnetic easy axis which lies in the (001) plane and tilts away from the normal to the film by 22-26°, its direction lying between the [110] and [010] axes. For visual clarity, these faces and directions are shown in Fig.7. For intertwinned, multidomain $SrRuO_3$ films the easy axis were found to draw closer to the normal of the film as a collective result from all the domains [55].

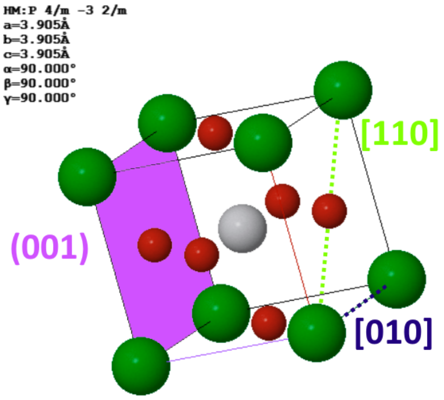

Figure 7: (001), [110] and [010] made clear on a $SrTiO_3$ unit cell. Image made using the University of Cádiz TEM-UCA servers.

Magnetic materials have a tendency to subdivide into several magnetic domains in zero applied field in order to reduce their magnetostatic energy. In $SrRuO_3$ , this tendency leads to the formation of stripe-like domain walls separated by about 200 nm. The domain walls are Bloch walls when the applied field is in the plane of the domain wall, and of Néel type at perpendicular alignment [70].

In magnetic materials, in addition to the ordinary Hall effect (OHE), stemming from an external magnetic field, we also can observe the anomalous Hall effect (AHE), which depends on the magnetization of the material [56]. A complete explanation of the AHE can be found in section 2.3. The AHE observed in ferromagnetic materials is closely related to magnetic monopoles in momentum space [41], as we will see in section 2.5.

## 2.3 THE HALL EFFECT IN $SrRuO_3$

In order to understand the origin of the AHE in $SrRuO_3$ , we first need to understand what the classical Hall effect is, as well as its quantum counterparts.

### 2.3.1 *The Hall effect*

In 1878, Edwin Hall read contradictory statements in Maxwell's *Electricity and Magnetism* and Edlund's "Unipolar induction". The former asserted that currents, after the abeyance of transient induction currents, felt no force due to a constant magnetic field; the latter stated that a stationary magnet affected a current in the same fashion a moving magnet may affect a conductor. Hall reasoned that if a current were affected by a magnet, then it would be drawn to one side of the conductor, thereby increasing the resistance in the wire. At the time, some supposed electricity to be an incompressible fluid, and thus could not be pushed to one side of a conductor. However, if a magnet could act upon a current, then the 'electric pressure' on one side of the conductor could still differ from the other, due to the incompressible electric liquid 'pressing' on one of the sides. As such, Hall measured the potential difference between two sides of the conductor. This voltage drop was directly proportional to the product of the current and of the applied magnetic field [8].

The effect of magnetic fields on conduction electrons in materials is given by the equation of the Lorentz force:

$$\boldsymbol{F} = q\boldsymbol{E} + q\boldsymbol{v} \times \boldsymbol{B} \tag{1}$$

in which q represents the charge of a particle, $\boldsymbol{E}$ and $\boldsymbol{B}$ applied external electric and magnetic fields, and $\boldsymbol{v}$ the velocity of the particle. As is apparent, a charged particle will feel a force on the same axis as the electric field, but transverse to any magnetic field. This is what led to a difference in potential drop in Hall's experiment, as can be seen in Fig.8. Charge is deviated by the transverse magnetic field (in orange), and we see charge separation occur in the conductor, leading to the establishment of a transverse electric field (in blue); this voltage $V_H$ is given as

$$V_H = \frac{IB}{nte} \tag{2}$$

where t is the thickness of the material in the direction of the magnetic field, I is the current, and n is the charge carrier density.

The phenomenon known as the (classical) Hall effect is thus the production of a voltage difference across an electrical conductor due to the effect of a magnetic field perpendicular to the electric current inside the conductor.

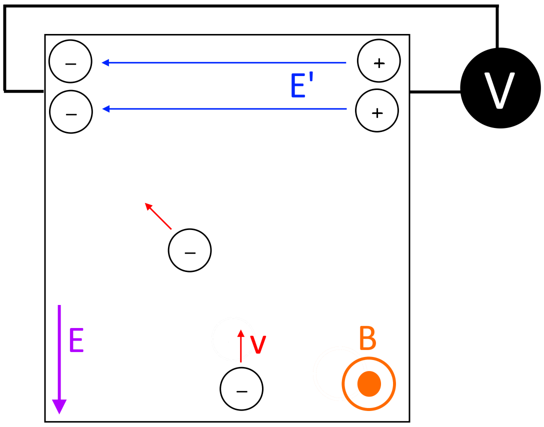

Figure 8: A schematic representation of charge dynamics in the Hall effect.

### 2.3.2 *The anomalous Hall effect*

After the discovery of the ordinary Hall effect, a Hall response ten times larger than in normal metals was observed in ferromagnetic conductors [58]. This new discovery became known as the anomalous Hall effect (AHE). It remained shrouded in mystery for a long time, since the AHE mixes quantal and topological concepts that have come into use only fairly recently [63].

For the ordinary Hall effect, transverse resistance increases linearly with the magnetic field,

$$R^{o}_{xy} = R_H B,\ R_H = \frac{E_y}{j_x B_z} = -\frac{1}{ne} \tag{3}$$

where $R_H$ is the Hall coefficient, $j_x$ the current density and $E_y$ the transverse induced electric field [65]. For the AHE, a rapid increase in transverse resistance at low applied fields followed by a saturation towards a certain value was observed. This value was found to be roughly proportional to the magnetization in the sample, thus the AHE was linked to spontaneous magnetization in the material:

$$R^{a}_{xy} = R_s M \tag{4}$$

where $M$ is the magnetization and $R_s$ is the anomalous Hall coefficient [65]. In ferromagnetic conductors, a Hall effect is present in the absence of an applied magnetic field, as shown in Fig.9. The same separation of charge occurs in Fig.9b) as in 9a), the difference being the fact that for the AHE no magnetic field is required for initial charge separation. The fact that the transverse resistivity is proportional to magnetization means that the $R - H$ plots display hysteresis and saturation behavior, like $M - H$ curves in ferromagnets:

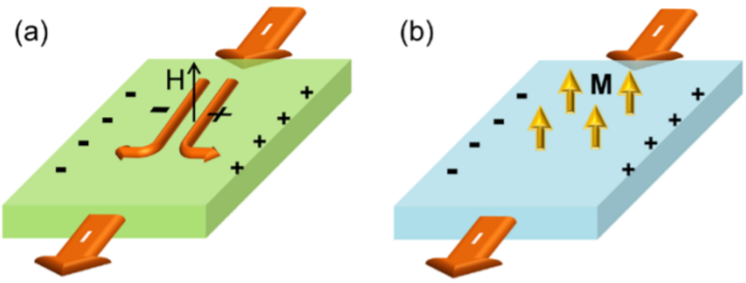

Figure 9: (a) The Hall effect, (b) the anomalous Hall effect [5].

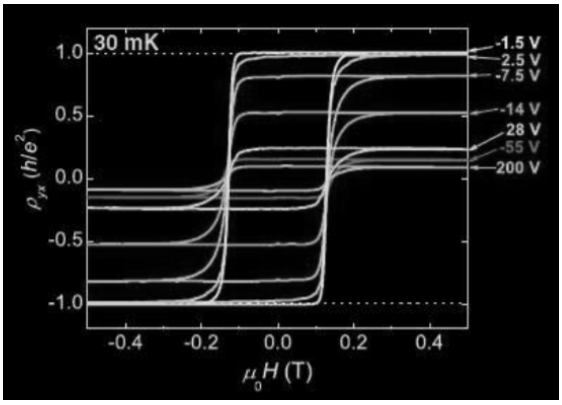

Figure 10: The Hall resistance as a function of external magnetic field for different gate voltages in $Cr$-doped $(Bi, Sb)_2Te_3$ films [58].

Although the apparent symmetry between Eq. 3 and Eq. 4 might indicate a straightforward dependence of $R^a_{xy}$ on $M$, the anomalous Hall coefficient has subtle dependencies on a collection of material-specific parameters [63], which requires more careful study than the simple carrier concentration dependence of $R^o_{xy}$.

Now that we have familiarized ourselves with the AHE, a connection to $SrRuO_3$ can be established via considerations concerning a certain geometrical phase: the Berry phase. This concept will be explored in Section2.5.

## 2.4 ANOMALOUS TRANSPORT IN $SrRuO_3$

The AHE in $SrRuO_3$ has proven to be a source of intrigue. It is characterized by sign changes of the anomalous signal. The sign has been shown to be affected by temperature as well as magnetization, as pictured in Fig.11. This phenomenon is widely documented for $SrRuO_3$ films [49] [61].

The anomalous resistivity of $SrRuO_3$ as a function of magnetic field demonstrates hysteretic behavior as expected (see Section 2.3.2). However, several domain switches

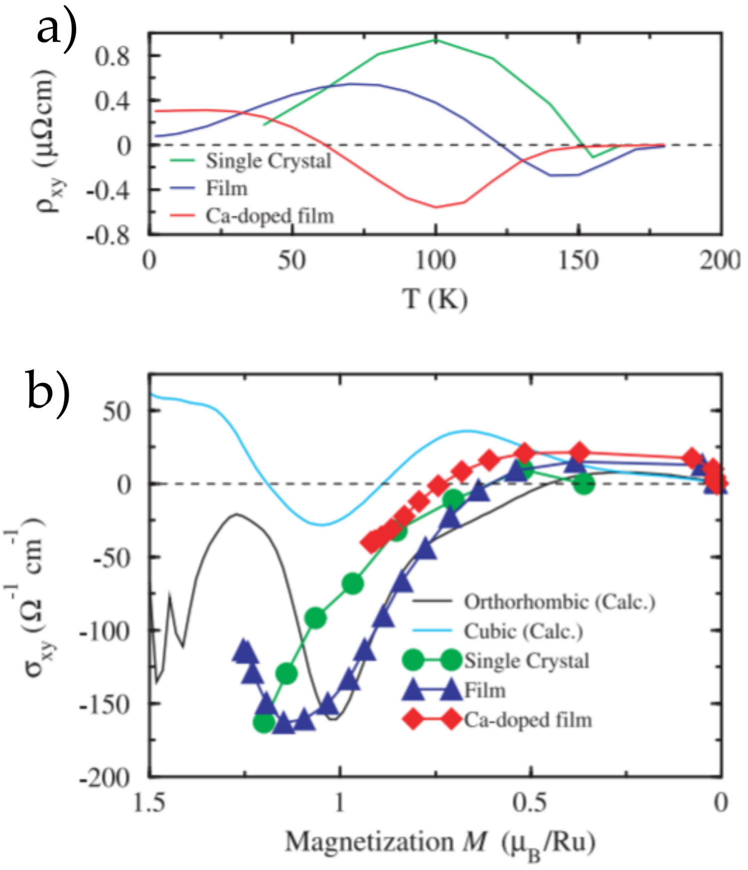

Figure 11: a) Transverse resistivity as a function of temperature and b) transverse conductivity as a function of magnetization of $SrRuO_3$ [41].

are visible, depending on film thickness [51], substrate orientation [47], and temperature [51]. This magnetic domain switch phenomenon is pushed to the extreme in ultrathin $SrRuO_3$ films. The sensitivity of the anomalous signal to changes in magnetization leads to sharp signal changes between magnetic domains, which can add up to a surprising result. Sohn et al. [75] ascribe the strange behavior in Fig.13 to the presence of magnetic skyrmions, spin arrangements as depicted in Fig.14. These skyrmions would arise from the intrinsic ferromagnetism of $SrRuO_3$ and be stabilized by Dzyaloshinskii-Moriya interactions (DMI) between $SrRuO_3$ and the vacuum [75]. Matsuno et al. [62] study the $SrRuO_3$ -$SrIrO_3$ interface and also claim to see skyrmion formation:

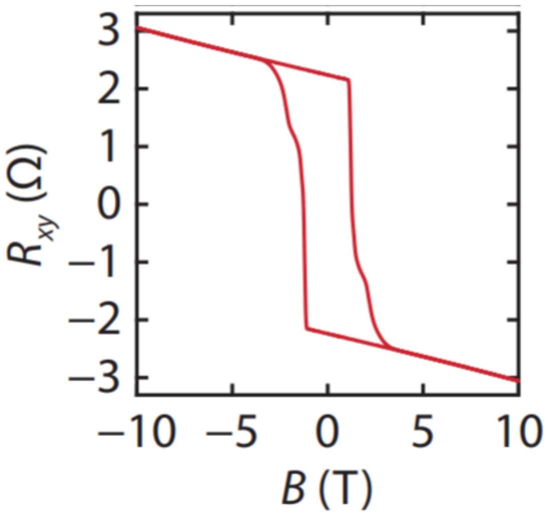

Figure 12: AHE resistivity as a function of magnetic field for a bilayer $SrRuO_3$ film at 10K [7].

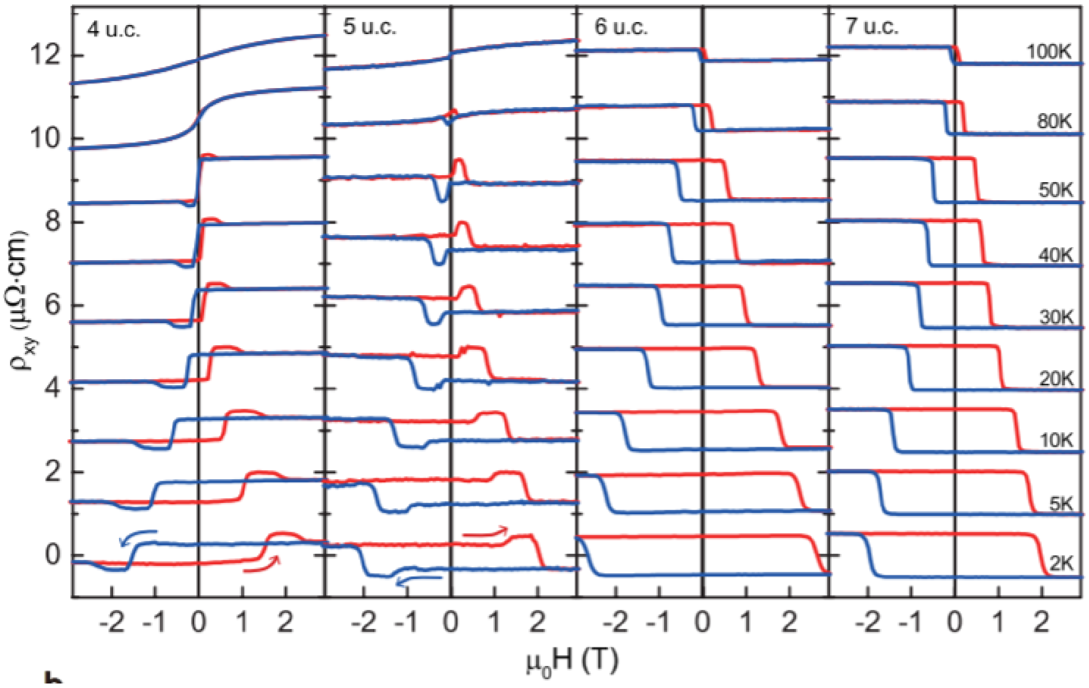

Figure 13: AHE resistivity as a function of film thickness, temperature, and magnetic field for ultrathin $SrRuO_3$ films. OHE is subtracted [75].

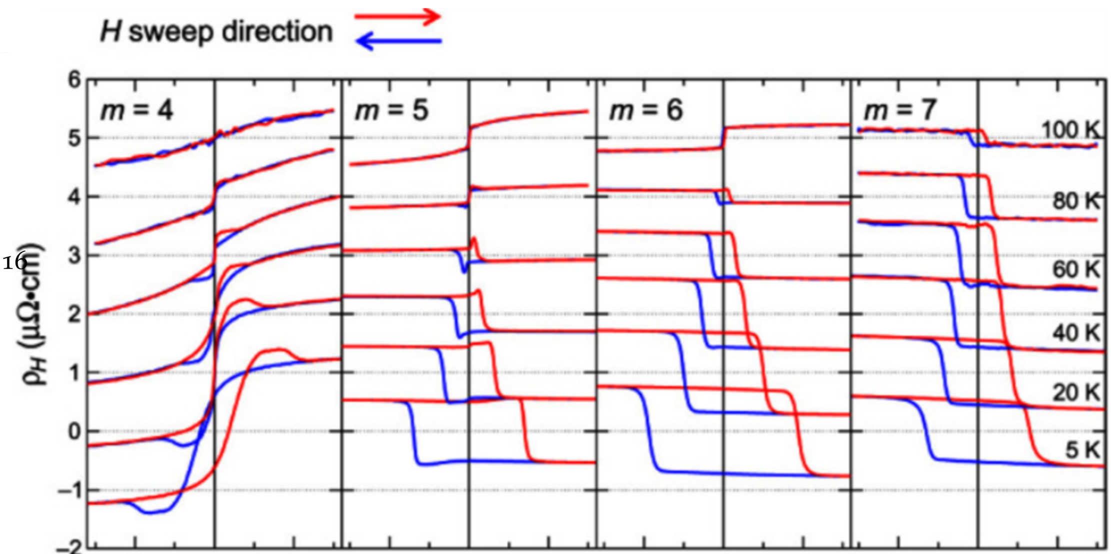

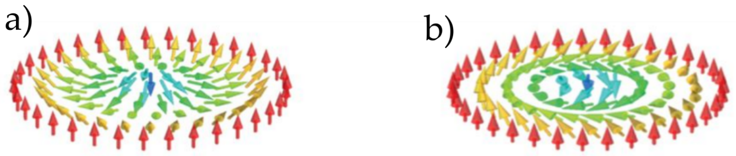

Figure 14: a) Néel-type and b) Bloch-type skyrmions [42] .

In this case, the skyrmions are ascribed to DMI between the $SrIrO_3$ -$SrRuO_3$ interface.

The relevance of skyrmions to the anomalous signal is their involvement in the topological Hall effect (THE). The skyrmions, as a spatially-varying magnetization, add a contribution to the Hall signal. This contribution is strictly dependent on the topology of the skyrmion magnetic texture, hence the name.

However, Groenendijk et al. [45] argue that the skyrmion picture is unlikely [86] and the shape of the Hall loops can also be explained via two co-existing AHE contributions, as pictured in Fig.16. The signal is explained as arising from two uncoupled ferromagnetic domains. Further arguments on the discontinuity of the coercivity give this phenomenological model an advantage over the skyrmion theory of $SrRuO_3$ [45]. $SrRuO_3$ thus proves to be a rich playground for condensed matter phenomena, and in order to understand the physical principles at play, it is highly relevant to delve into the phase responsible for the intrinsic AHE: the Berry phase.

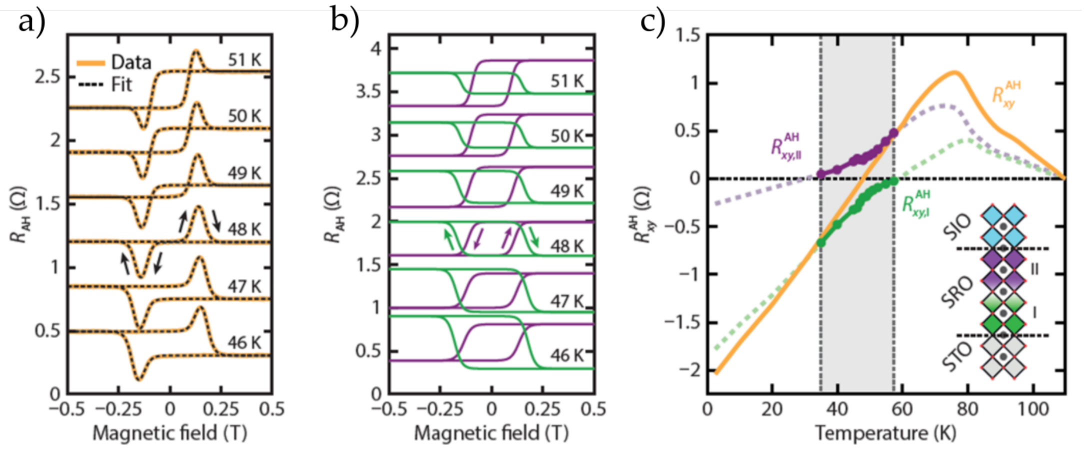

Figure 16: Hall loop data and fits for a $SrTiO_3$ -$SrRuO_3$ -$SrIrO_3$ sample. a) Data and fits of OHE-subtracted Hall loops, b) deconstruction into two AHE signals of opposite sign, c) projected AHE contributions as a function of temperature [45].

## 2.5 BERRY PHASE THEORY OF $SrRuO_3$ I

This section will contain comprehensive steps, through which the origin of the AHE in $SrRuO_3$ should become clear. This connection will be further explored with the help of topological concepts in section 2.6.

The AHE has been observed in ferromagnets like $SrRuO_3$ , and the mechanism that lies at its origin has been a widely-discussed topic. Extrinsic vs. intrinsic origins are debated, as pictured in Fig.17. Skew-spin scattering, wherein electrons with different spins scatter to different sides of impurities in the material, and mechanisms by which electrons act as if performing a side-jump have been theorized extrinsic explanations. These models rely on a perturbative expansion of the SOC and the magnetization to the Hamiltonian [41].

Another approach to the AHE is to consider intrinsic contributions, which would remove the reliance on disorder. Karplus and Luttinger, in 1954, showed that a ferromagnet in an external electric field saw its electrons acquire an additional contribution to their group velocity, perpendicular to the electric field. There were clear parallels to the Hall effect, and since no disorder was involved, it had to rely purely on the band structure. The anomalous velocity that these considerations yielded depended solely on the evolution of the Bloch wave packets in crystal momentum space under the influence of the electric field. If the material in question is a conducting ferromagnet, the sum of all the anomalous contributions can be nonzero [63]. For those familiar with the Berry phase, Karplus and Luttinger's predictions clearly anticipate the link between it and the intrinsic AHE. This theory was left to the wayside for several decades, until there was a realization that the transverse conductivity can be written as the integral of a momentum space (k-space) gauge field over occupied electronic states in k-space [41]. This lead to the recognition of the importance of a geometric quantum phase, named the Berry phase, in intrinsic AHE theory.

In order to understand the physical Berry phase, it is helpful to first picture a simple geometrical phase by considering a vector pointing out of a surface (cf. Fig.18). The vector is shifted along the surface in such a way that the angle between the two remains constant. If the surface is completely flat, then any closed loop along it would lead to the perfect spatial superposition of the vector with itself. However, as we can note in Fig.18, intrinsic curvature present in the surface introduces an anholonomy angle ($\alpha$ in the figure), which measures the degree to which the final and initial vectors differ from each other [23]. An open cylinder or a torus, for example, have no intrinsic curvature, as they can be cut into flat rectangles; a sphere cannot, as it has a constant intrinsic curvature.

Its value is a function of the shape and position in parameter space of the closed loop. This makes it difficult to say if a loop is small enough to appropriately estimate of the curvature of the parameter space manifold.

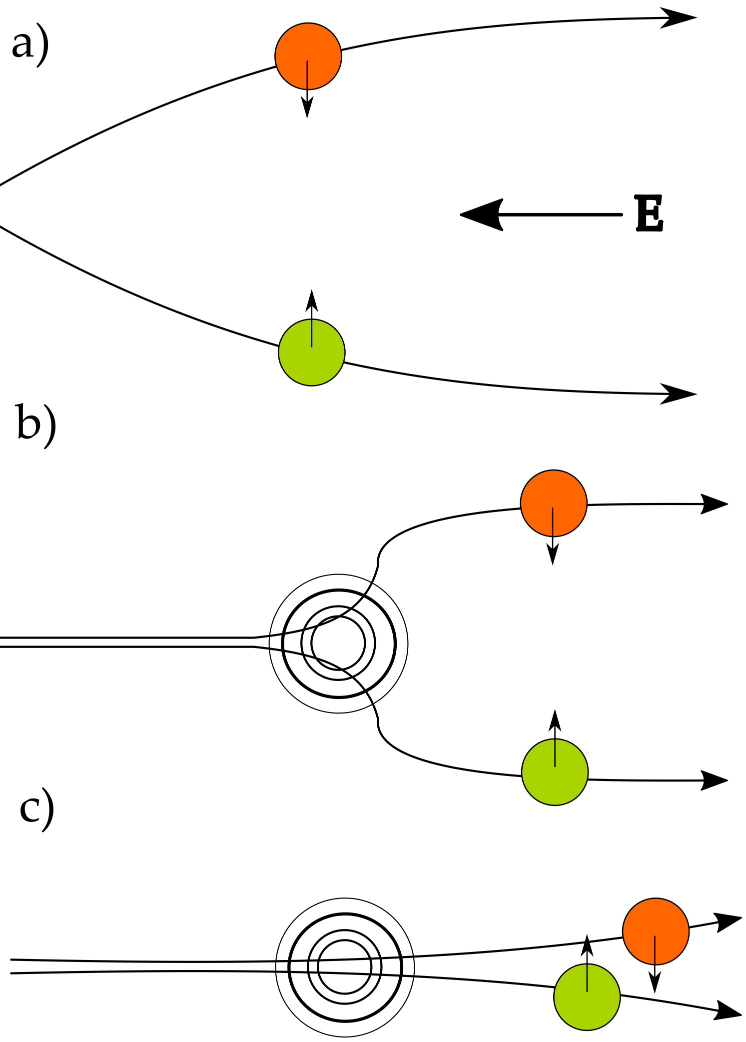

Figure 17: Theorized contributions to the AHE; a) intrinsic contribution, demonstrating deviation transverse to an applied electric field, b) side jump mechanism and c) skew-scattering mechanism [63].

The considerations made on this geometric angle can be extended to quantum mechanics: a quantum state may not return to its original value after one adiabatic cycle in parameter space, even once the dynamical phase is taken into account. One may think to adjust the basis of the system to account for this lack of correspondence, but Berry argued that this phase may not always be removable [24].

We consider a system of fast- and slow-changing variables. In such a system, the Born-Oppenheimer approximation justifies that the slow dynamical variables are independent of time, and can be used as evolution parameters of the system. As a classic example, we consider the hydrogen atom. The nucleus system evolves on a much

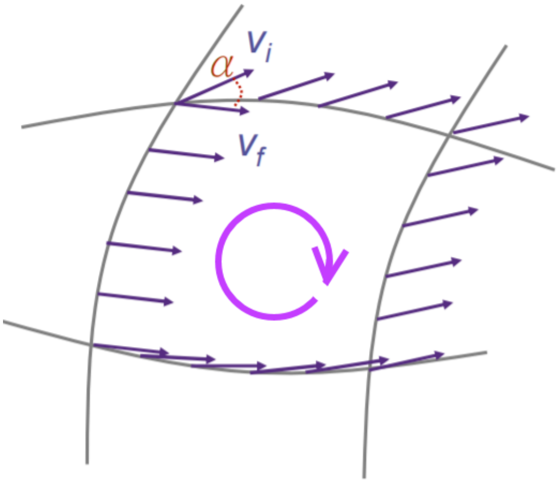

Figure 18: Parallel transport of a vector in a closed loop on a surface measures the surface intrinsic curvature via the anholonomy angle $\alpha$ [23].

longer time scale than the electrons. The slow momentum coordinate is ignored, and we only consider the slow position coordinate [23]. As such, the nucleus position $\boldsymbol{R}$ can be our time-independent parameter, and our quantum state is the following:

$$|\psi_t\rangle = e^{i\gamma_n(\boldsymbol{R})} e^{-i/\hbar \int_0^t dt \epsilon_n(\boldsymbol{R}_t)} |n; \boldsymbol{R}\rangle \tag{5}$$

If we want to determine the evolution phase $\gamma_n$ , we need to insert our state into the time-dependent Schödinger equation. Straightforward calculation yields [23]:

$$\dot{\gamma}_n(t) = i \langle n|\dot{n}\rangle \tag{6}$$

The system evolves adiabatically [41] by one cycle on a closed path $C$ in $\boldsymbol{R}$ -space. This will yield the (path-dependent) phase that has been accumulated:

$$\gamma_n(C) = i \oint_C \langle n|\frac{\partial n}{\partial \boldsymbol{R}}\rangle \cdot d\boldsymbol{R} \tag{7}$$

Berry labeled this integrand as $\boldsymbol{A}(\boldsymbol{R}) \equiv i \langle n|\frac{\partial n}{\partial \boldsymbol{R}}\rangle$, naming this expression the ”Berry connection” [23]. We note that the Berry connection is not gauge-invariant, unlike the Berry phase[32].

We previously mentioned that the Berry phase could be written as an integral over a gauge field. The Berry connection integral doesn't have this form, and so we need to take our expression farther. If we suppose that parameter space is two dimensional, then Stokes' theorem allows us to write the closed line integral as a closed surface integral [78]:

$$\gamma_n(C) = i \int \nabla \wedge \langle n|\frac{\partial n}{\partial \boldsymbol{R}}\rangle \cdot d^2\boldsymbol{R} \equiv \int_S \boldsymbol{\Omega} \cdot d^2\boldsymbol{R} \tag{8}$$

Above, $\boldsymbol{\Omega}(\boldsymbol{R}) = \nabla_{\boldsymbol{R}} \wedge \boldsymbol{A}(\boldsymbol{R})$ is the "Berry curvature" [23]. If we imagine that the Berry connection takes on the role of a vector potential, then the Berry curvature can be interpreted as some form of magnetic field. We can justify this parallel by looking at a change of basis states. Adding an arbitrary phase to the basis state $|n; \boldsymbol{R}\rangle' \equiv e^{ig(\boldsymbol{R})} |n; \boldsymbol{R}\rangle$ leads to changing the Berry connection to $\boldsymbol{A}' \equiv \boldsymbol{A} - \frac{\partial g}{\partial \boldsymbol{R}}$. This cannot change the Berry phase or the Berry curvature, as per their definitions. This is a gauge transformation for a potential, similar to what one finds in electromagnetism [23]. The vector potential is then directly likened to an emergent electromagnetic field [79].

Dirac, in his search for symmetry in the Maxwell equations, found that for magnetic charges (or monopoles) to exist, the vector potential needed to have a singularity [41], or "Dirac string", a physically undetectable object along which the magnetic field is infinite. However, alternate derivations of the Dirac quantization condition rid us of the string [14]. Beyond this resolution in monopole theory, we need to understand why we can say the source of this emergent magnetic field are point magnetic charges, and not, say, some time-varying emergent electric field.

In order to understand why magnetic charge is quantized, it is useful to look at how the Dirac string can be left out of the monopole formulation.

We consider a (large enough [14]) sphere with a magnetic monopole at its center. In order to bypass the string formulation, the sphere is divided into two hemispheres, and a vector potential is separately attributed to both. Their nonvanishing contributions at a given polar angle $\phi$ can be chosen as

$$A^1_\phi = g(1 - \cos(\theta)),\ \theta \,\epsilon\, [0, \frac{\pi}{2}] \text{ (lower hemisphere)} \tag{9}$$

$$A^2_\phi = -g(1 + \cos(\theta)),\ \theta \,\epsilon\, [\frac{\pi}{2}, \pi] \text{ (upper hemisphere).} \tag{10}$$

Both potentials yield the magnetic field of a monopole, $\boldsymbol{B} = g\frac{\hat{r}}{r^2}$, as required. Since both potentials meet at $\frac{\pi}{2}$ , they must describe the same physics ar that point. Their only allowed difference would have to be a gauge transformation:

$$A^1_\phi(\theta = \frac{\pi}{2}) - A^2_\phi(\theta = \frac{\pi}{2}) = 2g \equiv \frac{1}{ie}(\partial_\phi \omega)\omega^{-1} \tag{11}$$

with $\omega(\phi) = e^{i2eg\phi}$. If $\omega$ is multivalued, then the phase of an electron being transported along the $\frac{\pi}{2}$ equator line is not well-defined. We thus require the condition

$$ge = \frac{n}{2},\ n \,\epsilon\, \mathbb{Z} \tag{12}$$

This quantization condition contains no trace of the Dirac string, and leaves us with an important fact: magnetic charge must have integer values (as long as electric charge is also required to). $\omega$ ($\phi$ ) covers the U(1) gauge group g times as $\phi$ cycles from 0 to $2\pi$ . As such, we can see that the magnetic charge of the monopole is a winding number [14], i.e. it counts how many times $\phi$ covers the parameter space.

Since we're interested in physical condensed matter systems, we need monopole-hosting candidates in crystal lattice environments in order to study the intrinsic AHE.

Spin ice systems have hugely degenerate ground states that can host real-space monopole pairs in the form of spins, or magnetic moments. This will not concern the study of $SrRuO_3$ , since despite being postulated as a possible spin glass system at low temperatures [67], this study has since been retracted [56], due to a failure to recognize normal ferromagnetic behavior [17].

The magnetic monopole is not required to be in real space. Lorentz's law states that a magnetic field in real space will affect the trajectory of a charged particle in real space. A magnetic field in k-space would modify the trajectory of a charged particle in k-space. It may seem strange to consider such things, but a k-space magnetic field is exactly what we happen to be looking for in the case of the anomalous velocity due to the Berry curvature.

The Berry phase is associated to the intrinsic contribution of the AHE, wherein an anomalous velocity contributes to the total transport of electrons in the material. Haldane [9] connects this same anomalous velocity with the Berry curvature in the following way:

$$\frac{dx^a}{dt} = \frac{1}{\hbar}\nabla_k^a \epsilon_n(\boldsymbol{k}) + \mathcal{F}_n^{ab}(\boldsymbol{k})\frac{dk_b}{dt} \tag{13}$$

where $\epsilon_n$ is the energy of a Bloch electron in band n, and $\mathcal{F}_n^{ab}$ represents the Berry curvature, the k-space dual of the Lorentz force. To find its source, the divergence operator is applied[9]:

$$\epsilon_{abc}\nabla_k^a \mathcal{F}_n^{ab}(\boldsymbol{k}) = \sum_i q_{ni}\delta^3(\boldsymbol{k} - \boldsymbol{k}_{ni}),\ q_{ni} = \pm\pi \tag{14}$$

with $\epsilon_{abc}$ the Levi-Civita tensor. What this means is that the only source of the Berry curvature is at specific points in k-space: singularities at which a magnetic field in k-space diverges, magnetic monopoles in k-space [9]. From Eq. (13) and Eq. 14, we see that nonzero intrinsic anomalous transport arises from these monopoles. The Berry phase is connected to anomalous intrinsic transport.

Magnetic monopoles in k-space as sources of Berry curvature. The Berry curvature can be written out in several different ways [83] [78] :

$$\boldsymbol{\Omega}_n(\boldsymbol{R}) = \boldsymbol{\nabla}_{\boldsymbol{R}} \wedge \mathcal{A}_n(\boldsymbol{R}) \tag{15}$$

$$\Omega_{\mu\nu}^n(\boldsymbol{R}) = \frac{\partial}{\partial R^\mu}\mathcal{A}_\nu^n(\boldsymbol{R}) - \frac{\partial}{\partial R_\nu}\mathcal{A}_\mu^n(\boldsymbol{R}) \tag{16}$$

$$\Omega_{\mu\nu}^n(\boldsymbol{R}) = i\sum_{n'\neq n}\frac{\langle n|\partial H/\partial R^\mu|n'\rangle\,\langle n'|\partial H/\partial R^\nu|n\rangle - (\nu \leftrightarrow \mu)}{(\epsilon_n - \epsilon_{n'})^2} \tag{17}$$

Equation (15) is in vector notation, whereas equations (16) and (17) are in tensor notation. Eq. (17) shows that the closer the n, n′ energy bands are to being degenerate, the more the Berry curvature could diverge (provided a nominator that tends towards 0 a lot slower than the denominator at the points of degeneracy). As such, we could suppose that areas of avoided degeneracy play the role of k-space magnetic monopole. The Berry curvature in the degenerate scenario requires the use of non-Abelian formalism [83]. We can, however, use semi-classical Abelian analysis by considering symmetries.

We consider the velocity of an electron in a weak electric field. The gauge-invariant crystal momentum $\boldsymbol{k} = \boldsymbol{q} + \frac{e}{\hbar}\boldsymbol{A}(t)$ satisfies $d\boldsymbol{k}/dt = -\frac{e}{\hbar}\boldsymbol{E}$ [83]. In (13) this results in:

$$v_n(\boldsymbol{k}) = \frac{\partial \epsilon_n(\boldsymbol{k})}{\hbar \partial \boldsymbol{k}} - \frac{e}{\hbar}\boldsymbol{E} \wedge \boldsymbol{\Omega}_n(\boldsymbol{k}) \tag{18}$$

The anomalous velocity term is transverse to the applied electric field, indeed reminiscent of a Hall effect. Under time-reversal symmetry (TRS), $v_n$ and $k$ change sign, and under inversion symmetry (IS), $v_n$, $k$ and $\boldsymbol{E}$ all change sign. As such, in order for (18) to remain valid, these symmetries impose constraints on $\boldsymbol{\Omega_n}$:

$$\boldsymbol{\Omega}_n(-\boldsymbol{k}) = -\boldsymbol{\Omega}_n(\boldsymbol{k}) \text{ , for TRS} \tag{19}$$

$$\boldsymbol{\Omega}_n(-\boldsymbol{k}) = \boldsymbol{\Omega}_n(\boldsymbol{k}) \text{ , for IS} \tag{20}$$

It becomes immediately clear from this that for systems preserving both TRS and IS, the Berry curvature vanishes over the whole Brillouin zone (ZBR). However, if either TRS or IS are broken, then this does not have to be the case. In $SrRuO_3$ , ferromagnetism breaks TRS [83]. In $SrRuO_3$ , spin-orbit coupling opens avoided crossing gaps: it's at these points in the ZBR that the Berry curvature is nonzero [41]. We recognize near-degeneracy in this system, the degeneracy lifted on the order of the SOC strength. Fang et al. [41] mapped the Berry curvature for $SrRuO_3$ in a cubic structure:

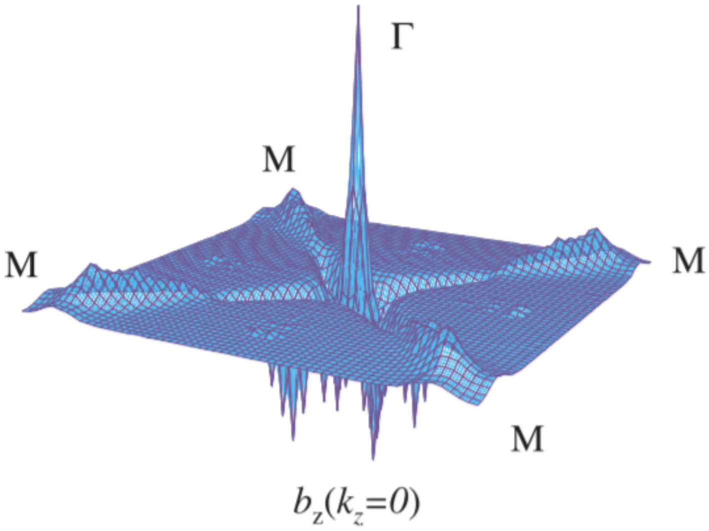

Figure 19: Plot of the Berry curvature for $SrRuO_3$ in the $(k_x, k_y)$ plane with $k_z$ fixed at zero. The sharp peak is due to the monopole source origination from near-degeneracy of the $d_{yz}$ and $d_{zx}$ bands [41].

## 2.6 TOPOLOGY IN $SrRuO_3$

In order to find a k-space monopole, we know that we need to find an avoided crossing. We expect the tight-binding bands of $SrRuO_3$ to be periodic in k-space; this requires every avoided crossing to have a twin, as illustrated schematically in Fig.20. Clearly, if the energy bands are periodic over the first Brillouin zone, then every crossing is accompanied by another. Interpreting this as the creation of a monopole- anti-monopole pair, we can infer that a k-space monopole cannot appear alone in k-periodic systems. 20 might seem like too simple an example, as more complex energy-momentum space trajectories between two periodic points exist. However, no matter the shape of the (single-valued) trajectories or the number of bands included, they will cross an even number of times. The exception is that the bands may only touch at a single point, the superposition of two monopoles, leading them to cancel. An example of this is the link between the Dirac cone and a pair of Weyl cones, where Dirac points have neutral charge and Weyl nodes have opposite chiral charge. If the bands are not spin-orbit coupled, the crossings will not be avoided and cannot change the number of monopole charges. An important consequence of these considerations is that the sum of the total Berry curvature over all bands is zero [32].

Any system that is able to force two spin-orbit-coupled bands to cross can host monopole pairs. This is the case for ferromagnets [49]. Band crossings in ferromag-

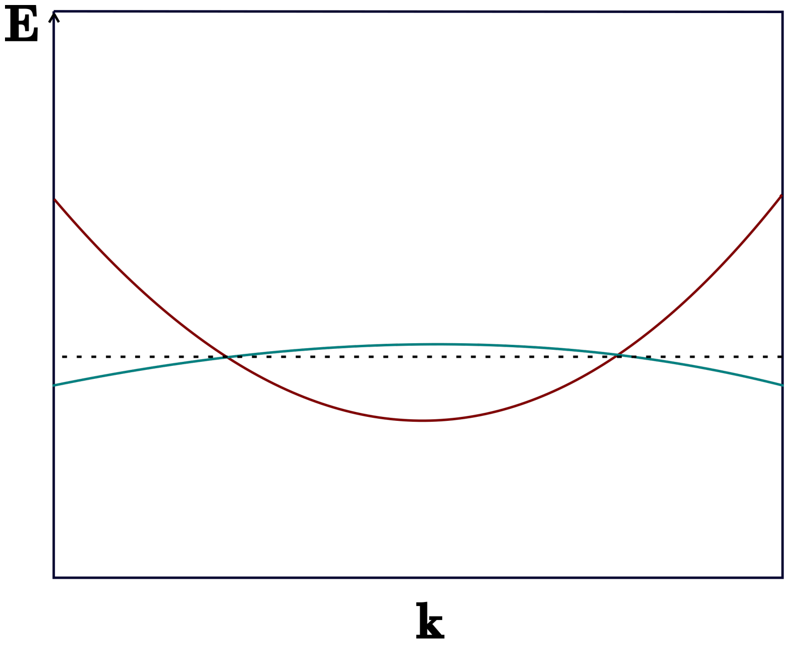

Figure 20: Example of a periodic dispersion in k-space. The dashed line represents the Fermi level.

nets come about when the exchange splitting lead to energy bands of opposite spins crossing.

We can reasonably expect for this to happen in $SrRuO_3$ [49]. Since the phenomenon responsible for the anomalous Hall effect in $SrRuO_3$ is attributable to the occupation of a small number of states close to dispersion crossings, we could expect to see a sharp, quantized signal apparent in experimental data, representative of the quantized nature of the monopoles. The first obstacle to this thinking is to consider whether or not the monopoles are degenerate. If so, adding electrons to the system will simultaneously populate both monopoles. In this case, since the ferromagnetism in $SrRuO_3$ is itinerant, magnetic imaging (e.g. SQUID data) could help reveal the presence of counter-propagating chiral edge currents. Their signature would not be detectable in other transport studies. Barring the degeneracy of monopole pairs, however, there should be a way to see a sharp response close to the monopoles.

We can consider the dispersion of a simple tight-binding model of a $SrRuO_3$ monolayer [45]:

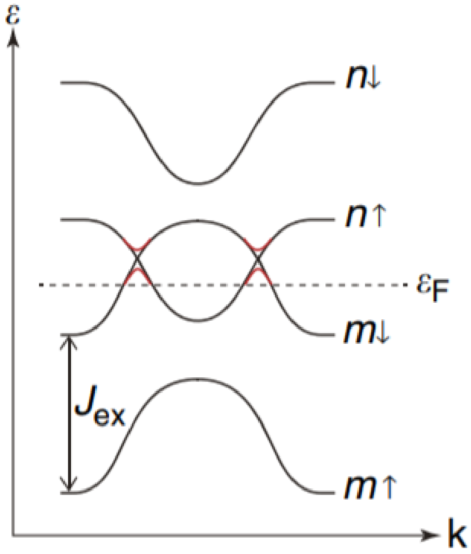

Figure 21: Band inversion due to exchange splitting $J_{ex}$ leading to avoided crossings forming in a ferromagnet [49].

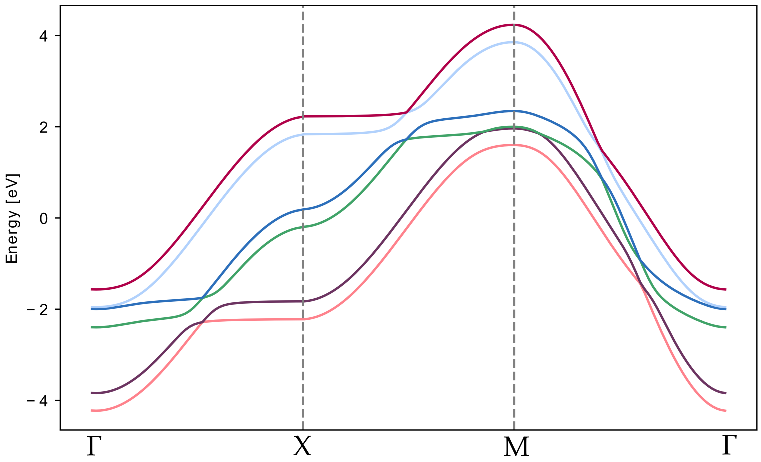

Figure 22: Numerical reproduction of a $SrRuO_3$ monolayer tight-binding model with an exchange splitting of 0.2 eV along tetragonal high-symmetry directions [45]. Details regarding the model can be found in Chapter 5

.

In Fig.22 there is no way to place a Fermi level entirely in a gap; as such, the occupation of states yielding a sharp signal will be accompanied by the occupation of states bearing a finite contribution and states close to other competing monopole points of different charge. This means that we cannot expect the quantum anomalous Hall effect in $SrRuO_3$ , but we can still hope for signal surges when the Fermi level passes by topologically significant points, should they be present close to the Fermi level. As such, this motivates electrostatic experiments, in which the bands could be filled or depleted depending on the applied bias.

## 2.7 ELECTROSTATIC CONTROL OF THE BERRY CURVATURE

### 2.7.1 *Changing the AHE signal via a bias*

Band structure is the representation of a system's eigenvalues in momentum space. As such, the most direct way to probe band structure is through manipulating occupation. One way to achieve this is by applying a bias across the sample. Since we've come to realize that the band structure and the intrinsic Berry curvature are directly linked to each other, such a bias could also directly affect the anomalous transport in the system. Fig.23 illustrates such a principle, using the same $SrRuO_3$ monolayer model from 5.

Changing the Fermi level at a fixed value of magnetization has the potential to change the signal dramatically, as evidenced by Fig.23 a) and b), where tuning the exchange splitting to -1.6 eV and raising the Fermi level by 1 eV leads to a sharp signal reduction, whereas at -0.5 eV exchange splitting, the signal is hardly affected. Fig.23 c)-f) serve to illustrate how the level shift affects the total Berry curvature contributing to anomalous transport.

It is clear from Fig.23 that shifting the Fermi level has the capacity to affect the anomalous signal, with a larger change expected at higher magnitudes of magnetization. For this reason, it is of capital importance to estimate the fermi level shift produced by an applied bias.

### 2.7.2 *Estimating the Fermi level shift*

#### 2.7.2.1 *Thomas-Fermi screening length*

In order to obtain a transport signal, the $SrRuO_3$ film must be metallic. However, an electric field can only penetrate a very short distance into a metal, and so its potential effect is constrained to the very edge of the sample. The penetration distance is related to the Thomas-Fermi length:

$$x_{TF} = \frac{1}{2} \cdot \left( \frac{\pi \cdot \hbar^3}{3n \cdot m_e^3} \right)^{1/6} \tag{21}$$

From Eq.21, it is apparent that the electron density, $n$, strongly determines the penetration depth. $n$ can be determined experimentally with the ordinary Hall coefficient [56]. At low temperatures, it is estimated to be of the order of $10^{21}$ cm$^{-3}$ [10], thus placing

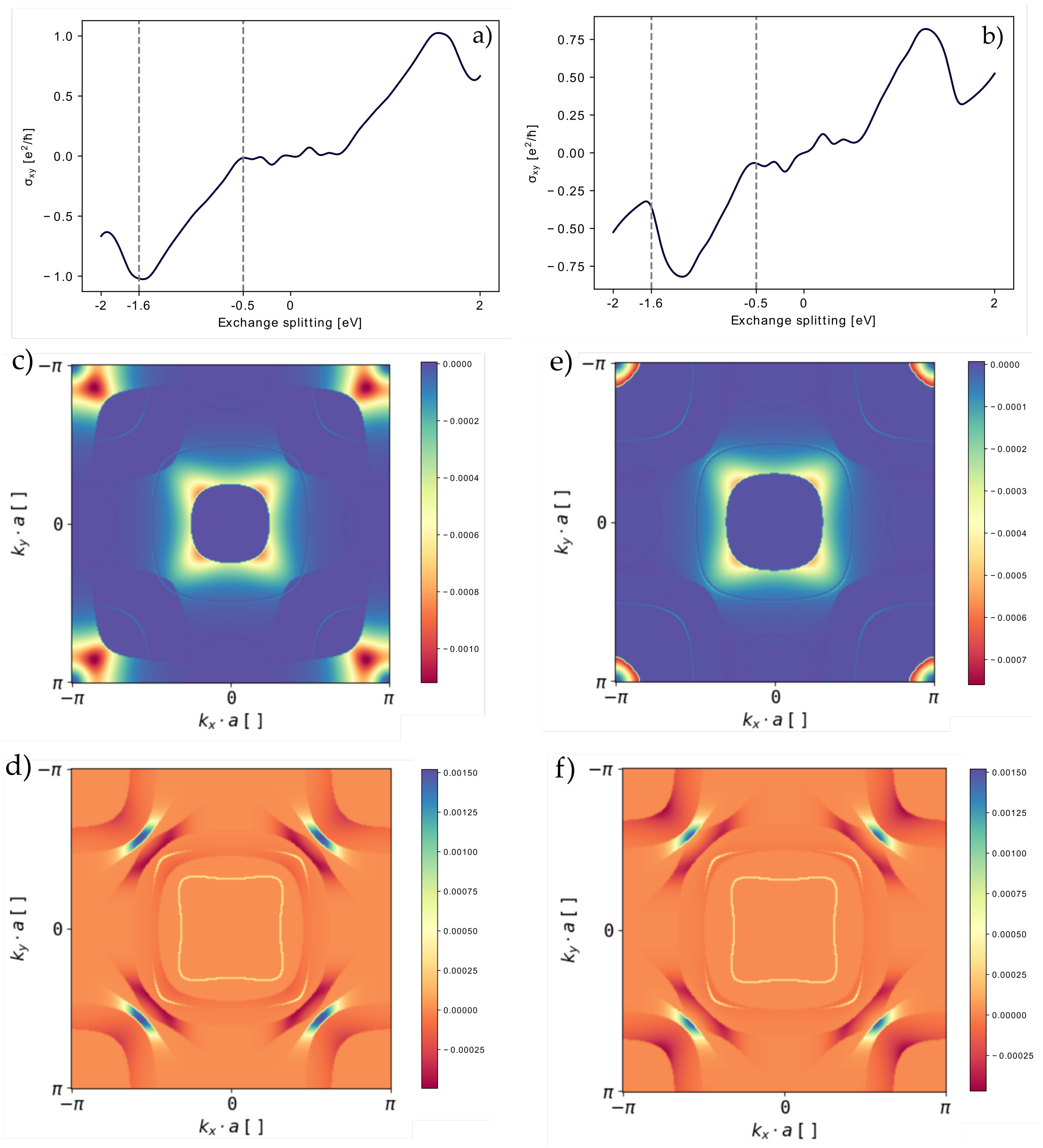

Figure 23: Conductivity and berry curvature calculations of the $SrRuO_3$ model from Ref. [45]. Anomalous conductivity for Fermi levels at a) 1 eV and b) 2 eV. Berry curvature map for a $10 \cdot 10$ division of the first ZBR, at c) 1 eV Fermi level and -1.8 eV exchange splitting, d) 1 eV Fermi level and -0.5 eV exchange splitting, e) 2 eV Fermi level and -1.8 eV exchange splitting, and f) 2 eV Fermi level and -0.5 exchange splitting.

the screening length at 23 Å. Higher estimates of carrier density [72] yield a screening length of 4.25 Å, which falls short of the $SrRuO_3$ lattice constant [56].

#### 2.7.2.2 *Charge accumulation*

Estimating the charge accumulation on the $SrRuO_3$ film can be treated as a simple parallel plate capacitor problem filled with two dielectric layers, the alumina and the $LaAlO_3$. The alumina layer is 25 nm thick, and the $LaAlO_3$ is 10 u.c. thick, or 4 nm [11]. Their dielectric constants are 7 [16] and 24.5 [11] respectively.

A typical area used for the device top gates is $4 \cdot 10^{-9}$ m$^2$, and so the calculation of two capacitors in series yields a capacitance of $1.05 \cdot 10^{-11}$ F. Applying 15 Volts leads to a charge accumulation of $1.58 \cdot 10^{-10}$ C, or about $10^9$ electrons.

#### 2.7.2.3 *Relating charge accumulation to energy shift*

The accumulated charge adds an electrostatic potential energy term, which leads to a spin-independent global energy shift for charges located within the penetration depth. In essence, charges are accumulating (or depleting, depending on the sign of the applied voltage) on $SrRuO_3$ , that need to occupy $SrRuO_3$ bands. At 0 K, the electrons will occupy the next possible states above the Fermi level, raising it as a consequence. The increase in the Fermi level is directly dependent on the DOS.

Looking back to Fig.4, we see that the d-orbitals are all more or less contained with ± 2 eV of the Fermi level. Since these are the orbitals that will affect the anomalous signal the most, it will be mainly worthwhile to only consider maximum energy shifts of ± 2 eV, and likely expect to see much smaller energy shifts, in the meV range. Matching these possible shifts to experimental data should allow us to determine the degree of band bending and information on the DOS at the new Fermi level.

# Part II

# EXPERIMENTAL SETUP

# 3

# EXPERIMENTAL METHODS

## 3.1 OVERVIEW OF EXPERIMENT

## 3.2 SAMPLE PREPARATION

### 3.2.1 *Film deposition*

Thin $SrRuO_3$ films of about 5 u.c. are grown via pulsed laser deposition (PLD) by Thierry van Thiel onto $SrTiO_3$ substrates, then capped with $LaAlO_3$ . $SrTiO_3$ closely matches the lattice constant of the pseudolattice of $SrRuO_3$ and is insulating [56], making it a good match for $SrRuO_3$ . $SrTiO_3$ having a higher dielectric constant than $LaAlO_3$ , the former diverging at 0 K [12] and the latter increasing to about 27 [84]. However $LaAlO_3$ is used for the capping based on considerations from previous experiments (cf. Appendix 7.1).

In order for their structure to be preserved, films must be deposited onto the substrate epitaxially: at the interface, the lattices should lock on to each other and share the same lattice constant. This is acheived by ablating plumes of Strontium and Ruthenium from a stoichiometric target using high-energy laser pulses. These plumes attain the substrate surface, and the $Sr$ and $Ru$ atoms reorganize with $O$ to form $SrRuO_3$ . The details of this process are as follows.

The laser used is a LPX Pro 305F KrF-excimer laser. It lases 248 nm UV light in pulses that are set to deliver $1 J/cm^2$. These pulses are focused onto the selected rotating target. The photon energy is absorbed by the lattice via its electrons. The absorption time scale is far shorter compared to the thermal relaxation, thus resulting in plasma formation on the pulse duration time scale [6]. This plasma is composed of neutral atoms in various excited states and electrons. The plume expands outward and condenses onto the substrate [28].

The oxygen pressure in the chamber is a crucial component, as it is necessary to the growth of any oxide. The oxygen gas interacts with the plume and is incorporated into the film. In doing so, it also reduces the kinetic energy of the plume; in order to obtained the desired film stoichiometry, an appropriate oxygen pressure must be used. Typically 0.1 mbar is used to grow $SrRuO_3$ films.

After the PLD, the sample is annealed at 600°C for one hour at an oxygen pressure of 300 mbar in order to replete oxygen vacancies. The sample is then cooled down by 20°/min.

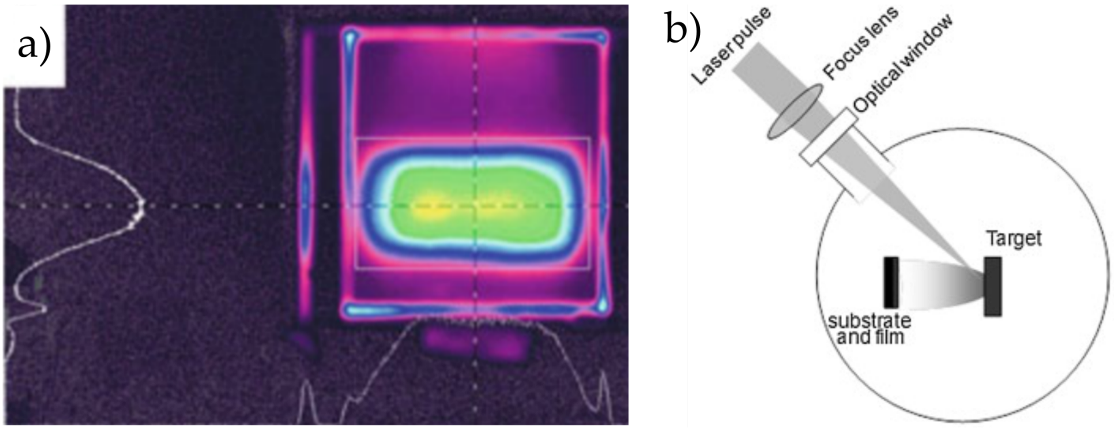

Figure 24: a) Beam profile of a KrF excimer laser at 248 nm [6], b) schematic of the working principle of PLD [28].

PLD thus offers a precise control on film thickness. In order to monitor the growth, a high-pressure reflection high-energy electron diffraction (RHEED) system is used. It provides in-situ information on the development of the film. Electrons, typically within 10-30 keV, are accelerated from an electron gun to the surface of the sample at an incident angle of about 3°or less with respect to the surface. This angle is small enough that the electrons are diffracted by the first few crystal planes of the film. The diffracted electrons are collected by a sensor, and the crystalline structure of the film can be deduced from their resulting diffraction pattern.

In each plume, an insufficient amount of matter condenses for an entire, uniform crystal plane to be formed. Instead, the matter either forms islands that then coagulate into a single layer (layer-by-layer growth), or if the adatoms have sufficiently high energy, they migrate to step edges of the lower surface so that several layers are being formed at the same time (step-flow growth) [6]. The electron diffraction pattern is responsive to the crystal structure: disorder leads to broader, streaky diffraction spots, whereas a perfect crystal plane will result in narrow signal peaks. In layer-by-layer growth, as a layer is being formed, the diffracted electron signal will be low, increasing in strenghth as the crystal plane becomes more structurally organized, until reaching a peak upon completion of the layer. In this manner, control of the film thickness can be done on the unit cell scale [6]. Fig.25 shows the evolution of the RHEED signal during deposition in layer-by-layer growth. The number of oscillations indicates the number of layers grown. In Fig.25a) shows five dips, indicating the deposition of 5 u.c. of $SrRuO_3$ . In Fig.25b) we count the deposition of 10 u.c. Growth is stopped at the fifth minimum for $SrRuO_3$ and the tenth minimum for $LaAlO_3$ . We note an increase in signal intensity after the end of the deposition, which is a sign that the adatoms are reorganizing on the surface of the film. This in turn is a demonstration of their high mobility during deposition.

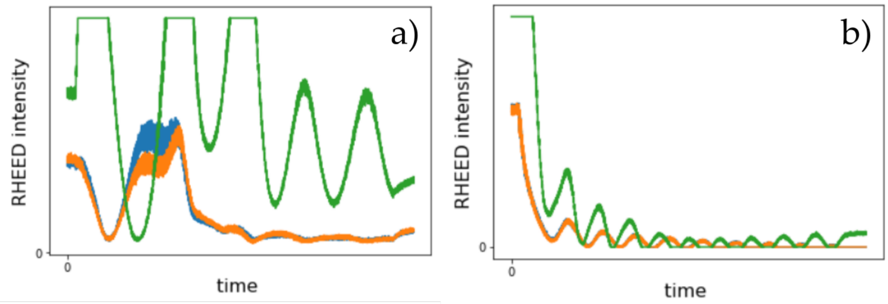

Figure 25: Intensity of RHEED signal with time for a STO/SRO/LAO sample. a) deposition of $SrRuO_3$ , b) deposition of $LaAlO_3$ . The three curves correspond to the intensity read at the positions indicated in Appendix 7.2.

### 3.2.2 *Samples*

The samples and their growth characteristics are listed in Table1:

Table 1: Samples as grown

| **Label** | **Substrate** | **Layer 1** | **Layer 2** |
|---|---|---|---|
| FM15 | $SrTiO_3$ (001) | $Sr_3Al_2O_6$ 125 u.c. | $SrRuO_3$ 25 u.c. |
| SRO12 | $SrTiO_3$ (001) | $SrRuO_3$ 5 u.c. | $SrTiO_3$ 10 u.c. |
| SRO13 | $SrTiO_3$ (001) | $SrRuO_3$ 5 u.c. | $LaAlO_3$ 10 u.c. |
| SRO26 | $SrTiO_3$ (001) | $SrRuO_3$ 5 u.c. | $LaAlO_3$ 10 u.c. |
| SRO27 | $SrTiO_3$ (001) | $SrRuO_3$ 4 u.c. | $LaAlO_3$ 10 u.c. |
| SRO32 | $SrTiO_3$ (001) | $SrRuO_3$ 5 u.c. | $LaAlO_3$ 10 u.c. |

Sample FM15 was grown in 2017 prior to this project. The final patterned sample consisted of a free-standing $SrRuO_3$ flake. The methodology followed to obtain the oxide flakes is described in Ref.[60].

Notes regarding the deposition involve the presence of 3D structures on SRO13, as pictured in Fig.26. They could originate from droplets of liquid target reaching the surface of the film during deposition, but there was no evidence for 3D growth at the time of deposition. This should be taken into account whilst considering the results obtained from SRO13.

A second note regarding growth is a positive one: the RHEED signal for SRO32 is indicative of an atomically flat surface, indicating 2D growth with minimal roughness, as shown in Fig.27. Additional morphological characterization of the growth can be found in Appendix 7.3.

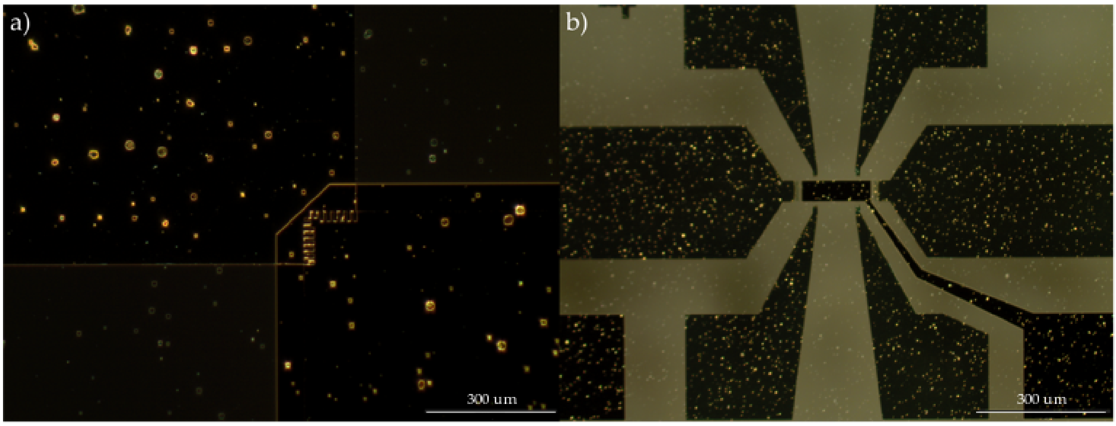

Figure 26: Dark-field images of SR013 devices, a) a Van der Pauw device and b) a Hall bar. 3D drop-like protrusions cover the entire surface.

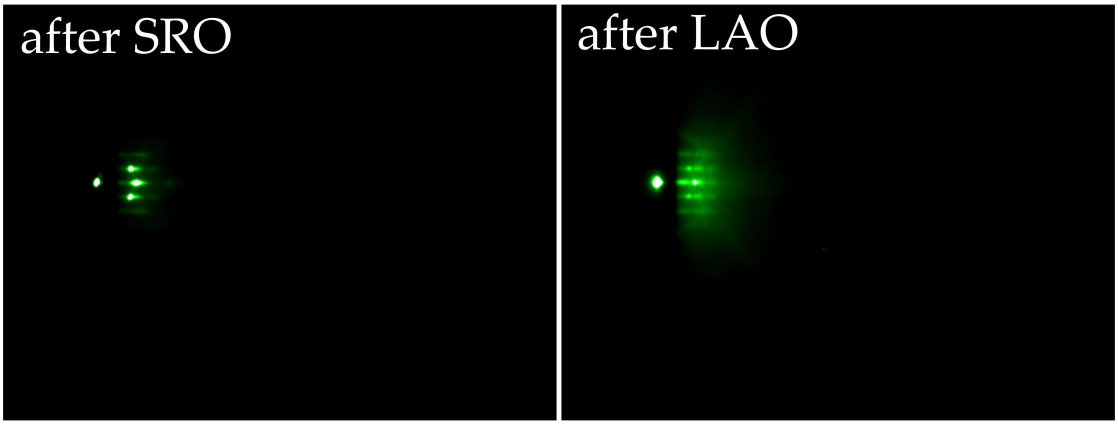

Figure 27: SRO32. RHEED signal before and after $LaAlO_3$ deposition. The broadening of the signal is visible after $LaAlO_3$ , but it remains exemplary of good 2D growth.

### 3.2.3 *Patterning*

A variety of devices can be patterned onto a single sample, ensuring that at least one will normally survive mishaps in the patterning process and be measurable. Typical configurations useful for anomalous Hall experiments are Hall bars and Van der Pauw devices, and 7 to 10 of varying geometries can fit together. Larger devices are likely to be more inhomogeneous, but output a larger signal than the smaller ones. The data in this thesis was collected using large (SRO13, SRO32) to medium-sized (FM15b) Hall bars.

The process flow for the production of the experiment-ready samples can be found in Fig.28.

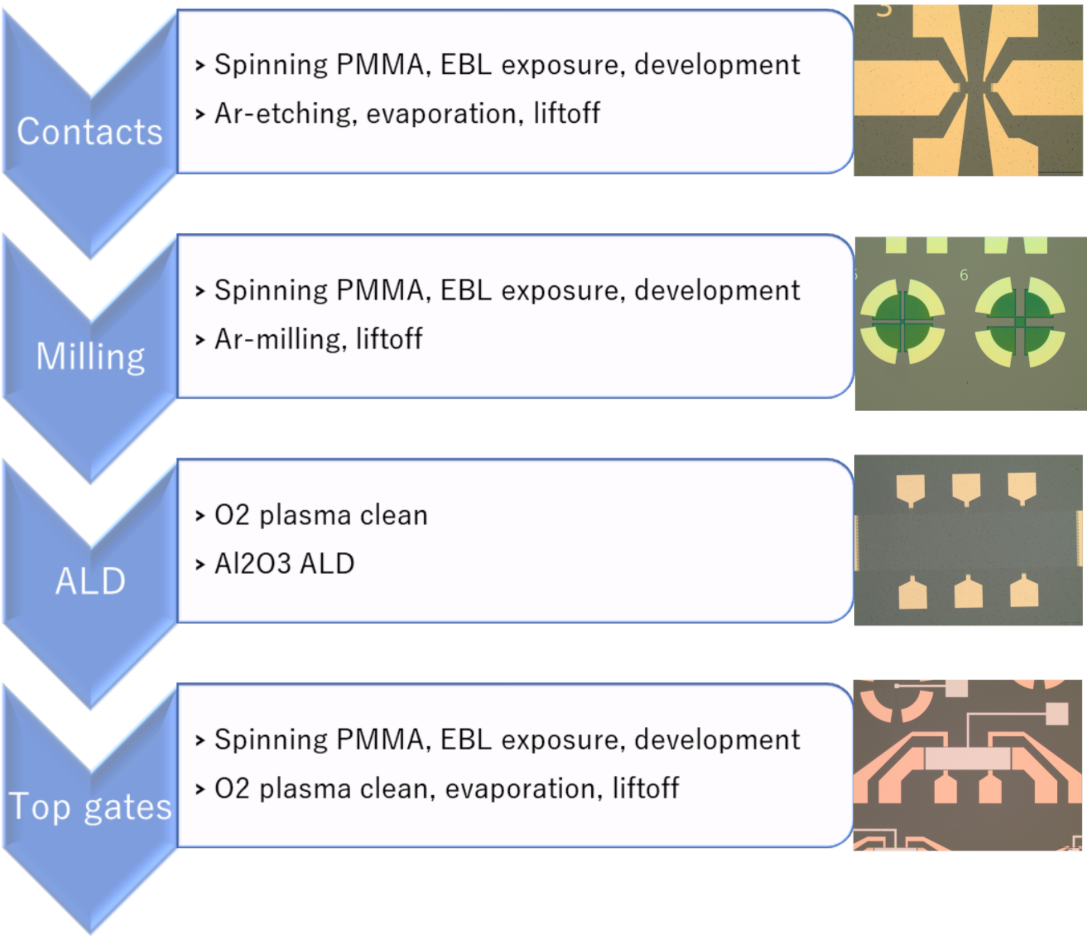

Figure 28: The steps required to pattern the samples examined in this thesis.

Once the film has been epitaxially deposited via PLD, the first step is to define contacts. The devices on the sample are on a scale of tens to hundreds of microns, and thus require a high level of spatial precision for delimiting their boundaries. For this, we use the EBPG 5000 for electron-beam lithography (EBL) in order to write a pattern into polymethyl mecrylate (PMMA) and ”Elektra” resist. The Elektra layer is added on top of the PMMA as a thin conducting layer that will prevent electrons accumulating in the sample during the EBL.

The exposed resist is removed by development in deionized water to remove the Elektra, a 1:3 mixture of methyl isobutyl ketone (MIBK) and isopropyl alcohol (IPA) to remove the PMMA, and lastly in IPA to stop the chemical reaction. It is important to quickly dry the sample after the IPA, as it can tend to leave puddle-like stains on the sample surface.

Once developed, the sample is submitted to argon etching in the load-lock QT-AJA. Etching through the $LaAlO_3$ and $SrRuO_3$ on non-device areas will allow side-contacting of the films. Non-contact areas are protected from the etching by the PMMA.

The etch time was extrapolated from a calibration etch test, as there are no sensors indicating the etch depth. It is vital to not etch too little, as if the $SrRuO_3$ is not completely removed from contact areas, the contacts risk being shorted through the metallic film. It is also important to not etch too much, as $SrTiO_3$ has found to become conducting at its surface following Ar etching [68]. Additionally, Ar etching tends to heat the sample. Consequences of this range from difficult resist removal as it has been over-baked to altering the sample stoichiometry. Suggested amendments include a water-cooling system to prevent the sample from over-heating, which has been implemented previously in similar machines.

Once the etching is complete, the sample is loaded into the main chamber and metal is evaporated onto the etched area to form the contacts. Metals used for the contacts ranged from germanium and gold to palladium. Lift-off in warm acetone removes the coat of metal from the rest of the sample by dissolving the remaining PMMA, as can be seen in Fig.29. Lift-off can be assisted by sonication, or the use of the more aggressive n-methyl-2-pyrrolidone (NMP), which additionally has a higher boiling point than acetone. If there is no access point to the resist due to too thick a layer of metal, the sample can be lost as the metal layer cannot be removed.

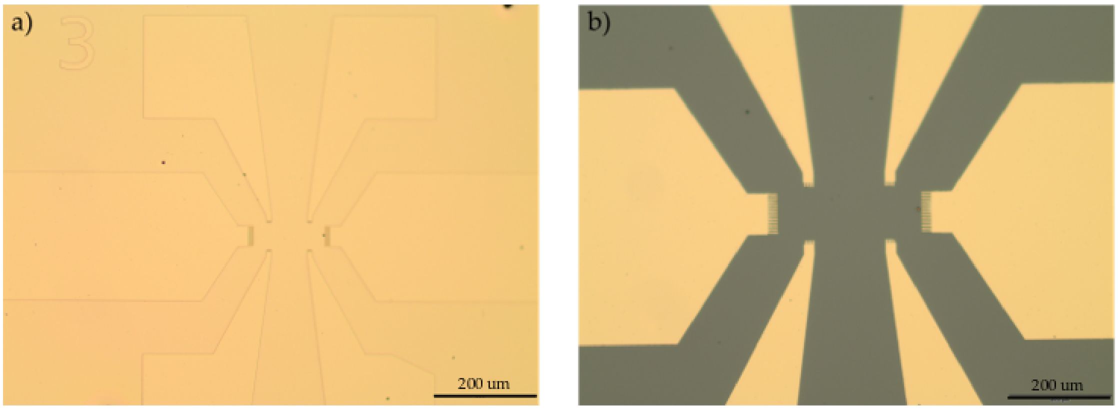

Figure 29: Sample SR012. a) Post metal deposition, b) post lift-off

The next step involves defining the device shapes. EBL and development is used to remove resist from the remaining area of the sample not intended for devices. Ar etching is once again used, and the resist serves as an etch mask that is dissolved once the etching has been completed.

Looking back to Fig.26 a), we see that post-etch, the size of the 3D droplets on SR013 has been reduced noticeably. The etch, however was not deep enough to remove them completely. Further, the etch has no ability to remove the droplets on the device itself, since that area is protected. This may lead to some non-uniform behavior.

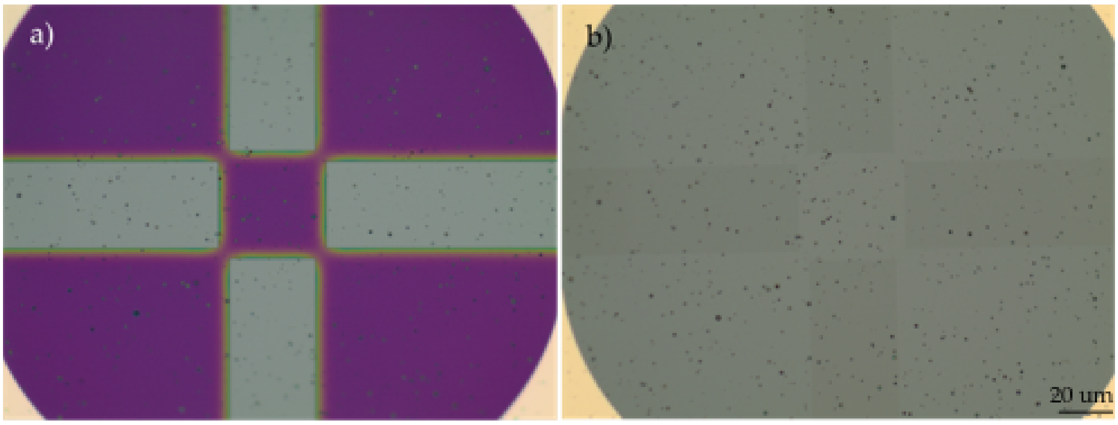

Figure 30: Sample SR013. a) Pre-etch, with resist covering the device area. b) Post-etch and development. The device outline is faintly visible.

Next, the dielectric layer is deposited on the sample via atomic layer deposition (ALD). Although alumina is deposited at 300°C and above [35], 105°C was chosen in order to not disturb the stoichiometry. The dielectric layer is vital to the experiment. A small thickness yields higher capacitance, but it needs to be thick enough to help prevent the dielectric breakdown of $LaAlO_3$ [76], which could damage the device. A larger thickness also helps the electric field lines arrive in a more parallel fashion to the surface of the sample.

The final step is the deposition of top gates. This process is almost identical to making the contacts, with the difference being an oxygen cleaning as opposed to an Ar etch prior to evaporation. Finished devices are pictured in Fig.31.

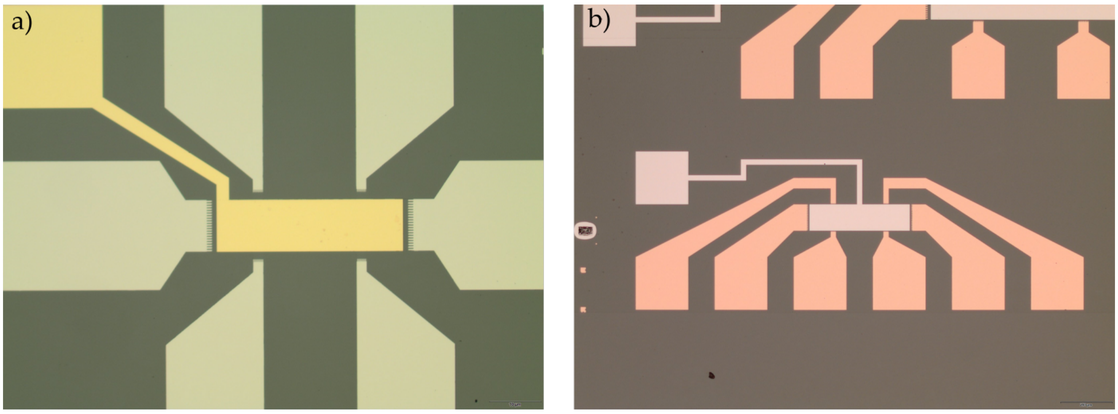

Figure 31: Devices with top gates from a) sample SRO26 and b) sample SRO32.

### 3.2.4 *Mounting the sample for experiment*

Once the sample has been patterned, it needs to be contacted. Silver paste is applied to the bottom of the substrate and stuck onto a PCB, ensuring an electrical connection from the sample to the PCB's back gate. Wire bonds are used to contact the PCB to the sample contact pads. The wires are made of a eutectic alloy of Aluminum and Silicon, making them easy to melt into place.

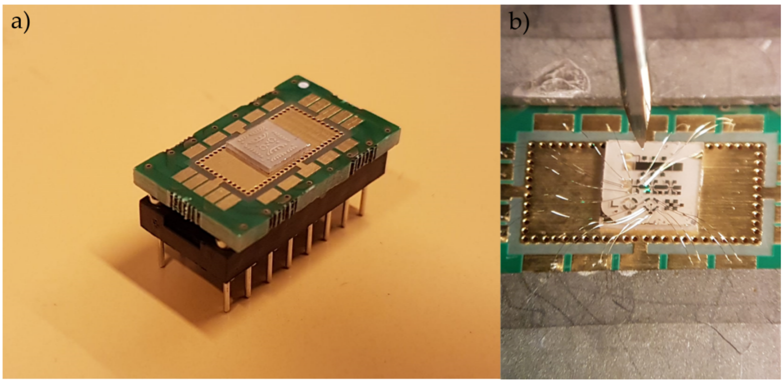

Figure 32: a) SRO32 mounted on a PCB. b) SRO26 at the wire-bonder (needle apparent in center)

## 3.3 SAMPLE MEASUREMENT

Since *SrRuO*3 samples can only host ferromagnetism below room temperature, we need to cool the sample in order to measure its AHE response. For this purpose, the sample is attached to an electrically-contacted arm and inserted into a flow cryostat.

### 3.3.1 *The fridge system*

The flow cryostat is composed of several chambers, as seen in Fig.33: an outer chamber contains liquid nitrogen, which acts as a heat isolator for the inner compartments. A chamber with liquid helium wraps around the core, in which the sample is inserted. He gas enters the sample space through a variable opening, and is pumped away. As it evaporates, the He gas cools the sample temperature below 4.2 K, down to 1.5 K. Before starting anomalous Hall measurements at any temperature, the sample must first be cooled down to the minimum temperature. This ensures the restoration of the magnetic state and makes a (hopefully) identical starting point so that subsequent measurements remain comparable. In order to heat up the sample, rather than closing the He flow, a heater in the sample arm heats the back of the PCB. Teflon tape is applied to the back of the PCB before connecting it to the arm in order to avoid too

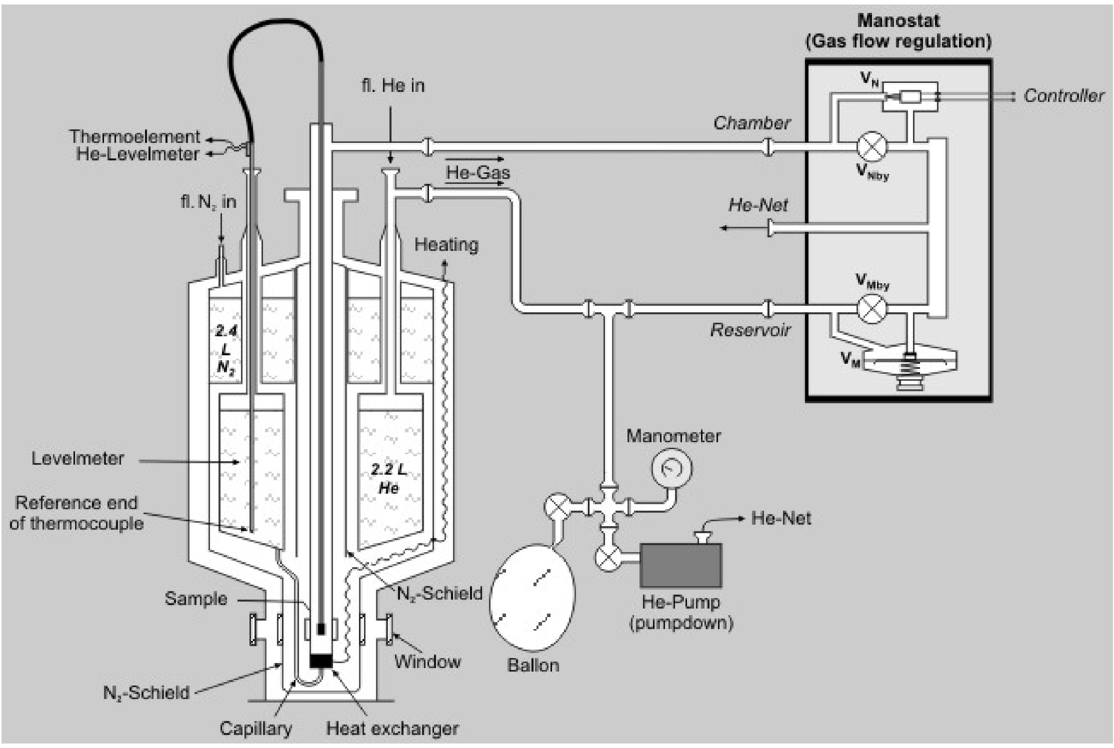

Figure 33: Schematic of a flow cryostat [1]

strong a thermal contact to the heater. This allows a ± 0.1 K control of the temperature, which is vital to the stability of the measurements.

In the helium bath is a superconducting magnet coil that surrounds the sample space chamber. The sample is introduced such that the magnetic field in the coil is applied to the sample perpendicularly.

### 3.3.2 *Control parameters*

Transport measurements can be operated on the sample via sweeping of several parameters. Magnetization can be controlled with an applied magnetic field perpendicular to the sample, and field sweeps are used to obtain the AHE signal. Temperature is also an important parameter; it controls the magnitude of the magnetization, as well as the ferromagnetic phase transition. Thermal control of state occupation is also a crucial element, not only in the unfreezing of trapped states but also in previous studies, the AHE has shown double-loop characteristics apparent in only a certain temperature frame [45]. Cooldown curves are used to study the metallic or insulating nature of the sample. A combination of magnetic field and temperature control yields field cooldowns, in which cooldown curves are compared for two equal and opposite values of magnetic field.

Further control can be exerted via the back and top gates. The purpose of both is to bias the sample in order to deplete or fill a differing range of states. The back gate is separated from the $SrRuO_3$ devices by the substrate, whereas the top gate lies on the sample proper, with only $LaAlO_3$ and the alumina dielectric layers. As such, while the back gate can safely supply hundreds of volts, care needs to be taken to not apply a voltage whose resulting leakage current exceeds 0.01 $\mu$ A or more via the top gate (depending on the value of the leakage current) in order to prevent dielectric breakdown. Defects are also starting points for electric failure [15], and in big devices the probability of having such defects is higher.

# 4

# NUMERICAL METHODS

## 4.1 NUMERICAL BERRY CURVATURE

### 4.1.1 *Creating a tight-binding system*

Experimental results can be compared to previously obtained results from articles and reports. Another type of comparison can be done using numerical simulation. Depending on the level of refinement, a model can provide either a general framework, a qualitative analysis or specific trends data can be expected to obey.

Since we know that the intrinsic AHE finds its origin in band-structure interactions, we need to model the dispersion relation of $SrRuO_3$ . This could involve the creation of lattice points defined by a strong periodic potential [78] related by hopping values, generating trajectories in energy-momentum space that match the low-energy behavior of $SrRuO_3$ . Such an approach is known as a tight-binding model.

A tight-binding approach is debatable in its relevance to $SrRuO_3$ , as it is a one-electron model [4], and $SrRuO_3$ has moderate electron-electron interaction [72]. The transport properties of $SrRuO_3$ changing from metallic to insulating with decreasing film thickness is not simply ascribable to defect scattering, but is closely related to film stoichiometry and the degree of electron-electron correlation [80]. As such, despite the fact that it should have the largest response to the top gate due to a longer screening depth, capturing the qualitative physical response of the semiconducting $SrRuO_3$ sample could prove to be beyond the capabilities of a correlation-free model.

Using code from the Python library Kwant [46], a tight-binding model can be generated and passed to a solver in order to calculate physical properties of the system. The creation of a tight-binding system with Kwant is as follows. First, a mathematical graph (a set of nodes [2]) is created by calling an instance of kwant.lattice. The nodes are Bravais lattice sites that can be arranged with built-in libraries of kwant.lattice (eg. ’honeycomb’, ’square’, ’kagome’) or any arbitrary shape using kwant.lattice.general. The tight-binding model is created through defining onsite energies on the nodes and connecting them by defining hoppings. Leads (tight-binding systems with translational symmetry in at least one direction) are attached to the system so that transport properties between leads can be probed by the Kwant solvers. Before it can be passed to solvers, the system is finalized, which sets the tight-binding graph but leaves the matrix elements open to change [46].

The numerical computation of the AHE requires knowing the periodic band structure of the lattice. In order to obtain periodic band structure information, we need a periodic lattice. Since an edge presents a break in periodicity, that means the lattice should be infinite in the directions we want band structure information. A monolayer should be infinite in-plane (2D), and a thick structure should be infinite in 3D. The infinite system is then wrapped around, and the result is a k-space periodic system, with periodicity $2\pi/a$, $a$ being the lattice constant (for a cubic system) [4].

### 4.1.2 *Considerations on precision*

The key to analyzing anomalous transport are the eigenvalues and eigenvectors. The solver hamiltonian_submatrix allows us to obtain the tight-binding Hamiltonian matrix, from which the eigenvalue and eigenvector sets can be extracted with the use of e.g. scipy.linalg functions.

Having obtained the eigenvalue and eigenvector set, we now need to implement Eq.7. Eq.8 implies that the Berry curvature is related to the Berry phase per unit area in parameter space. We note that Eq.7 relies on the existence of a function of a continuous set of eigenvectors and eigenvector derivatives, over which a contour integral is performed. Ideally, nothing would stop us from generating a continuous energy and eigenvector surface from our tight-binding Hamiltonian. We are however limited by computational restraints: a computer cannot be expected to yield an infinite set of values; such a set could not be stored in its memory. In any case, we only need a 'fine enough' [43] mesh, such that changes in the local Berry curvature are adequately visible. Finding a fine enough mesh can be done by comparing anomalous conductivity calculations to each other for increasing values of k-space precision, as a cut-off after which change is negligible can generally be found.

Globally, the integration of the Berry curvature over the whole ZBR should yield a quantized CN for an isolated energy surface, independent of the mesh value. However, the value of the CN may change with increasing precision [43]. By looking at the Fermi surface behavior of the model, we can estimate how fine our inquiry grid needs to be in order to capture energy surface changes on the order of linear behavior between adjacent grid points. Without this condition, nontrivial contributions may be washed out locally. The necessary grid spacing typically varies over the Fermi surface. An example of the importance of sufficient precision can be seen in Fig.34. In this case, a ZBR partition into a set of $50 * 50$ squares is sufficient to capture a majority of the information; higher resolution yields no visible change to the energy surface.

### 4.1.3 *Calculating the Berry curvature*

We may have resolved the problem of a discrete mesh, but we still need to express a continuous integral on a mesh. For a small enough k-space lattice spacing, we can consider adjacent points as directional derivatives relative to each other, i.e. $\partial \boldsymbol{k}/\partial \boldsymbol{k_x}$ is expressed as $\boldsymbol{k} + b\hat{\boldsymbol{k}_x}$, $b$ the reciprocal space lattice spacing [82]. Calculating local

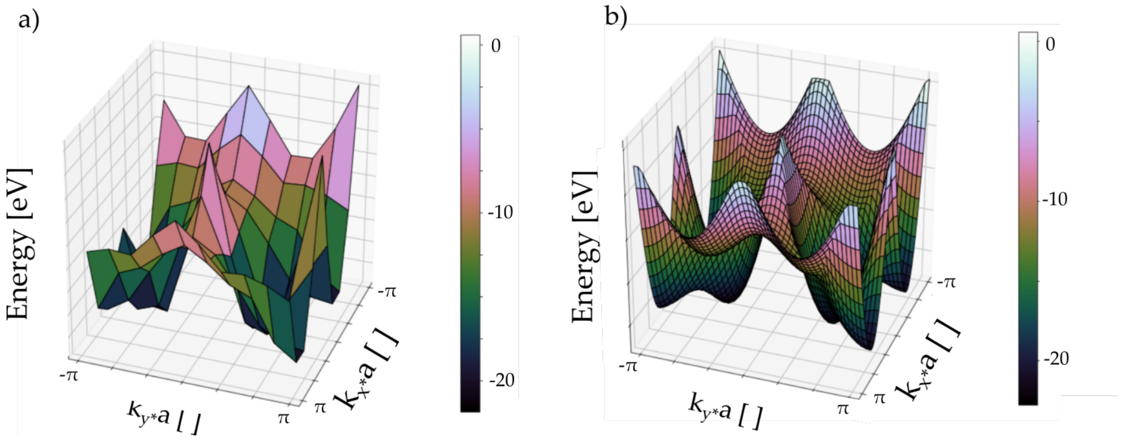

Figure 34: The lowest energy band surface of the $SrRuO_3$ -$SrIrO_3$ bilayer model that will be detailed in section 5.1, at $-\mu \cdot B = 0.25$ eV and a) $10 * 10$ b) $50 * 50$ ZBR partition.

Berry curvature is done by finding the anholonomy angle of a chain dot product of neighboring eigenvectors of the form [36]

$$\langle u_k | u_{k+b\hat{k_x}} \rangle \langle u_{k+b\hat{k_x}} | u_{k+b\hat{k_x}+b\hat{k_y}} \rangle \langle u_{k+b\hat{k_x}+b\hat{k_y}} | u_{k+b\hat{k_y}} \rangle \langle u_{k+b\hat{k_y}} | u_k \rangle \tag{22}$$

The neighboring eigenvectors are thus located on the corners of the smallest possible closed square loop in k-space. Eq.22 yields a complex number. We obtain the complex phase by taking its principal argument [82]; this phase is none other than the Berry phase. The Berry phase over a unit contour is the integration of the Berry curvature over a unit k-space area [32], Eq.8 confirming this is dimensionally correct. Overall, this yields the following form for the sum of the Berry curvature from states below the Fermi level of band n:

$$K_n = \frac{1}{2\pi} \sum_{\boldsymbol{k},E(\boldsymbol{k})<E_F} \Im \ln \left( \langle u_{n,k} | u_{n,k+b\hat{k_x}} \rangle \langle u_{n,k+b\hat{k_x}} | u_{n,k+b\hat{k_x}+b\hat{k_y}} \rangle \langle u_{n,k+b\hat{k_x}+b\hat{k_y}} | u_{n,k+b\hat{k_y}} \rangle \langle u_{n,k+b\hat{k_y}} | u_{n,k} \rangle \right) \tag{23}$$

The anomalous conductivity (in units of the conductance quantum $e^2/h$) is then obtained by summing over all bands [82].

The code used for obtaining the Berry curvature of our models can be found in Appendix 7.

### 4.1.4 *Calculating the anomalous conductivity*

Obtaining the Berry curvature over all of k-space is simply the addition of the Berry curvature results over every square in the ZBR. More interestingly for us will be the selection of contributions attributed to energies in a small window around the Fermi level, since these will be the occupied states that contribute to the anomalous transport signal. This is the reason why a fine mesh is particularly important, so as to define the Fermi surface as precisely as possible. We know that at low temperatures and magnetizations, the domain of applicability of a tight-binding model, the Fermi level doesn't reside in a gap in $SrRuO_3$ . It's possible that contributions neighboring the Fermi level, if not carefully excluded or included, would significantly affect the signal. Fig.35 illustrates this notion.

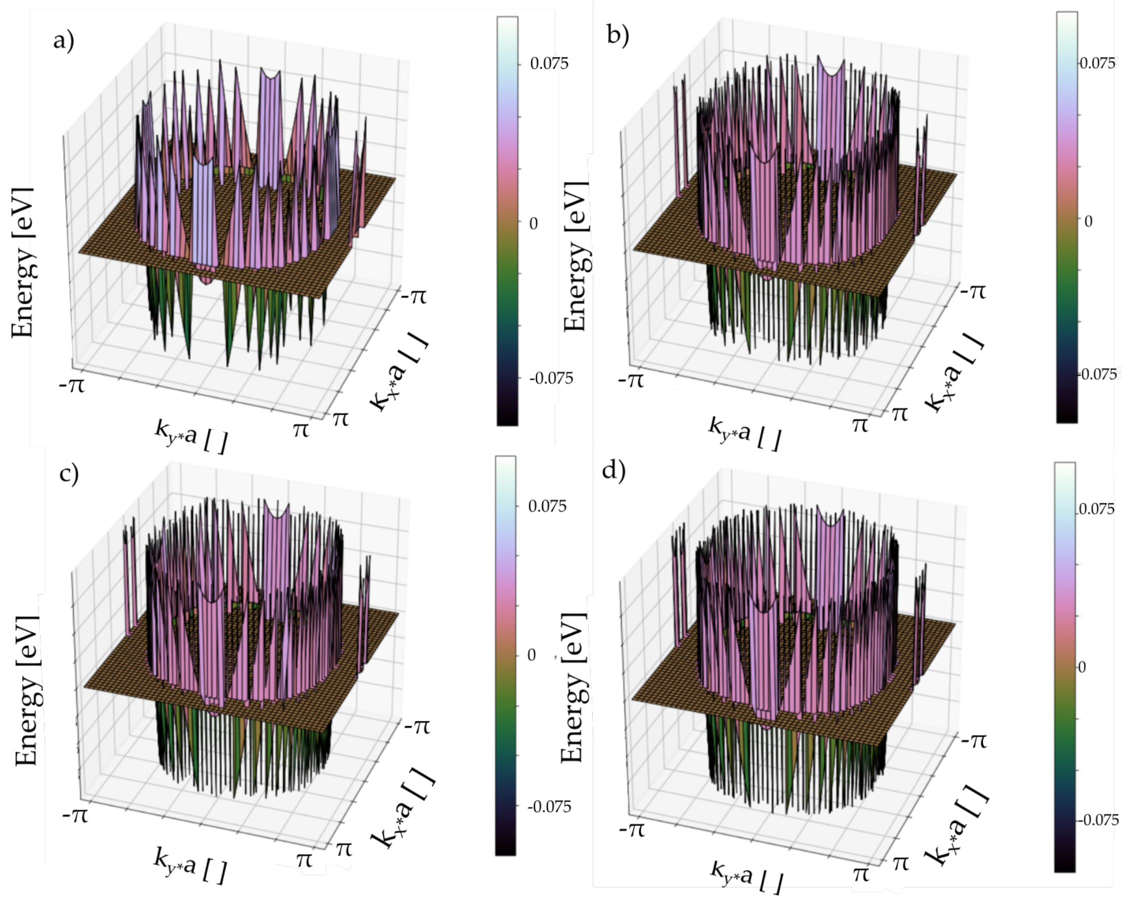

Figure 35: Sixth-lowest energy surface with states within 0.1 eV of the Fermi left intact and all others set to 0, for a) $50 * 50$ b) $200 * 200$ c) $300 * 300$ d) $500 * 500$ squares in the ZBR. We see that although the lack of significant difference between b) and c) might suggest sufficient precision; however, d) still indicates the inclusion of states that might have been excluded. Model used is the same as Fig.23.

Since the calculation of the Berry curvature is calculated with loops made of four states, it seems unjustified to include squares that have three of their four corners above the Fermi level, since those states in principle would not contribute to the signal. As such, it is safer to include squares whose four eigenvalues sum to an energy equal to or smaller than the Fermi level. This will exclude certain states, but it will be a more accurate state selection. This can lead to a smoothing-out of point-like inclusions apparent particularly in Fig.35 b), c) and d). Further improvement of the code could include plaquette weighting factors (0 for plaquettes above the Fermi level, 1 below, and a number between 0 and 1 for squares cut by the Fermi level) as implemented in Ref.[39]. This method would also give a direct indication in the error of the numerical Berry curvature calculation [39].

# Part III

# RESULTS AND DISCUSSION

# 5

# NUMERICAL RESULTS

This chapter will exposit the tight-binding models that will be studied. For this, band structure analysis, local Berry curvature and anomalous conductivity will be calculated as a function of magnetic field splitting and relative Fermi level shift. The goal is to find a behavioral model for the low-energy anomalous Hall signal of the $SrRuO_3$ -$LaAlO_3$ films.

## 5.1 THE MODELS

The models we explore are based on tight-binding models elaborated in the supplementary information of Groenendijk et al. [45]. They include a monolayer of $SrRuO_3$ , a $SrRuO_3$ -$SrIrO_3$ bilayer, and a $SrRuO_3$ -$SrTiO_3$ bilayer. Their tight-binding parameters were obtained via DFT LSDA+U calculations as described in Ref.[45].

### 5.1.1 *Form of the models*

All three models are based on the $Ru$, $Ir$ and $Ti$ $t_{2g}$ orbitals $d_{xy}$, $d_{xz}$ and $d_{yz}$. The $SrRuO_3$ monolayer tight-binding Hamiltonian basis is composed of the $Ru$ $t_{2g}$ orbitals in both z-spin projections. The effective bilayer models are composed of diatomic unit cells, mimicking the interface of $SrRuO_3$ with either $SrIrO_3$ or $SrTiO_3$ . The Hamiltonian orbital basis is thus of length 12.

Ref.[45] adds the effect of a magnetic field through the Stoner model, $E_{\uparrow,\downarrow} = \epsilon(k) \pm I \cdot \frac{N_\uparrow - N_\downarrow}{N}$, with $\epsilon(k)$ the spinless dispersion and $I$ the Stoner parameter [77]. This term enters the Hamiltonian as an additive contribution to the onsite energy, and is spanned from 0 to 2 $m_B/Ru$ [45].

Fig.36 compares the band structure of the bilayer models from the paper to the numerical results obtained with Kwant:

Some clear differences are apparent. The Kwant models included SOC values sourced from Ref [45] for $SrIrO_3$ and from external sources for $SrRuO_3$ [56] and $SrTiO_3$ [52]. No explicit mention is made of the SOC values used to generate the plots referred in Fig.36 a) and b), so the comparison on that front is limited. However, the SOC value for $SrTiO_3$ has little importance due to the bands being far above the Fermi level, and is generally considered very weak (0.02 eV) [85] [52].

Another point of difference is the location of the Fermi level. Ref. [45] states that the Fermi level is set to zero, with no inclusion of this fact apparent in their tight-binding onsite parameters. The energy shift between the $SrIrO_3$ -$SrRuO_3$ models is

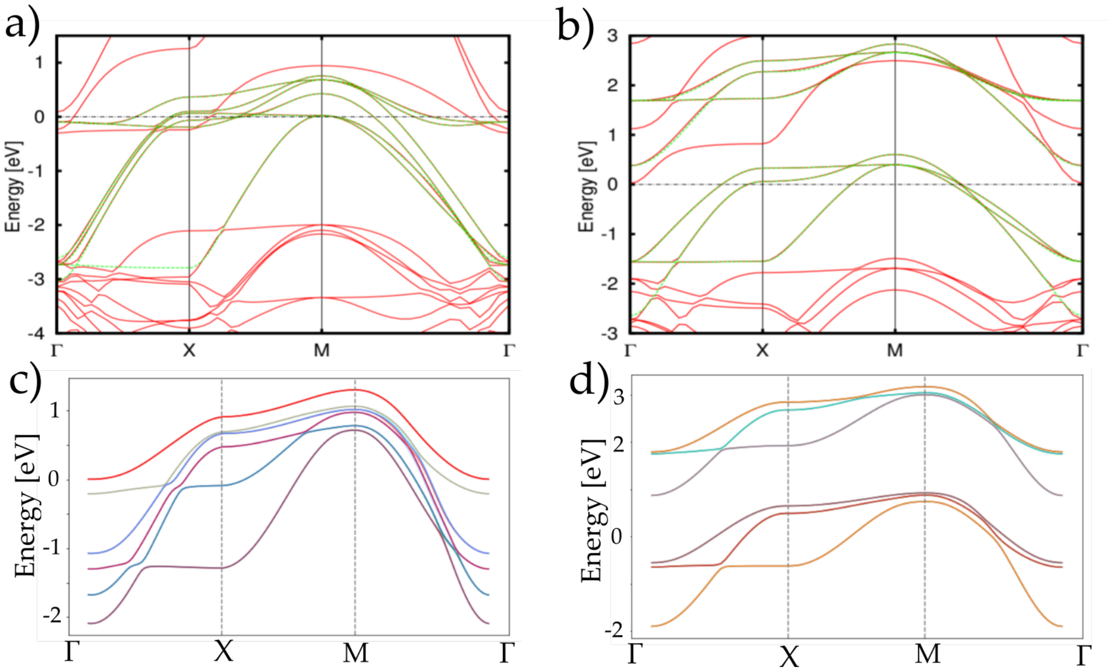

Figure 36: Numerical simulations of tight-binding bands for the bilayer models. From the paper, a) $SrIrO_3$ -$SrRuO_3$ and b) $SrTiO_3$ -$SrRuO_3$ in green [45], and calculated with Kwant c) $SrIrO_3$ -$SrRuO_3$ and d) $SrTiO_3$ -$SrRuO_3$ . The models are presented in the nonmagnetic phase (spin-up and spin-down bands have no energy split).

approximately 0.5 eV. This means that this shift should be included in conductivity calculations to obtain the same results as the paper.

### 5.1.2 *$SrRuO_3$ monolayer*

Calculations of the Berry curvature of a 3D $SrRuO_3$ structure were performed in 2003 by Fang et al. [41], yielding the following result at $k_z = 0$ (Fig.19). Groenendijk et al. present numerical results under the form of band-structures, conductivity calculations and spin-polarizations. Explicit figures of Berry curvature calculations are limited to the negative-parity spin-orbit-parity-symmetric $SrRuO_3$ Hamiltonian. They show how dimensionality has affected the Berry curvature in Fig.37.

Despite the Berry curvature of the $t_{2g}$ bands being displayed separately, we can still compare the $\Gamma$ point value between Fig.19 and Fig.37: clearly, the near-degeneracy at low $\boldsymbol{k}$ is lifted and the bulk of the Berry curvature signal is shifted elsewhere in k-space.

The same bands are imaged numerically as a point of comparison in Fig.38.

We note a difference in the first two energy levels: an extra and opposite feature appears around $\boldsymbol{k} = (0, 0)$. This is due to the way Scipy manages and sorts eigenval-

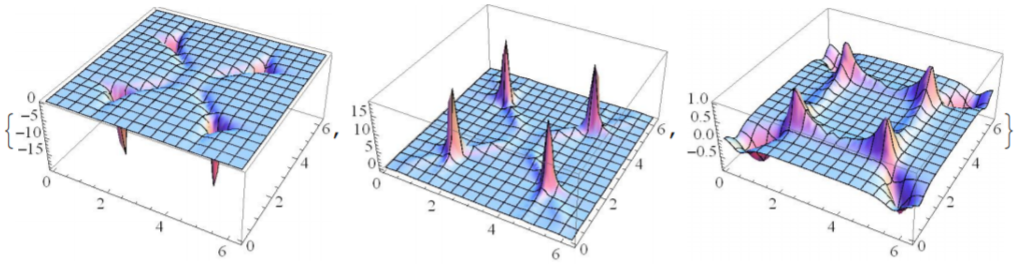

Figure 37: Berry curvature of the three negative spin-orbit-parity-projected $t_{2g}$ bands of monolayer $SrRuO_3$ , ordered by increasing energy [45].

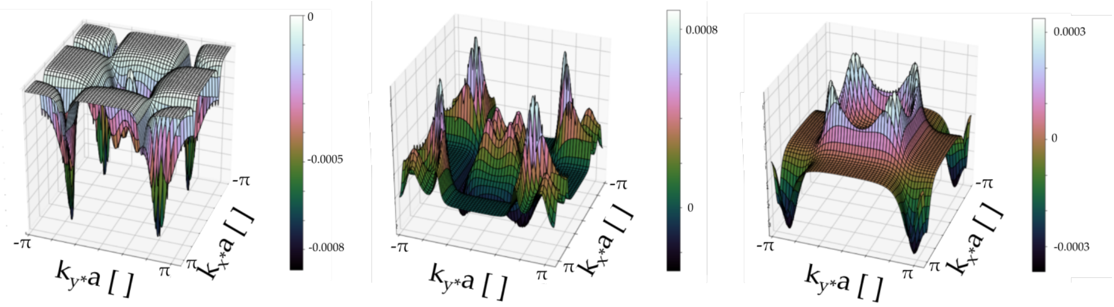

Figure 38: Berry curvature of the three negative spin-orbit-parity-projected $t_{2g}$ bands of monolayer $SrRuO_3$ , ordered by increasing energy; Kwant numerical simulation. Note that the axes are different from the paper simulation.

ues and eigenvectors. Eigenvalues are sorted in ascending order, which results in the energy band losing its connection to the orbital states. This is exemplified by switching the SOC on and off, as pictured in Fig.39. In Fig.39 a) and b) we see the eigenvalues are sorted into bands from lowest to highest at all point in k-space. However, c) shows the actual repartition of eigenvalues according to orbital contributions. What this means is that if the onsite term as well as the hopping to and from an orbital were removed,

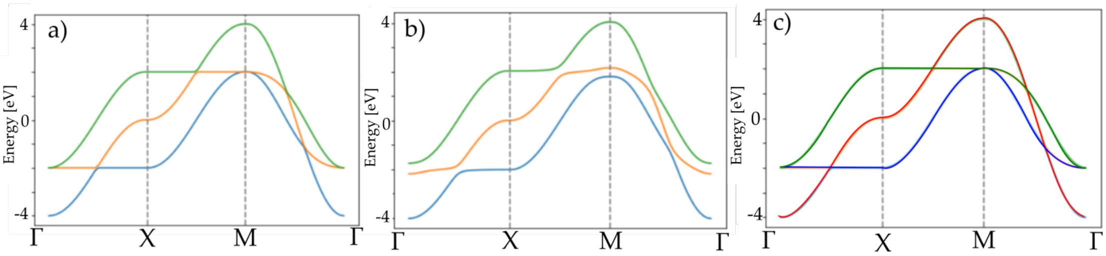

Figure 39: Dispersion of the three negative spin-orbit-parity-projected $t_{2g}$ bands of monolayer $SrRuO_3$ . For a), b) colors exemplify bands as separated by Scipy; for c) colors identify bands from the orbital basis. SOC is switched on only for b).

it would remove one of the orbital bands in c) as opposed to one of the bands in a). Comparing a) and c), we see that the top and bottom Scipy bands have the character of two of the orbitals, and the middle Scipy band is a combination of all three. As such, we cannot compare Fig.37 to Fig.38 directly without taking this into account.

The Scipy bands can still be used in calculations, as the goal of the simulations is to calculate the AHE conductivity. This is done by including states below the Fermi level, completely independently of what orbital they originated from. As such, we can use Scipy's bands but have to keep in mind that they do not retain the entire physical significance of the model when considered individually.

The $SrRuO_3$ model will be an integral part of our analysis, since the thin $SrRuO_3$ film will be the experimental focus. The surrounding materials in the devices, such as the $SrTiO_3$ substrate and the $LaAlO_3$ capping layer have the capacity to affect the $SrRuO_3$ dispersion at their interfaces, and as such are also interesting to model.

### 5.1.3 *$SrTiO_3$ -$SrRuO_3$ bilayer*

Modeling a bilayer in principle requires the addition of the third dimension, making Berry curvature analysis $k_z$-dependent. $SrTiO_3$ bands are located above the Fermi level of $SrRuO_3$ , and thus are expected to not contribute to transport in any significant way. However, the Berry curvatures one obtains show changes from the $SrRuO_3$ monolayer, as exemplified in Fig.40. Comparing the Berry curvatures for the $SrRuO_3$ monolayer and the $SrRuO_3$ -$SrTiO_3$ bilayer reveal that the $SrTiO_3$ does have an important effect on the Berry curvature. Its full relevance to our study arises precisely from the fact that its bands do not contribute to the AHE signal. Since $LaAlO_3$ bands are also above the $SrRuO_3$ Fermi level, this $SrTiO_3$ model can provide some insight into the $LaAlO_3$ -$SrRuO_3$ interface in addition to the $SrTiO_3$ -$SrRuO_3$ interface.

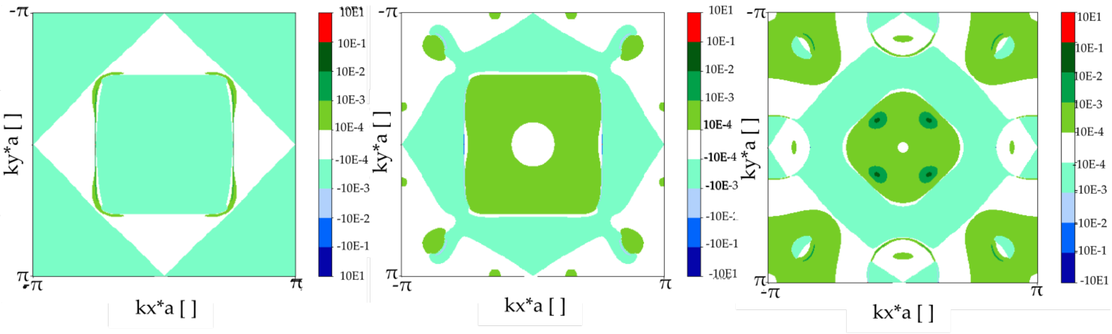

Figure 40: Berry curvatures for the three lowest energy levels of the simulated $SrTiO_3$ -$SrRuO_3$ bilayer at 0.5 eV spin splitting. A norm is used for clarity. ZBR partition is $400 * 400$.

### 5.1.4 $SrIrO_3$ -$SrRuO_3$ bilayer

Groenendijk et al. [45] study a double-loop scenario in the AHE signal, as pictured below:

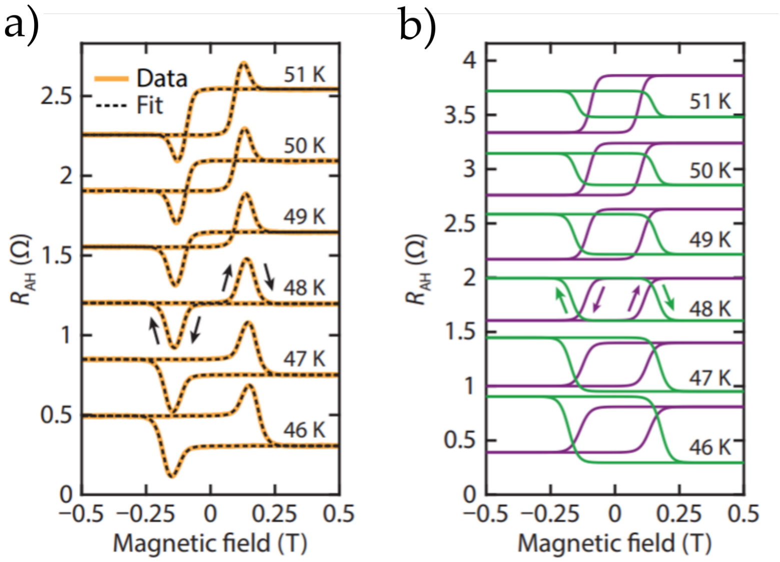

Figure 41: $SrTiO_3$ (substrate)/$SrRuO_3$ (4 u.c.)/$SrIrO_3$ (4 u.c.) data decomposition into double loops. a) The OHE-subtracted AHE data with double loop fit b) Double loop simulations of two anomalous Hall channels [45].

In their paper, they theorize the presence of two AHE channels of opposing sign that would explain the signal shape apparent in Fig.41 a). Others have attributed this to the topological Hall effect (THE), associated to topologically non-trivial spin textures such as skyrmions [69] [62]. However, sample-to-magnetic-field angle-dependent measurements [86] would provide evidence against the skyrmion explanation. Although the double-channel picture is a phenomenological rather than quantitative model, it provides credible qualitative reasoning for the shape of the AHE signal.

The focal point of their analysis is the comparison of the positive AHE contribution from a $SrIrO_3$ -$SrRuO_3$ -$SrIrO_3$ sample from 35 K to 58 K to the negative AHE contribution of the $SrTiO_3$ -$SrRuO_3$ -$SrTiO_3$ sample at the same energy range [45]. This would imply that the double-loop phenomenon is purely interface-driven. Thus, although it will not be included in our comparison to experimental data here, the $SrIrO_3$ -$SrRuO_3$ interface provides an interesting playground for exploring the AHE conductivity in $SrRuO_3$ .

The parameters for obtaining experimental data include the Fermi level shift, the magnetic field and the temperature. The Fermi level shift can be included in our measurements as the inclusion of states below a value different from 0 (the Fermi level is set to 0). The magnetic field phase is not a geometric phase, and thus does not need to be included in the tight-binding model directly. Instead, magnetic field and temperature manifest in the magnetization function $M(B, T)$. For the thermal magnetization, we use the same function as in Ref.[45], the Stoner model for itinerant ferromagnets:

$$M_1(T) = M_0 \left[1 - (\frac{T}{T_C})^2\right]^{\frac{1}{2}} \tag{24}$$

A Heaviside-type function can be used for the magnetic-field-dependent portion of the magnetization. However, a better alternative might be a non-infinite slope at the transition point. This can be done with two offset Langevin or Brillouin functions, or a set of two hyperbolic tangent functions. The temperature dependence of the magnetic coercivity $B_c(T)$ is also included as a linear function.

$$\begin{cases} M_{2,down}(B,T) = M_1(T) * [\tanh(B * slope - B_c(T))] \\ M_{2,up}(B,T) = M_1(T) * [\tanh(B * slope + B_c(T))] \end{cases} \tag{25}$$

This leaves us with a relatively complete magnetization function.

Data collection is done by first generating the eigenvalue and eigenvector set for each value of magnetization. The states can then be dynamically selected by choosing the threshold that each k-space square must sum to. In this way, a colormap of the conductivity value can be made, as pictured in Fig.42. From this, it is straightforward to image the conductivity variation for any path through parameter space.

### 5.2.1 *$SrRuO_3$ monolayer*

#### 5.2.1.1 *Band structure and monopoles*

The band structure of the $SrRuO_3$ monolayer can be seen in Fig.43 In view of the discussion of the intrinsic AHE originating from avoided band crossings, we can locate where these crossings take place in k-space. Recalling the way Scipy sorts eigenvalues, we know that the bands in Fig.43 do not have a 1-to-1 correspondence to the possible states of an electron in a single orbital, but are combinations of these bands. Turning the SOC on and off, this time including spin splitting, should give us a good idea of where the orbital bands have avoided crossings. We only expect these interaction between the SOC-coupled bands, given by the following relation:

$$\lambda \cdot \left[\sigma_x \otimes L_x + \sigma_y \otimes L_y + \sigma_z \otimes L_z\right] \tag{26}$$

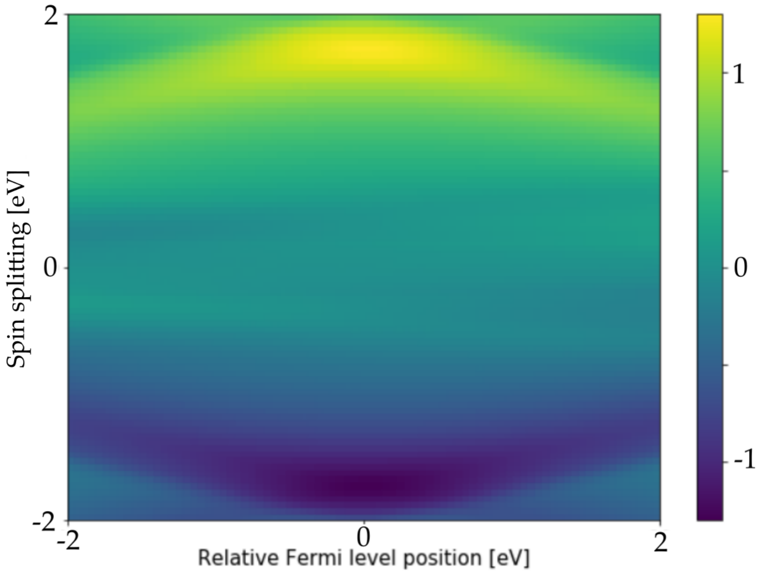

Figure 42: Colormap of conductivity in spin splitting - Fermi level parameter space for the $SrRuO_3$ monolater model.

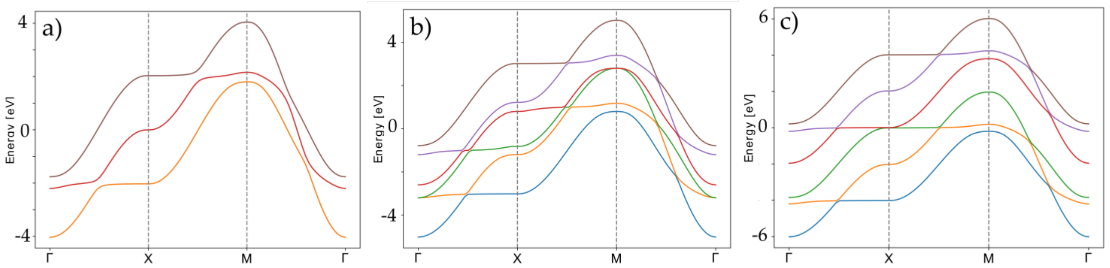

Figure 43: $SrRuO_3$ ML band structure for an spin splitting of a) 0 eV, b) 1 eV and c) 2 eV.

with $\lambda$ is half the strength of the SOC [18], $\otimes$ the Kronecker product, $\sigma_{x,y,z}$ the Pauli matrices and $L_{x,y,z}$ the orbital momentum operators. In orbital basis, the matrix form of the SOC is:

$$\begin{array}{c} |\uparrow, yz\rangle \\ |\uparrow, xz\rangle \\ |\uparrow, xy\rangle \\ |\downarrow, yz\rangle \\ |\downarrow, xz\rangle \\ |\downarrow, xy\rangle \end{array} \begin{pmatrix} 0 & -i\lambda & 0 & 0 & 0 & \lambda \\ i\lambda & 0 & 0 & 0 & 0 & -i\lambda \\ 0 & 0 & 0 & -\lambda & i\lambda & 0 \\ 0 & 0 & -\lambda & 0 & i\lambda & 0 \\ 0 & 0 & -i\lambda & -i\lambda & 0 & 0 \\ \lambda & i\lambda & 0 & 0 & 0 & 0 \end{pmatrix} \tag{27}$$

(28)

where ↑, ↓ correspond to the electron spin state and $xy$, $xz$, $yz$ are the $SrRuO_3$ $t_{2g}$ orbitals. The sets of SOC-coupled orbitals are thus $(|\uparrow, yz\rangle, |\uparrow, xz\rangle, |\downarrow, xy\rangle)$ and $(|\downarrow, yz\rangle, |\downarrow, xz\rangle, |\uparrow, xy\rangle)$. This means that we can expect both trivial (intragroup) and non-trivial (intergroup) crossings.

At no spin splitting, orbital bands for both spin values are perfectly superposed. Since there is no SOC between these bands, there can be no avoided crossings. With increasing spin splitting magnitude, the *down*-type bands will split away from the up-type. Since $SrRuO_3$ is a majority down-spin ferromagnet, down spins see a reduction in energy with increasing exchange coupling, while up spins have to pay an energy cost; Fig.43 shows this process. Avoided crossings will occur when two SOC-coupled bands start to cross. We exemplify this in Fig.44 by switching the SOC on and off for a spin splitting of 0.5 eV.

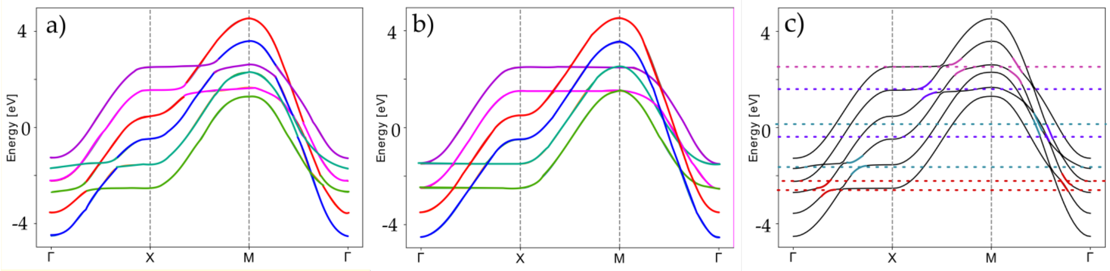

Figure 44: $SrRuO_3$ monolayer crossings along tetragonal high-symmetry trajectories. Color is used to visualize separate orbital character. a) with SOC b) without SOC c) locations of anti-crossing pairs; dotted lines of the same color indicate a pair of Weyl nodes of opposite chirality. The tetragonal high-symmetry points are illustrated in Appendix 8.1.

In Fig.44, we see the locations of anti-crossings along the main high-symmetry directions. Other crossings are likely to exist elsewhere in k-space. Fig.44 however can serve as a useful illustration of a key concept. We see that most anti-crossing pairs are not both located at the same energy level. This means that the occupation of one of these pairs will result in an anomalous velocity contribution that wo not be erased by the simultaneous equal and opposite contribution that would come from occupying the pair.

### 5.2.1.2 *Berry curvature*

We can expand beyond the high-symmetry points to the entire ZBR, which repeats periodically in $2\pi$. In the simulations, the lattice parameter is set to one. This means that the periodicity in k-space is reduced to $2\pi/a = 2\pi$ in both lattice directions. In this fashion, we can spot points of avoided degeneracy by the large Berry curvature localized in certain k-space points.

In this subsection, 'bands' refer to the Scipy lowest-to-highest sorted bands, and not the orbital-associated bands; this is because the calculation is done with the Scipy bands. As such, the analysis of Berry curvature is limited in its physical meaning when done band-by-band. It should, however, serve to reveal where points of large Berry curvature are.

An important question remains the necessary k-space partition precision required to calculate the Berry curvature. This question will be of particular importance in the next subsection, when the conductivity is calculated. The conductivity calculation relies on the precise inclusion of states below the Fermi level and on the integration on small enough loops that do not wash out important anholonomy angle contributions. The calculation of the Fermi level for each band only relies on the latter, and it is difficult to appraise beyond what visual means can tell us. As such, this subsection will comprise of a first look at the Berry curvature over all k-space with a partitioning of $300 * 300$. Additionally, it will be most informative to once again consider a spin splitting of $0.5eV$, since it will then be possible to compare anti-crossing locations with subsection 5.2.1.1.

The Berry curvature of the 6 bands associated to the 6 orbitals, using the code in Appendix 7, can be seen in Fig.45. From Fig.45 we can deduce that the avoided crossings are located principally on the high-symmetry points. We thus know, using the information obtained in subsection 5.2.1.1, where the avoided crossings are.

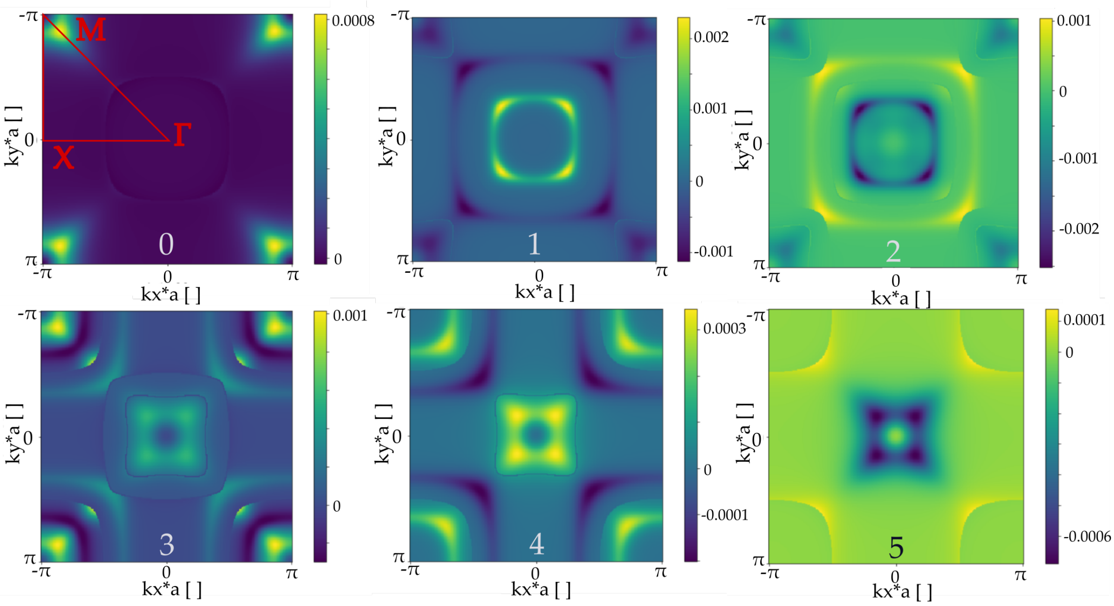

Figure 45: Berry curvature over the first ZBR for the six $SrRuO_3$ bands. Numbers indicate Scipy order. On the zeroth band, the tetragonal high-symmetry trajectories are indicated in red. k-space partitioning is $300 * 300$.

From Fig.45 it appears that bands 0 and 1 share an additional avoided crossing at $M$, which was not accounted for in Fig.44. However, since the crossing pair is likely very close together near $M$, it is unlikely that their effects do not cancel simultaneously.

Fig.44 indicates that the avoided crossings most likely to be affected by the top gate experiment are the ones closest to $E = 0$, as their partners are separated in energy by 1 eV or more ('blue' and 'purple' crossings). Their position close to the Fermi level implies that a top gate, both positive and negative, could have an important effect on the Berry curvature signal.

The avoided crossings are prone to shifting in k-space and in energy with changing values of spin splitting. The conductivity calculation will reveal how the signal is affected.

### 5.2.1.3 *Intrinsic anomalous conductivity*

Only states occupied by electrons can manifest in transport. As such, studying the conductivity of an entire Scipy band by itself makes little sense, as the bands are not separated by a gap. Instead, the conductivity is calculated by the inclusion of all states below the Fermi level of all the bands together. Fig.46 presents a visual example.

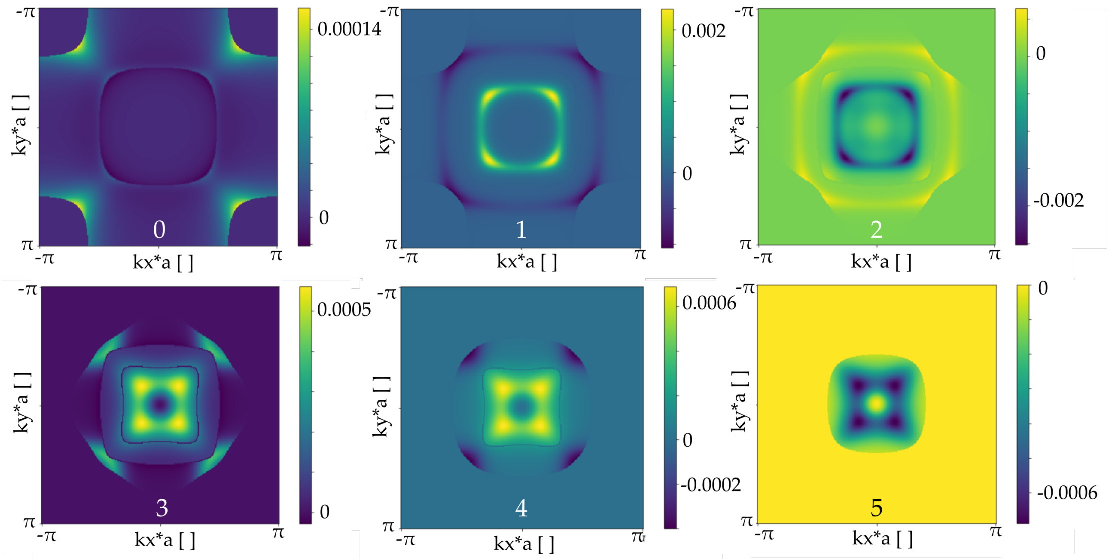

Figure 46: Berry curvature for states below $E = 0$. Numbers indicate Scipy order. k-space partitioning is $300 * 300$.

The partitioning of k-space has been limited to $300 * 300$. This is due to the appearance of a signal anomaly visible at higher precision; the details are in Appendix 8. Comparing Fig.46 and Fig.45, there is a clear signal exclusion that takes place. As such, as long as the pair anti-crossings are not occupied simultaneously, an AHE signal will be produced by the non-compensated anti-crossings.

Using the colorplot seen in section 5.2, we can visualize how the changes in chemical potential and magnetization affect the AHE signal. A note should be made about the realistic Fermi level shifts that can be achieved. Shimizu et al. [71] conducted ion-gating experiments on $SrRuO_3$ thin films. The ionic liquid used had a capacitance of about $10^{-5}Fcm^{-2}$. For a 5 u.c. $SrRuO_3$ film they predicted a carrier change of $\pm 2.5 * 10^{14} cm^{-2}$ for an applied gate voltage of $\pm 4V$, yielding a change of about $\pm 6\%$ in the longitudinal resistivity. Experimental results showed changes of $+2\%$ and $-5.5\%$. The change in anomalous conductivity was much larger, reaching $\pm 40\%$ at 2 K [71]. The $SrRuO_3$ -$LaAlO_3$ films prepared for this report have a capacitance of $1.05 \cdot 10^{-11}$ F. $\pm 4V$ results in an accumulation of charge of $\pm 2.6 * 10^8$ electrons on the surfaces of the dielectric. On the surface of the large Hall bar devices made for this experiment, this yields a charge carrier concentration of $6.5 * 10^{12} e/cm^2$, about two orders of magnitude less than Ref.[71]. Our experimental results will show a $\pm 2\%$ change in the anomalous conductivity for a 5 u.c. $SrRuO_3$ film at 10 K, and a $\pm 17\%$ change at 1.5 K (Fig.69). A $\pm 26\%$ is seen for the semiconducting $SrRuO_3$ film, showing that while the effect is reduced compared to ionic gating, the resulting change is of the same order for the semiconducting film with a solid gate, due to the larger field penetration depth. The density of states at the Fermi level would have to be considered in order to connect this to a Fermi level shift. As such, the link from model to experiment will have to be retroactive; considering a shift spread of $\pm 2\ eV$, since that is the total energetic spread of the $SrRuO_3$ bands at 0.5 spin splitting (cf. Fig.43), and comparing the observed behavior to the model, it might be possible to glean the effect of the top gate in terms of a Fermi level shift. Fig.47 shows that changing the Fermi level has the power to reverse the sign of the AHE signal at low spin splitting magnitude ($< 0.5$). This effect arises for spin splittings of 0.5 eV and higher, and for relative Fermi level of -0.5 eV and lower. This Stoner splitting is within the correct magnitude for $SrRuO_3$ [31] [73] [40]. As such, we can realistically expect to manipulate the AHE sign of $SrRuO_3$ .

Using the temperature- and magnetic field-dependent magnetization function as described in section 5.2, and associating each point to a conductivity value from the colormap, Fig.48 is obtained. Fig.48 is qualitative in that the time-dependent coercivity function $B_c(T)$ is taken as a relative coercivity, $1 - T/Tc$. As such, the values of the magnetic field are not important but are included as a general guide. The discreet jumps in the signal are due to the discreet nature of the signal values in the colormap.

The peak features are present for higher values of temperature, visible until about 80 K, or slightly more than halfway to the selected Curie temperature of 150 K, as visible in Appendix 8.3. However, we should only consider the tight-binding model as qualitative guidance for low temperatures. This argument merely lends some robustness to the signal: its features do not disappear at temperatures immediately higher than 0 K, meaning that it is not unrealistic to hope to observe similar features at low temperatures.

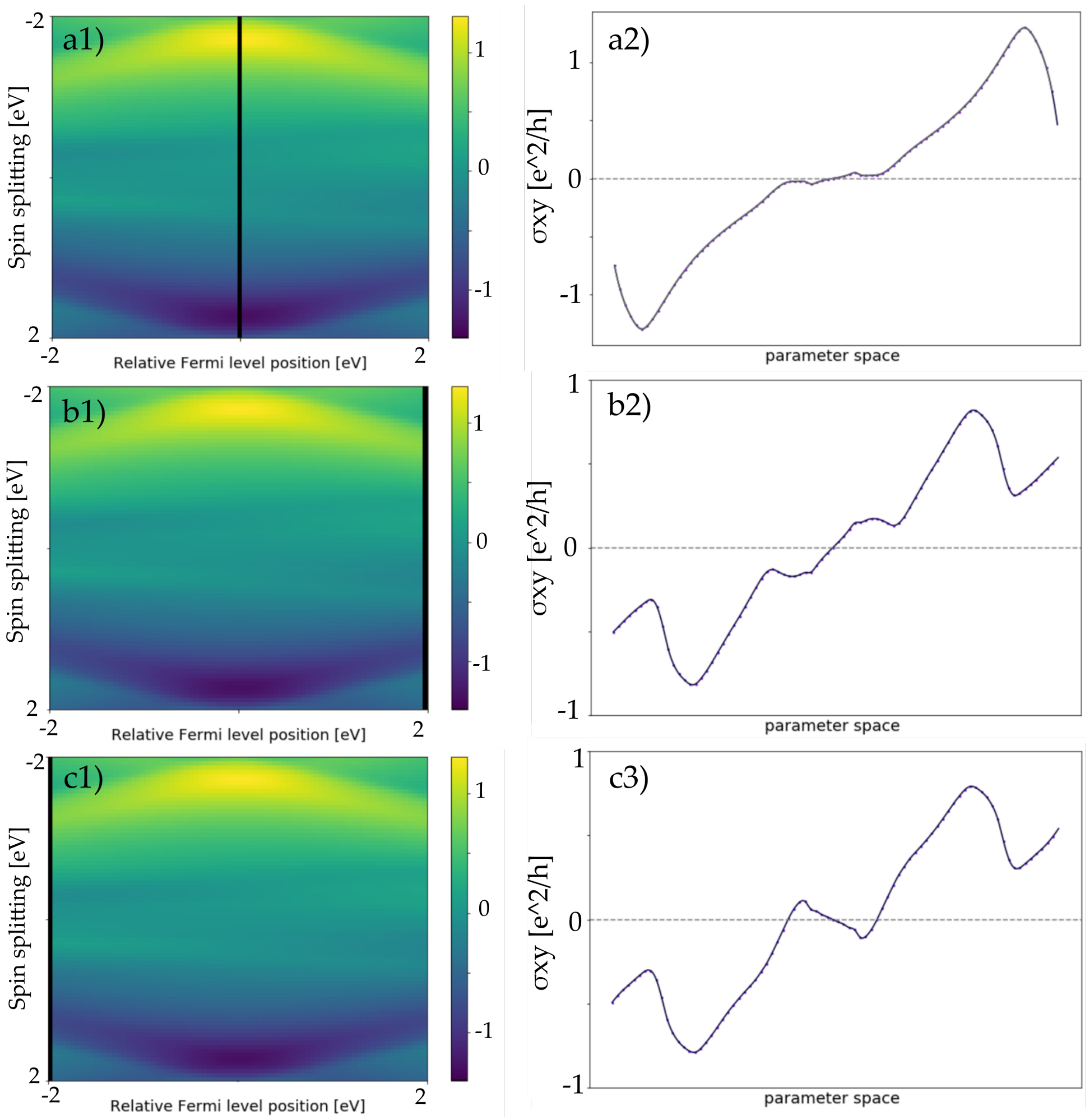

Figure 47: AHE signal as a function of spin splitting for fixed values of the chemical potential. Black lines on a1), b1) ,c1) indicate path taken in parameter space, and a2), b2), c2) show the AHE signal strength along the paths. k-space partitioning is $300 * 300$.

The features of the AHE signal change with the relative Fermi level, as expected from Fig.47. The signal is affected primarily in the following way at low temperatures, regardless of the sign of the shift: the saturation value of the signal is reduced, secondary peaks of opposing sign, and at low absolute values of magnetization there is a continuous evolution of magnetic switching. As expected from what was determined by Fig.47, we observe that the positive Fermi level shift induces no sign shift in the AHE signal at low magnetization amplitude, but rather two bumps. The nega-

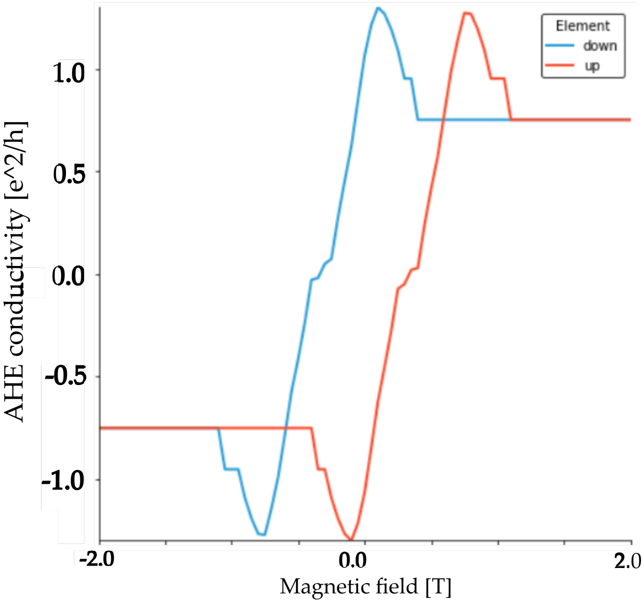

Figure 48: AHE conductivity signal of the $SrRuO_3$ monolayer model at 0 K and 0 eV relative Fermi level shift.

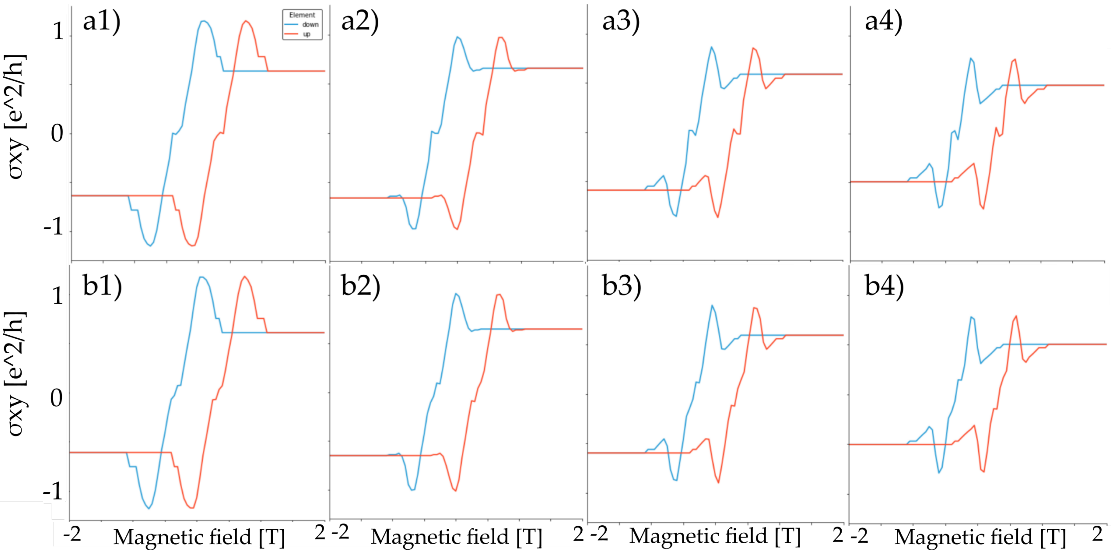

Figure 49: AHE conductivity signal of the $SrRuO_3$ monolayer model at 0 K. Relative Fermi level shift a1) 0.5 eV, a2) 1 eV, a3) 1.5 eV, a4) 2 eV, b1) -0.5 eV, b2) -1 eV, b3) -1.5 eV, b4) -2 eV.

tive Fermi level shift, where we expect to see the sign change, is increasingly visible with shift size. Fig.49 will be one of the qualitative bases with which we can approach measurements.

### 5.2.2 *$SrRuO_3$ -$SrTiO_3$ bilayer*

The $SrRuO_3$ -$SrTiO_3$ bilayer as described in [45] yields Fig.50. This model has 12 bands (the 6 $SrTiO_3$ $t_{2g}$ bands are now included). The calculation was limited in Fermi level precision (9 points instead of 81 for each of the 81 magnetization points). The signal is zero at zero spin splitting for all values of Fermi level shift, as expected. We note the presence of a sign inversion close to the Fermi level for low values of magnetization. Fig.51 reveals several surprising things. A sign reversal at low energies takes place at 0.5 eV and -1 eV, so for both shift directions. Compared to the $SrRuO_3$ model, the sign reversal at 0.5 eV here is broader and closer to the Fermi level. Since both $LaAlO_3$ and $SrTiO_3$ are insulating interfaces with $SrRuO_3$ , the $SrRuO_3$ -$SrTiO_3$ could model some behavior of the $SrRuO_3$ -$LaAlO_3$ samples, and these features should be taken into consideration. We note, however, that $LaAlO_3$ does not have $t_{2g}$ bands, unlike $SrTiO_3$ and $SrRuO_3$ .

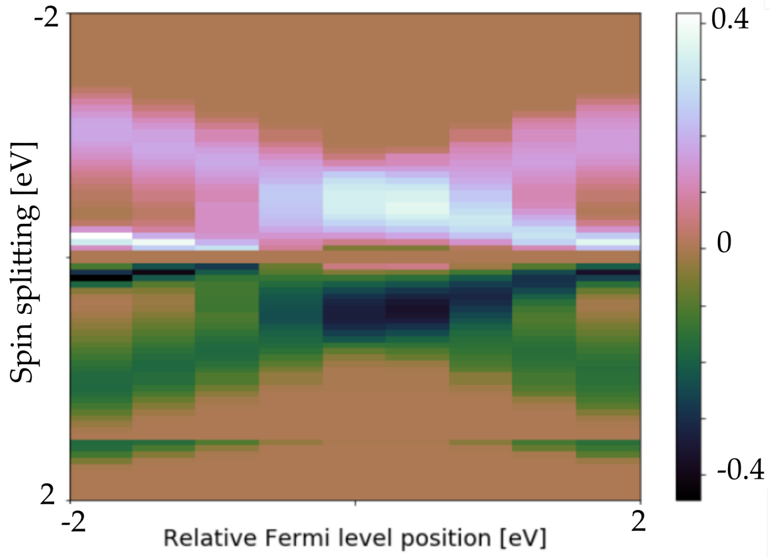

Figure 50: AHE of the $SrTiO_3$ -$SrRuO_3$ model from [45] as a function of spin splitting and Fermi level shift. k-space partitioning is $300 * 300$.

This model does have some strong qualitative problems, however; the AHE signal drops to zero above a certain magnitude of spin splitting, which is not the expected behavior [45]. Looking at Fig.36, it is likely that monopole pairs group evenly above and below the Fermi level for a certain value of spin splitting. As such, the conductivity drops to zero.

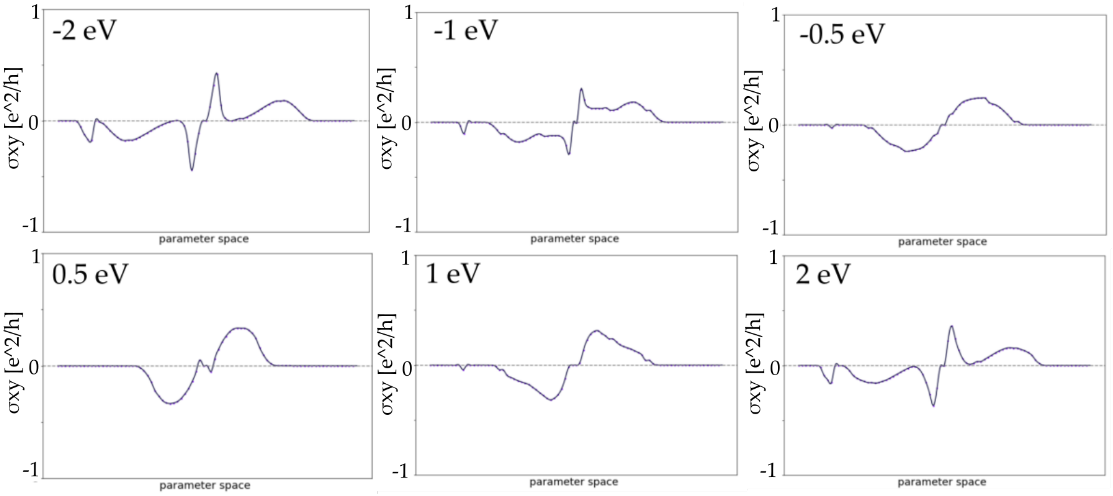

Figure 51: Magnetization sweeps of the AHE signal from Fig.50 at different values of energy shift from the Fermi level. Sweeps are done from -2 eV to 2 eV spin splitting.

### 5.2.3 $SrRuO_3$ -$SrIrO_3$ *bilayer*

Unlike $SrTiO_3$ , $SrIrO_3$ has tight-binding bands that contribute at the Fermi level. Fig.36 a) shows how dense these states are at the Fermi level. Simulations of the AHE signal with varying k-space partitioning precision and spin splitting data points demonstrate the need for high precision. Fig.52 shows vast signal differences at low energies. Since we are interested in the Fermi level and its close vicinity, a high-resolution calculation was performed between -0.5 and 0.5 eV for the spin splitting, while keeping a 4 eV chemical potential sweep, for completeness. Of course, since $SrIrO_3$ is also metallic, a top gate on a $SrTiO_3$ -$SrRuO_3$ -$SrIrO_3$ sample would a lower chance of affecting the $SrRuO_3$ , as an electric field would be mostly screened before attaining it. However, there is the possibility of back-gating the sample, as shown in Ref.[64] to remarkable results, including the reversal of the AHE signal. Even though it will not be an experiment, the $SrRuO_3$ -$SrIrO_3$ model is still relevant to our numerical study of the AHE signal in $SrRuO_3$ . Fig.53 shows that the precision may still be too low, due to the appearance of discontinuous peaks, perhaps similar in origin to the nonphysical peak seen for the $SrRuO_3$ model (cf. Appendix 8). Two signal crests of opposite sign are hosted in the model from -1.5 eV to 1.5 eV. Since the model excludes ferromagnetic ordering for the $SrIrO_3$ bands, the AHE signal is entirely attributable to the $SrRuO_3$ bands. As such, we should see similarities between the signals of the $SrRuO_3$ model and the $SrRuO_3$ -$SrIrO_3$ model.

Close to the Fermi level, we see a switch in the signal sign at low magnetization. This effect is more pronounced for positive Fermi level shifts, reappearing after 1.5 eV. For negative Fermi level shifts, the effect disappears at -0.5 eV before briefly reappearing.

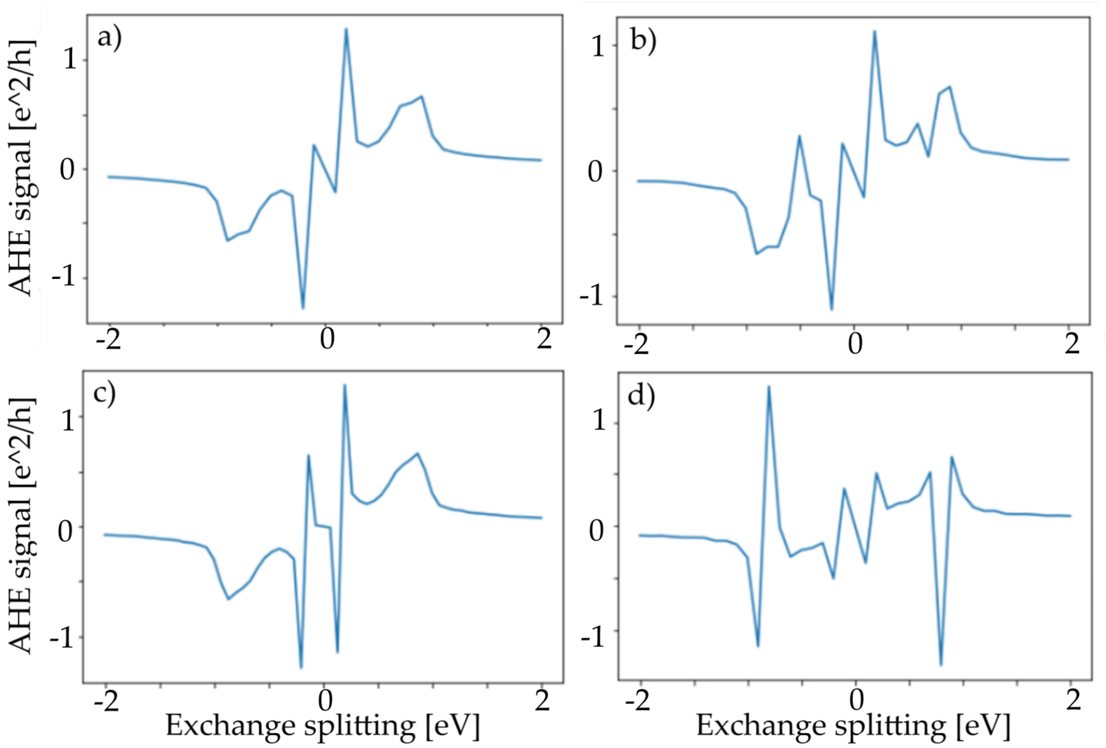

Figure 52: AHE of the $SrIrO_3$ -$SrRuO_3$ model from [45] as a function of spin splitting at the Fermi level. k-space partitioning is a), c) $300 * 300$, b) $200 * 200$, d) $100 * 100$ and number of data points is a),b),d) 41 and c) 61.

This complicated signal is no doubt onset by the strong SOC induced in the $SrRuO_3$ by the proximity with $SrIrO_3$ , leading to complex interplay of bands not seen for lower values of SOC.

It would be interesting to attempt to modify the Fermi level of a $SrRuO_3$ -$SrIrO_3$ sample due to the rich low-energy reactions to the shift; however, the experimental reality would likely be quite different due to the small magnetization range over which the signal fluctuations occur, as exemplified below; the sign changes five times from -0.25 eV to 0.25 eV spin splitting close to the Fermi level, and evolves in a complex manner with Fermi level shift.

## 5.3 COMBINING CONTRIBUTIONS

In the two-loop model of Ref.[45], contributions are thought to arise from the two different interfaces of $SrRuO_3$ with other complex oxides. As such, we can combine the $SrRuO_3$ signal with the $SrRuO_3$ -$SrTiO_3$ model in order to see how the signal changes. Fig.55 reveals several interesting features. The case in which both contributions coexist at the Fermi level, originating from magnetization loops of the same shape, show

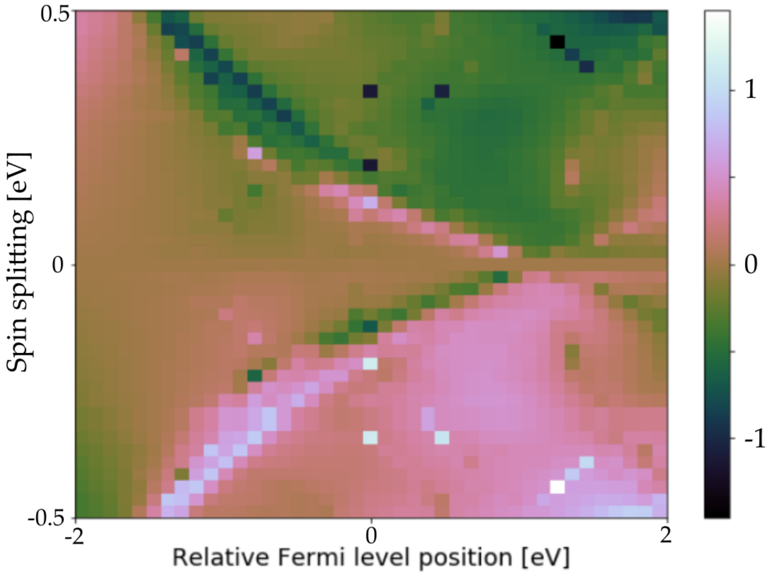

Figure 53: AHE of the $SrIrO_3$ -$SrRuO_3$ model from [45] as a function of spin splitting and chemical potential. k-space partitioning is $450 * 450$.

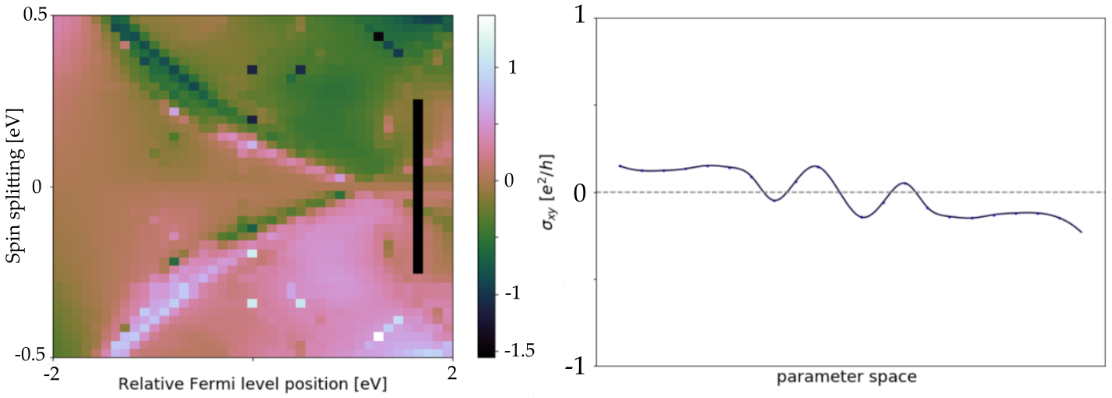

Figure 54: Magnetization sweep of the AHE signal at different values of energy shift from the Fermi level. Black line indicates path taken in parameter space.

little difference from the $SrRuO_3$ monolayer model in Fig.48. However, if the $SrRuO_3$ contribution experiences the effect of the top gate and the $SrRuO_3$ -$SrTiO_3$ contribution is unaffected, for example due to a penetration depth that doesn't span the depth of the film, low-magnetization behavior is suppressed. The clear switching signal close to zero magnetization of the accumulated $SrRuO_3$ model is sharply reduced by the presence of the unaffected $SrTiO_3$ -$SrRuO_3$ interface. Once this interface is affected, we see little difference between accumulation and depletion beyond a smaller separation of the switching for accumulation. It is interesting to note that there are now two switches for accumulation as opposed to one for the $SrRuO_3$ model.

The influence of the $SrRuO_3$ -$SrTiO_3$ signal on the total AHE signal can be considered even at the Fermi level, as pictured in Fig.55 a) and b). If the magnetic domains differ, then the consequence for the final signal is even more pronounced than if two $SrRuO_3$ loops coexisted (cf. Appendix 8.9). Since there is no direct magnetic domain information that can be obtained via the transport experiments in this thesis, and since the model can be tuned by many different parameters, this type of manipulation should be done very carefully in order to avoid using unjustifiable parameter values in order to justify an observation. Nevertheless, this model could prove to be more valuable than the $SrRuO_3$ monolayer model, as it can yield information on both the participation of the $SrTiO_3$ -$SrRuO_3$ interface to the total signal, and on the degree of depletion and accumulation present in the sample at both interfaces.

The three models display similar low-energy features, and the higher field signal signs are mutually consistent. Whereas there is no guarantee the expected features will be visible at low temperatures and magnetizations in the $SrTiO_3$ -$SrRuO_3$ -$LaAlO_3$ samples, the $SrRuO_3$ model can serve as a general qualitative guide. The joint $SrRuO_3$ -$SrTiO_3$ and $SrRuO_3$ signal will also be considered on a secondary note, due to the delicacy required in using it appropriately.

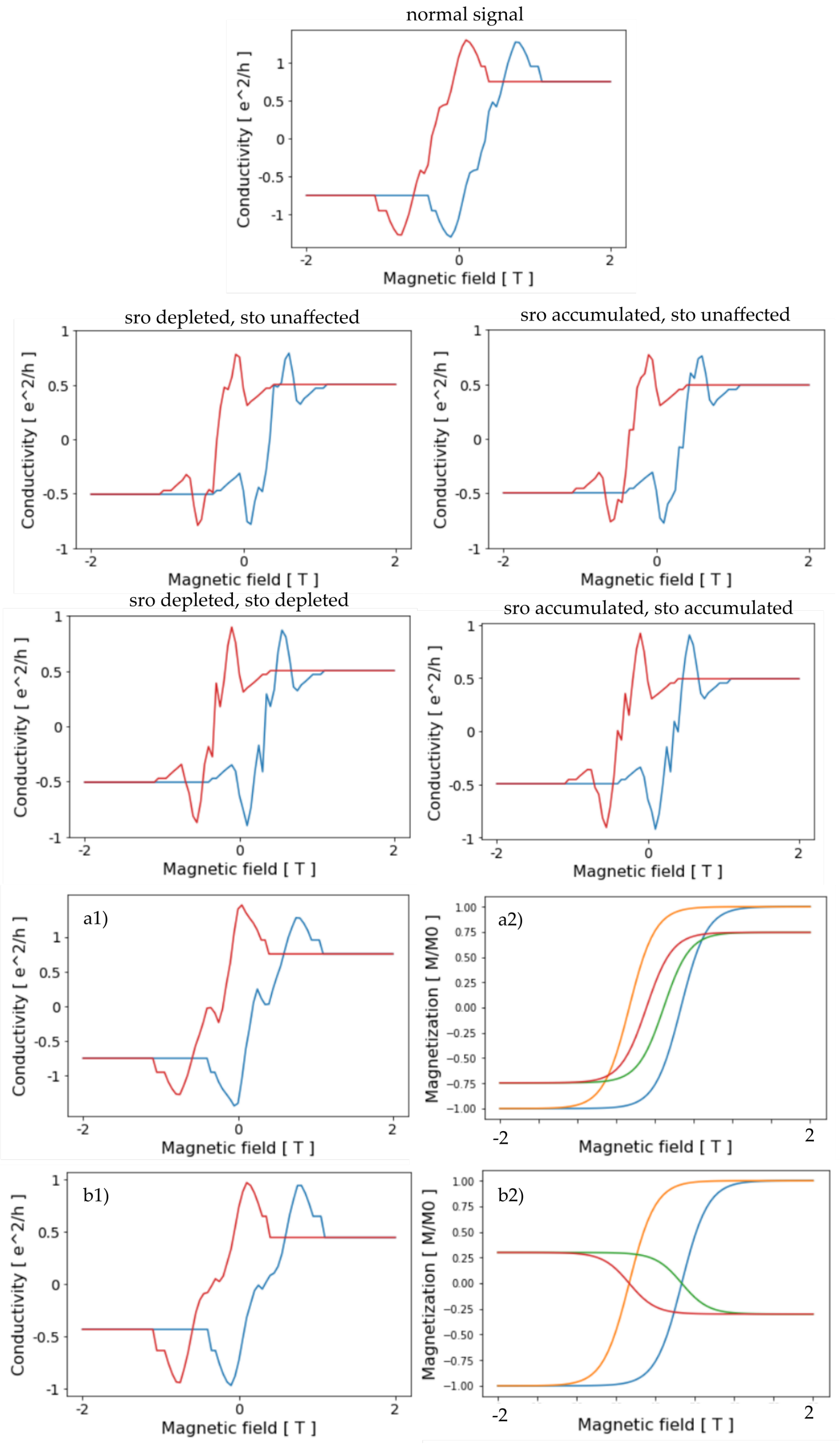

Figure 55: Numerical simulations of the superposition of the monolayer $SrRuO_3$ and $SrRuO_3$ -$SrTiO_3$ bilayer AHE signal for different depletion and accumulation scenarios. a1) Represents the signal arising at the Fermi level of both contributions from the magnetization loops in a2) where the $SrRuO_3$ monolayer signal is from the loop with larger coercivity. b1) Represents the same scenario except the $SrRuO_3$ -$SrTiO_3$ signal arises from a magnetization loop of opposite and reduced sign in b2). The $SrRuO_3$ and $SrRuO_3$ -$SrTiO_3$ contributions were considered to be of equal magnitude unless stated otherwise.

# 6 EXPERIMENTAL RESULTS

A series of transport experiments are performed in order to gauge the potential effect of a top gate voltage on the AHE signal. The analysis will focus on the samples SRO13 and SRO32, and will contain qualitative comparison of the signal shape at low temperatures to the numerical models, as well as quantitative extraction of the coercivity, OHE coefficient, and loop height obtained with magnetic field sweep experiments. Changes in coercivity can indicate changes in the magnetic state as a result for the top gate, and probe the existence of two uncoupled ferromagnetic domains as suggested by Ref.[45]. The slope of the OHE contribution can be used to calculate charge carrier density $n$ via $R_H = -\frac{1}{nec}$ [4], which in turn gives an indication of penetration depth via Eq.21. The height of the anomalous hysteresis loop at 0 T gives an indication of the state of the AHE without influence from a magnetic field, and gives the anomalous Hall coefficient $R^{AHE}$ [45].

The raw data will be analyzed qualitatively and compared to the numerical model, then quantitative data will be extracted where it is possible and reasonable to do so.

## 6.1 QUALITATIVE ANALYSIS

Due to the sensitivity of the AHE signal to magnetization, measuring it at different temperatures allows us to explore a range of behavior in the sample. However, any passing comparison to the numerical model should be restricted to low temperatures. Measurements at other temperatures can give us an idea of how the model breaks down, for example by checking which of its features are the first to go. Beyond this, they also inform us of the variety of magnetic states possible in the samples, as even small changes in the magnetization should be accompanied by a change in the AHE signal.

Hysteresis loops were obtained for SRO13 at 1.5 K and 10 K. Fig.56 shows that while the loops change with different values of the top gate, there is no clear trend to support an immediate link between the changes and the applied voltage. Charge trapping due to the low temperature could account for the jumps in signal.

At 0 and -1 V, we see the peaks associated to double AHE loops [45] or the THE [62], that we were hoping to see in the sample. These peaks then disappear as the negative top gate voltage is increased, reappearing erratically and non-repeatably (see Appendix 8.5) at -3 V and -4V, before returning in a more convincing fashion at -7 and -8 V. From Fig.57 shows very little difference between loops as a function of top gate at 10 K. It seems some features appear at -4 V; however, like other spurious features

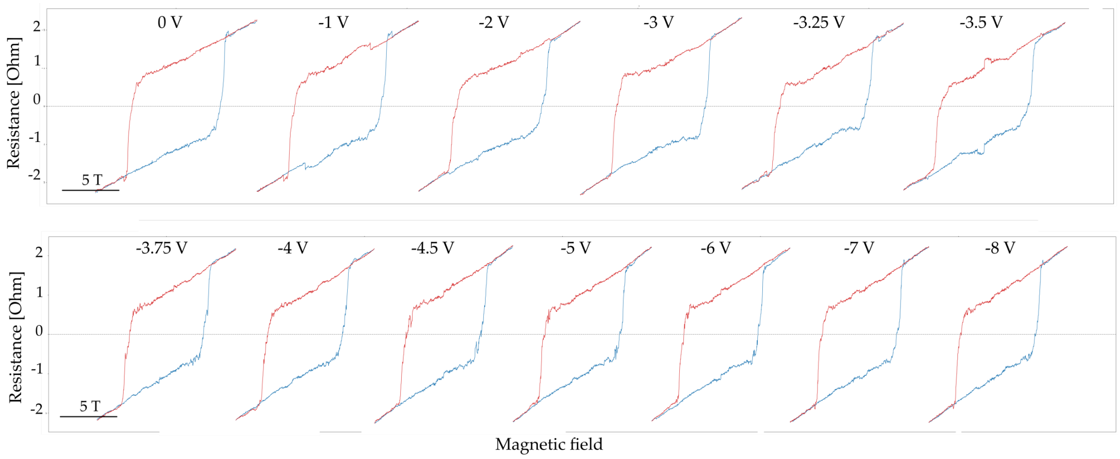

Figure 56: SRO13. Antisymmetrized anomalous Hall resistance as a function of top gate voltage at 1.5 K.

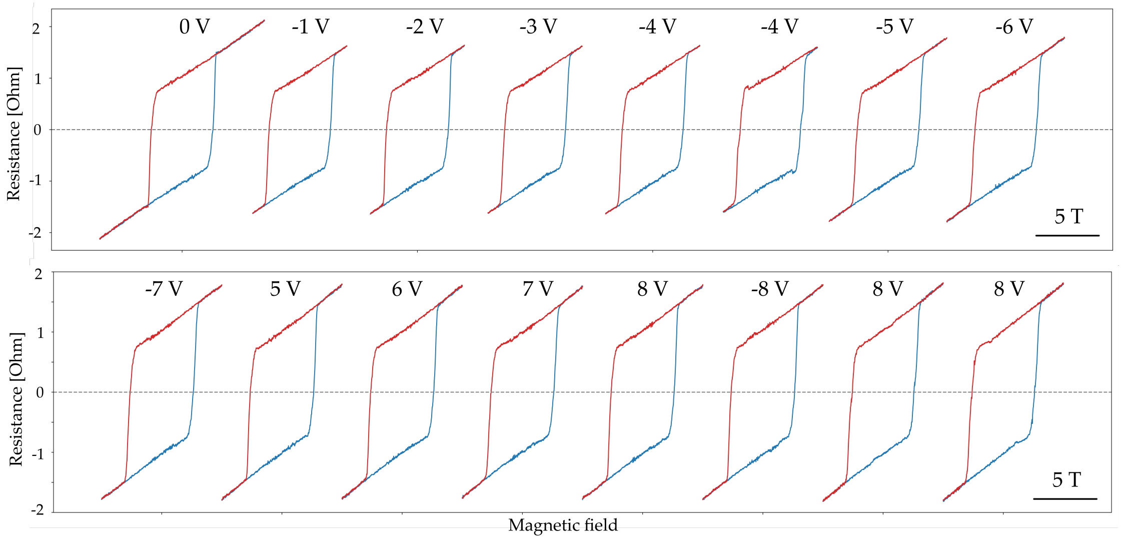

Figure 57: SRO13. Antisymmetrized anomalous Hall resistance as a function of top gate voltage at 10 K.

also visible (for example at 8 V) it was not reproducible. As there was little evidence for gate hysteresis in the previous sections, the difference between separate data sets must be in the magnetic state and the trapped charges at low temperature.

It is clear from Fig.56 and Fig.57 that the numerical model does not share the same behavior as the loops. For gated loops, this falls in line with previous considerations about the lack of significant accumulation or depletion behavior in SRO13. However, the numerical model is also not a fit at zero gate voltage.

Despite the SRO32 loops having few salvageable quantitative properties, their shape bears important qualitative information. Fig.58 shows the magnetic field sweeps for SRO32 at 30 K. For positive topgate values, a broad peak is noticeable at high fields, similar to the signal of the *SrRuO*3 -*SrIrO*3 4 ML sample from Matsuno et al. [62]. The negative top gate has little effect at high fields until at -5 V, a long tail appears and the loop only barely closes at 2 T. The coercivity of the hysteresis loop changes as a function of gate voltage. As shown in Appendix 8.12, the coercivity does not seem to follow a consistent pattern with gate voltage, but it is observably connected to other features of the signal shape. In Fig.58, a change in coercivity is accompanied by a change in loop height: smaller coercivity is associated to taller loops, whereas larger coercivities are associated to smaller loops. We see that the positive top gate curves with higher coercivity have the broad peak at high field, whereas those without have lower coercive fields. We also see that negative top gate curves affected at high fields, like -3 V and -5 V, are also associated to larger coercive fields, of the same magnitude as the large coercivity for positive top gate. This directly correlates the peak to a change in magnetic state to high-field effects. The top gate may be varying the magnetic saturation of the sample.

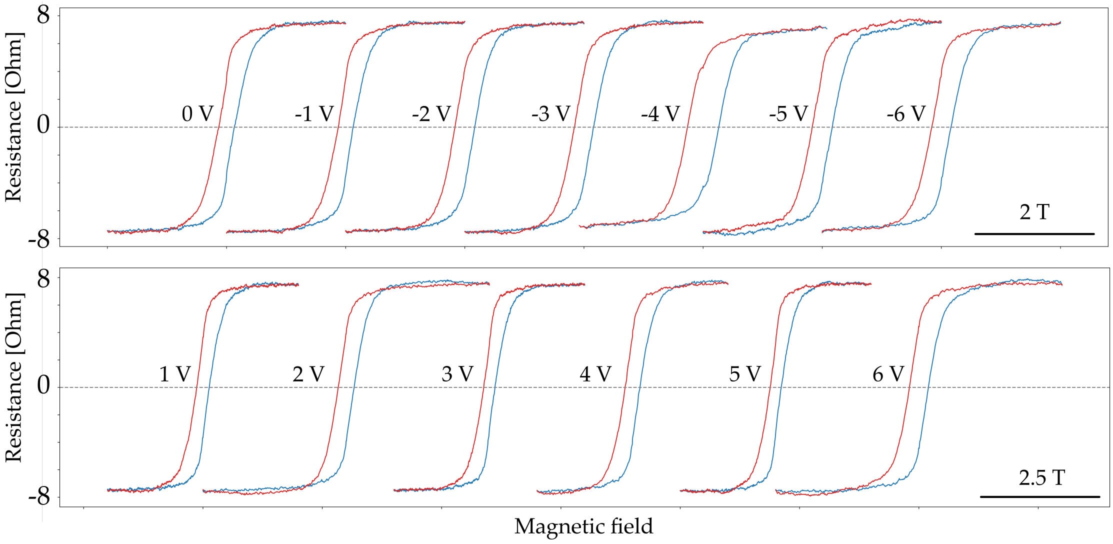

Figure 58: SRO32. Antisymmetrized anomalous Hall resistance as a function of top gate voltage at 30 K.

A close point of comparison for the 30 K data could come from 25 K measurements. We see from Fig.59 that the 1 V curve has both a wide tail and the largest coercivity. Both 3 and -3 V have broad high-field peaks; however, only -3 V shows a spike in coercivity, whereas 3 V shows no difference from -2 V.

Data was also gathered at 15 K. Fig.60 shows the signal coercivity oscillating. The periodically changing nature of the high-field behavior pictured in Fig.60 could sup-

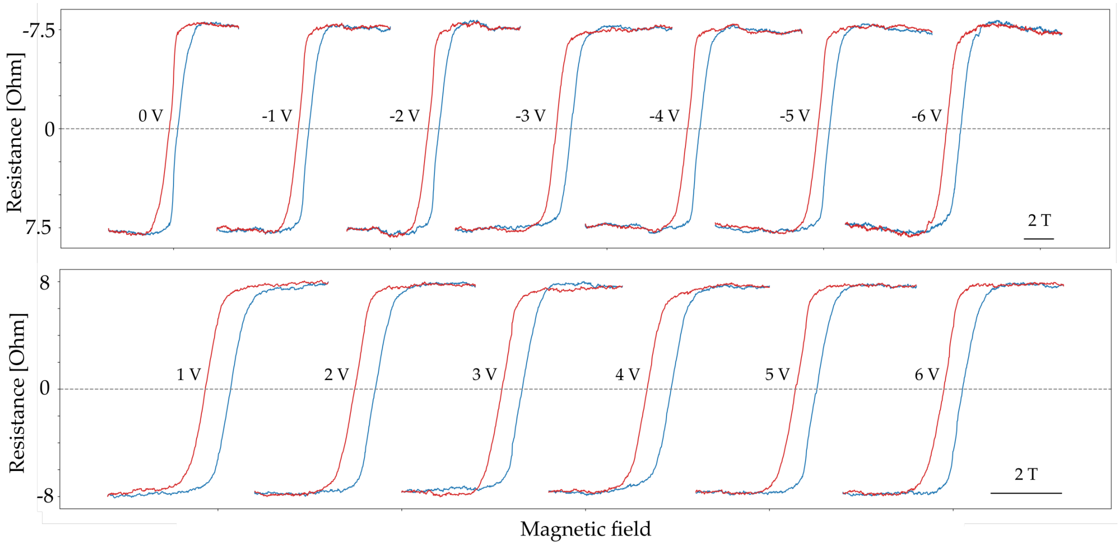

Figure 59: SRO32. Antisymmetrized anomalous Hall resistance as a function of top gate voltage at 25 K.

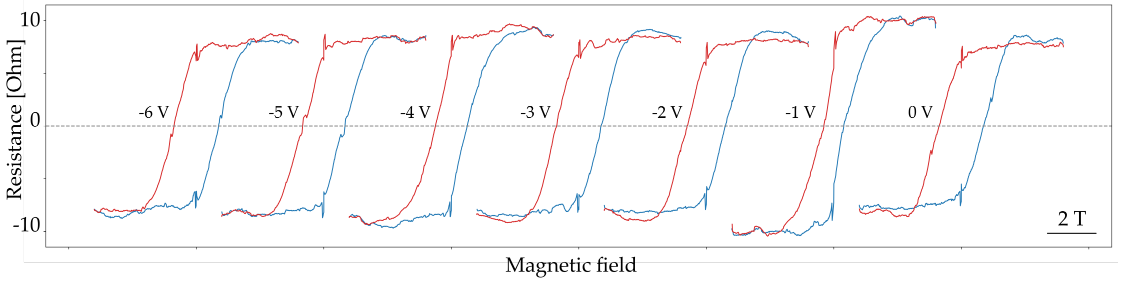

Figure 60: SRO32. Antisymmetrized anomalous Hall resistance as a function of top gate voltage at 15 K. Data is averaged over neighbouring points to improve clarity.

ply an origin, however as of yet unexplained, to a trend in coercivity as explored in Appendix 8.12.

At -6 V, we see a low-magnetization signal switch close to zero. The switch does not occur at zero, probably due to another magnetic contribution. At -5 V, the switch occurs closer to zero magnetization. As the signal spans two separate measurements, it can be hypothesized to arise from the low-magnetization switching we expect from our model.

The sharp peaks at zero field visible in Fig.60 are due to mismatches in the signal as the loop is closed. The culprit is probably the behavior at high field. One possible cause for this behavior is in-plane magnetization contributions that cannot be reversed with an out-of-plane field, as has been observed in $SrRuO_3$ nanostructures [74]. The loop height is difficult to ascertain, but the overall signal strength at low field seems to generally increase as the coercivity decreases. Fig.61 compares the raw data to the

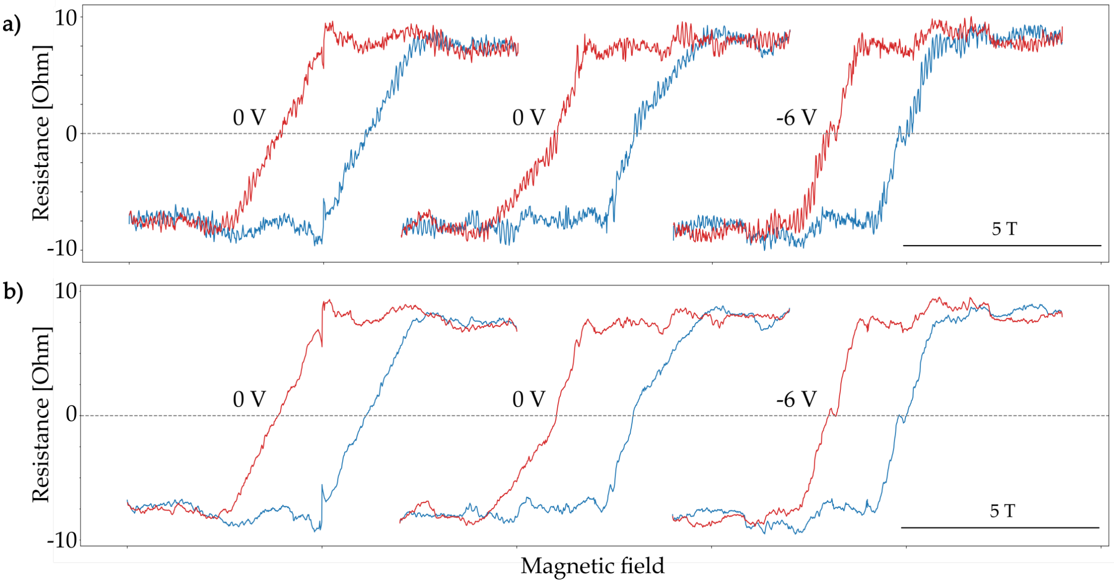

Figure 61: SRO32. Antisymmetrized anomalous Hall resistance as a function of top gate voltage at 10 K. a) Raw data and b) averaged data. Average is done over 8 adjacent points.

averaged data. The averaging serves to eliminate or at least reduce noise due to thermal fluctuations, that tend to be periodic over a few data points. (cf. Appendix 8.7). Both datasets are included in order to discern whether the low-magnetization switch signal seen at -6 V is legitimate or a measurement artifact. Since the signal bump is of the same magnitude as the noise around it, it would most likely be unfair to say the averaged data is representative of the sample's response. However, we saw that at -5 and -6 V at 15 K, the switching at low magnetization could be observed reasonably clearly, which could confirm the legitimacy of the averaged signal. Comparing this to our model however, sees that this switch is expected for shifts below the Fermi level (positive top gate) and not for shifts above the Fermi level (cf. Fig.49). As such, some doubt should be placed on either the validity of either the model or on the AHE signal at low temperatures.

Cooldowns revealed the lowest temperatures at which the AHE signal was still reliable; this threshold varied from 4.6 to 7 K (cf. Appendix 8.8), indicating that identical magnetic states are not necessarily recovered at low temperatures. This leads to a wide range in signal quality, as evidenced by Fig.62: The odd shape of the measurement at -3 V in particular puts into question the validity of the features garnishing the hysteresis loop. The two 0 V measurements were done sequentially, and the difference between the two signals is noticeable. Black arrows indicate features that appear in each measurement, and red arrows indicate shared features that appear for the nega-

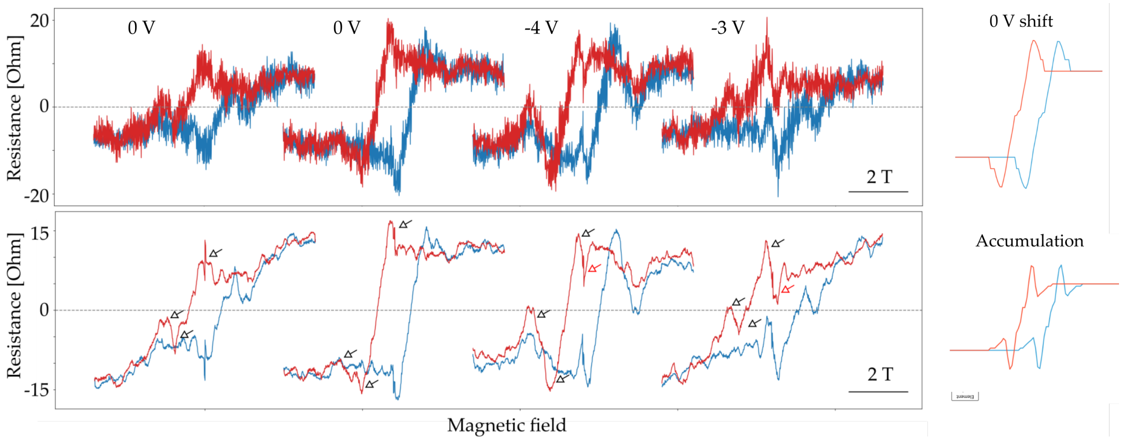

Figure 62: SRO32. Antisymmetrized anomalous Hall resistance as a function of top gate voltage at 5 K. a) Raw data and b) averaged data. Average is done over 8 adjacent points. For b), the high-field slope was corrected in an attempt to restore a hysteresis-loop shape. Numerical model predictions are included on the right.

tive top gate peaks. Comparing the indicated features to the predictions of our model, the predicted qualitative behavior could be confirmed in the 5 K measurements.

Before making such a claim, more data should be considered. Since the sweeps at 5 K were quite shaky, sweeps at 7.5 K were performed. The measurements are still unstable, as is made clear from the loop shapes changing despite the temperature only changing by one degree. When the top gate voltage was applied, common features were found

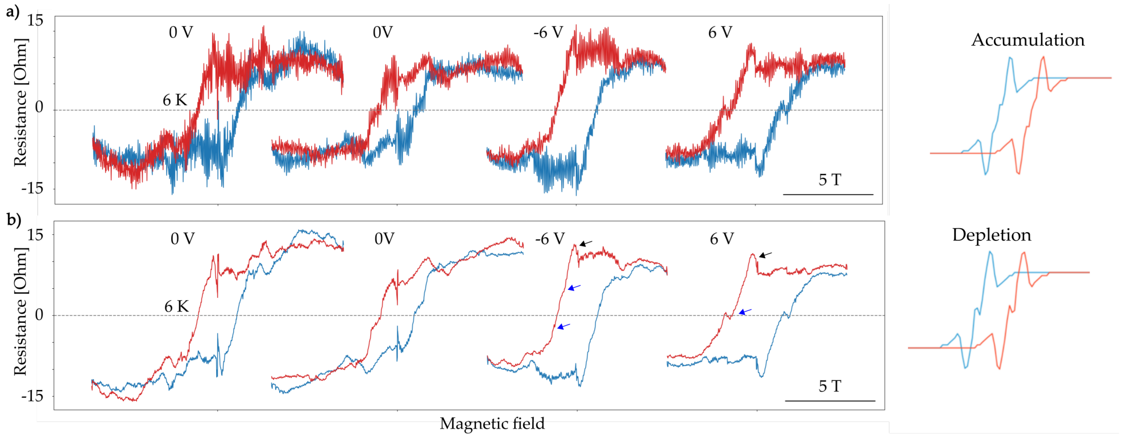

Figure 63: SRO32. Antisymmetrized anomalous Hall resistance as a function of top gate voltage at 7.5 K, save for one loop recorded at 6 K as indicated. a) Raw data and b) averaged data. Average is done over 8 adjacent points. For b), the high-field slope was corrected in an attempt to restore a hysteresis-loop shape. Numerical model predictions are included on the right.

for both values (black arrows) as the model expects, although two peaks were lost from the 5 K measurements, perhaps due to a change in magnetic state. The reappearance of two of the peaks in additional measurements steadies the hypothesis that they are reproducible. The nonzero top gate peaks are also sharper than those at 0 V, as could be expected from the model. Most remarkably, the low-magnetization behavior predicted by the model is apparent in the data (blue arrows): double switching for negative top gate, and a sign reversal for positive top gates. Since the sign switching appears for even low values of Fermi level shift, this should not serve as a measure for the degree of the shift alone, but should indicate that the Fermi level has been successfully shifted down by the top gate.

In order to verify if this behavior could be reproduced, another set of measurements was done at 7.5 K. As made evident by Fig.64, the data was not directly reproducible.

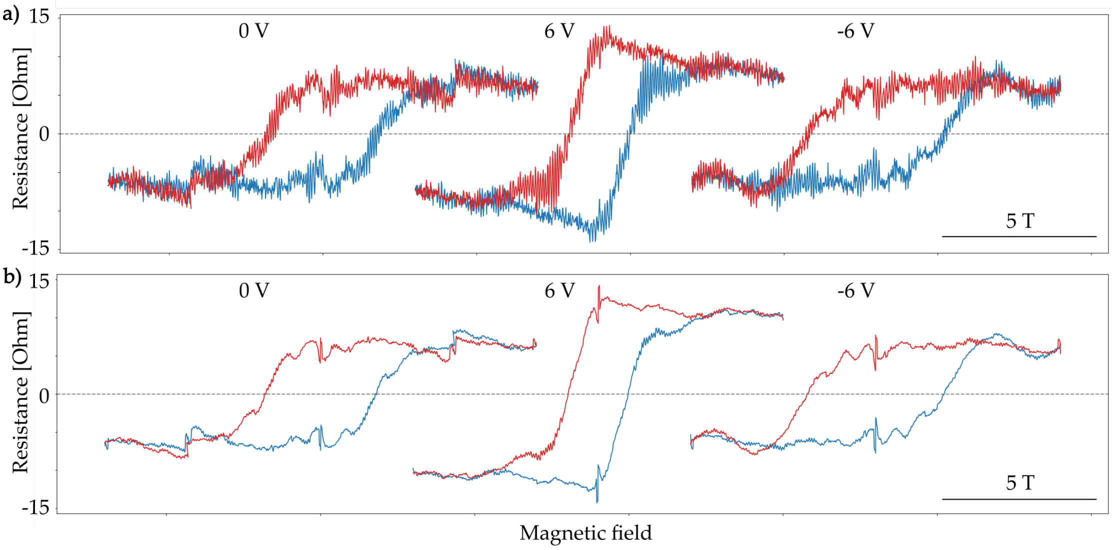

Figure 64: SRO32. Antisymmetrized anomalous Hall resistance as a function of top gate voltage at 7.5 K, second set of measurements. a) Raw data and b) averaged data. Average is done over 8 adjacent points. For b), the high-field slope was corrected in an attempt to restore a hysteresis-loop shape.

There are several reasons why this could be this case. Appendix 8.8 shows that the cooldown on 05-05, when the first 7.5 K data set was acquired, differs from the one on 06-05, where the second dataset was recorded. This could imply that the magnetic states, despite being at the same temperature, are different. Another possibility is the very nature of SRO32, as a semiconductor, makes it difficult to study repeatable transport properties due to trapped interfacial charges, especially at low temperatures.

While a simple one-loop model is sufficient in identifying main features in Fig.62 and Fig.63, perhaps a two-loop model would best capture the results in Fig.64, as there seem to be duplicate features in the 0 V and -6 V loops. A possible hypothesis could be two ferromagnetic layers, one at each interface. The $LaAlO_3$ -$SrRuO_3$ interface loop could be affected by the top gate, whereas the $SrTiO_3$ -$SrRuO_3$ loop would lie beyond the depletion length. This could be an explanation for the departure from the one-loop model fit. Possible fits are explored in Appendix 8.9.

Exculpating circumstances for not obtaining the same results also include temperature-drift noise (cf. Appendix 8.7), that is clearly visible for the 6 V measurement in Fig.64. The magnitude of the noise, and the fact that the magnetic state is very sensitive to temperature changes, makes the result inconclusive, and possibly not representative of a 6 V measurement at 7.5 K.

Another possibility is that the $SrRuO_3$ -$SrTiO_3$ interface is not affected in a reliable manner, or the ferromagnetic domain at the interface was different from previous measurements. Its capacity to affect the signal was estimated in Fig.55, and visible differences can be seen between the 0 V signal in Fig.63 and Fig.64, the former potentially suggesting a larger participation of the $SrRuO_3$ -$SrTiO_3$ interface based on the numerical simulation, specifically the suppression of one of the peaks and the 'wavy' loop body seen in Fig.55. It could be valid to consider that the magnetic domain at the $SrRuO_3$ -$SrTiO_3$ interface changes between measurement sets, affecting the total signal.

The 5 K results most closely resembled the numerical model, with the same general features appearing consistently over several measurements. Nevertheless, the quality of the non-averaged signal renders discussion debatable. The resemblance may have been coincidental, and until more low-temperature measurements are made in gated $SrRuO_3$ films, no definite conclusions can be drawn.

## 6.2 COOLDOWNS

Cooldowns measure anomalous and longitudinal conductivity in the samples as a function of temperature. A metal sees a decrease of resistance with a decrease in temperature, as thermal scattering will be reduced, whereas insulators and semiconductors see an increase of resistance with decreasing temperature, as fewer electrons are excited into the conduction band. At low temperatures, an increase in resistance is expected due to disorder-induced charge localization effects in $SrRuO_3$ thin films [37]. Close to the Curie temperature, a first-order ferromagnet to paramagnet phase transition takes place, appearing in the resistance vs. temperature data as a kink, or a point of discontinuous first derivative. The breadth of the ferromagnetic transition in $SrRuO_3$ was also shown to broaden with microstructural disorder[48]. These features should be noticeable in the cooldowns.

Field cooldowns are cooldowns with a magnetic field applied. Comparing two field cooldowns with opposite field applies reveals the effect of a magnetic field on the transverse signal in the sample. Information on the effect of the topgate can also be obtained in a similar fashion by applying opposing top gate values for sets of field cooldowns. Thus four separate cooldowns are sufficient to reveal these effects, should they exist. In order to compare the cooldown curves, the data needs to truncated in temperature between the lowest common high temperature and the highest common low temperature. In order to subtract the two curves, interpolation must be performed on the curves using the temperature data set containing the most points. The subtraction is still done between opposing values of magnetic field, for sets of cooldowns with matching top gate values.

### 6.2.1 *SRO13*

Fig.65 shows that SRO13 exhibits metallic behavior at high temperature, as the resistivity decreases with decreasing temperature. The Curie temperature manifests in the resistivity measurements as a kink at around 150 K, as exemplified in Fig.65) b).

In Fig.65 c), we note that positive top gate values tend to increased resistivity with respect to negative values. We also note that the positive top gate cooldown curves are noticeably more separated than the negative ones, as made clear by Fig.65 d); this could lead us to expect the positive top gate to have the largest effect on the sample. Comparing the resistivity values to Fig.65 a), we see that they are quite similar in magnitude to the 0 field, 0 V cooldown within the considered range.

The subtracted top gate curve shows the magnitude of the difference changing several times. At high temperatures until 185 K, the difference grows linearly with a large slope. Between 185 K and 155 K, the difference decreases and sees a sharp uptick at around 150 K, close to the measured Curie temperature. In Fig.65 c) we note that the kink associated with a ferromagnetic transition is difficult to see. The Curie temperature seems to be different between the different curves. One explanation for this could be the depletion and accumulation of charge carriers at the Fermi level by the top gate; since $SrRuO_3$ is an itinerant ferromagnet, changing occupation also changes the magnetic state. The peak in the subtracted positive top gate curve could be an indication of a ferromagnetic change, implying a difference of about 50 K in Curie temperature from positive to negative field with a positive top gate, corresponding to 4 meV of thermal energy shift. This behavior is not seen for the negative top gate pair, not for the 15 V cooldown, possibly meaning that this result is dubious. The kink in the negative top gate subtraction is due to a jump in the negative top gate and field term, due to the gas flow in the fridge increasing during the measurement close to 110 K, as is visible in Fig.65 c).

Since the positive top gate and field curve is the most different, it might be reasonable to question its accuracy. However, it is the data set with the highest number of data points (12163). The difference might be open to discussion, however, as the positive top gate and negative field data set consists of 7313 points. The number of points is directly correlated to the length of the measurement. It could indicate a measurement where the sample was cooled down too fast. Upon truncating the temperature

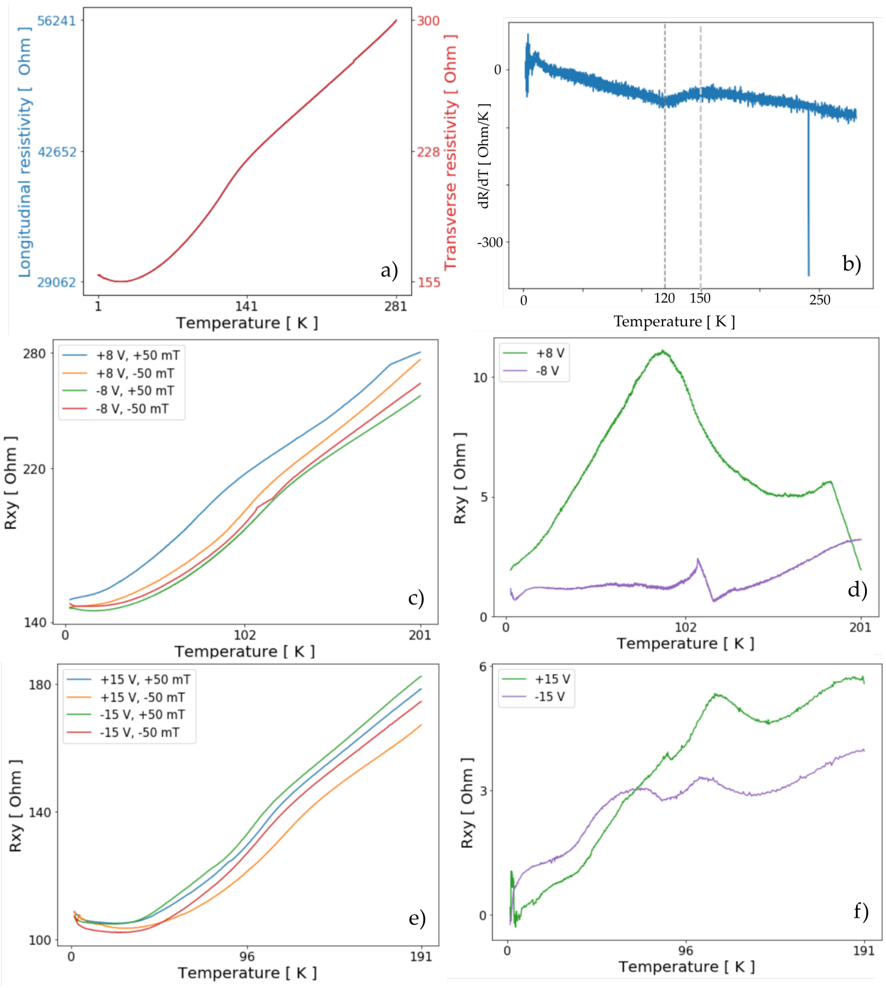

Figure 65: SRO13. a) Cooldown with no applied gate or magnetic field and its b) resistance gradient. c) Interpolated cooldown with a ±8 V top gate and ±50 mT field and d) the subtracted values between curves in c) sharing the same top gate and opposite field. e) Interpolated cooldown with a ±15 V top gate and ±50 mT field and f) the subtracted values between curves in e) sharing the same top gate and opposite field. In d) and f), subtraction is done so that the magnitude of the difference is positive.

and removing all repeated points in preparation for interpolation, however, the size of the dataset becomes 1814 and 1512 respectively. Therefore, the results need not be contested solely on the basis of an uneven set of measurements.

Of the positive top gate pair, the curve with a positive field is globally higher in resistivity than its negative field partner; this tendency is reversed in the negative top gate pair. This is no longer the case for the 15 V cooldown.

Comparing the 8 V and 15 V cooldowns, several observations can be made. First, the overall resistivity values are much lower for 15 V for the entire temperature range.

This implies that a larger top gate magnitude has increased the conductivity of the sample, regardless of its sign. Comparing this to the cooldown without an applied top gate voltage and field, both the initial resistivities and slopes are halved. The top gate thus has an increased effect at higher magnitudes, as expected, and this effect is non-negligible.

The curves are all more similar in shape, leading to similar subtraction curves. At temperatures above 96 K, both subtracted curves share the same features, being two peaks; one at around 185 K, and another at 115 K for the positive top gate and 105 K for the negative. Despite the second peak not being at the same temperature than the 8 V sweep, some similarity in general structure remain. Once again, it points to two changes in slope that could be associated with ferromagnetic transitions. A third peak at 70 K is noticeable for the negative subtracted curve, but beyond this, the trends between the two curves remain largely the same, but different enough to claim that the positive top gate voltage has a different effect on the sample than the negative top gate voltage.

In Fig.65 e), we see that a positive field yields higher resistivites. As opposed to the previous cooldown, the negative top gate set are no longer the less resistive pair, with the negative top gate and field being the most resistive of the four curves. This in itself should reveal the effect of increasing the magnitude of the top gate.

The negative field, negative top gate curve crosses the positive field, negative top gate curve, as in the 8 V cooldown. Here, however, the temperature at which this crossing occurs is increased from about 10 K to about 70 K, where we observe the third peak in the negative subtracted curve. The nature of this crossing is also changed, since here at high temperature it is the negative field, negative top gate curve that is higher in resistivity.

Overall, we see that despite the metallicity of SRO13, we expect to be able to influence the anomalous transport with the top gate, as Fig.65 d) and e) show that changing the top gate results in signal differences.

### 6.2.2 *SRO32*

SRO32 is semiconducting. Its semiconductivity should not be understood as a conventional semiconductor that has a small gap (less than 2 eV) [4], but rather as a bad metal with semiconducting transport characteristics. This has been noted previously in $SrRuO_3$ thin films [37]. Since SRO32 is semiconducting, we don't expect to see the same effect of the top gate during cooldowns as for SRO13. We might expect to see stronger effects, as the penetration depth should be longer. Even though this is a field cooldown without applying topgate voltage, it is still possible to glean useful information from it. First and most importantly, it reveals the semiconducting nature of the sample, from the increasing resistivity with decreasing temperature. During the cooldown, the sample resistance increased such that below 30 K, the signal sensitivity

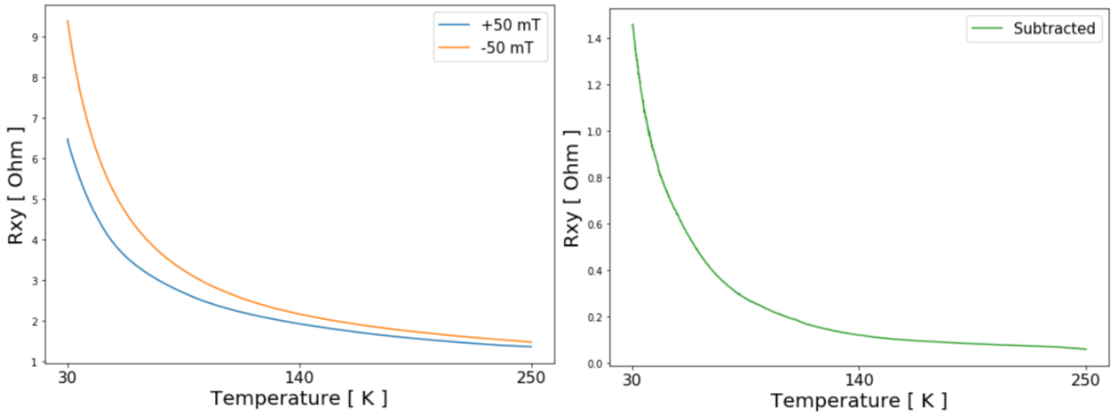

Figure 66: SRO32. Field cooldowns of field magnitude 50 mT a) before and b) after subtraction. Subtraction is done so that the magnitude of the difference is positive.

that was appropriate at high temperatures was too low. As such, the cooldowns are only shown until 30 K.

At first glance, no sign of a ferromagnetic phase switch is visible in the cooldowns. However, Fig.66 b) reveals a kink close to 40 K. Field sweeps at 65 K show that the ferromagnetic state no longer exists whereas it does at 30 K, thus not excluding the possibility of a transition close to 40 K. This is far below the Curie temperature of SRO13 (150 K). It is likely that the ferromagnetic state is more fragile to thermal perturbation in semiconducting $SrRuO_3$ ; its identity as an itinerant ferromagnet means that a decrease in conductivity is accompanied in a reduction in electrons contributing to the ferromagnetic state.

A similar decrease in Curie temperature in $SrRuO_3$ , from 163 to 45 K, was seen by Dabrowski et al. [38] as a result of fostering $Ru$ vacancies in pressed $SrRuO_3$ powders. As such, it is likely that SRO32 is $Ru$-deficient, possible close to the form $Sr_1Ru_{0.91}O_3$ [38].

In the following sections, magnetic field sweeps are performed in order to obtain information on the AHE. Since the AHE signal is directly related to the magnetization, magnetic field sweeps are an ideal tool for probing it. The magnetic field is varied between two extremes with the goal of obtaining a hysteresis loop. As seen in section 5.2.1.3, the anomalous conductivity still looks like a hysteresis loop, despite the additional peaks and switches.

## 6.3 SHEET RESISTANCE

The resistance of a thin film can be measured by sending a current through two probes, and measuring the voltage drop from one end of the sample to the other. Since the samples are close to two-dimensional, this resistance is known as the sheet resistance.

When the spacing between the probes is much smaller than the length and width of the film, the sheet resistance is given by $R_s = 4.532 * \frac{V}{I}$. A geometrical factor needs to be added if this is not the case [22]. For the Hall bars used, the geometrical factor is 0.5, yielding $R_s = 2.28 * \frac{V}{I}$ [19].

The sheet resistance as a function of top gate voltage is shown in Fig.67. From Fig.67 we see that the sheet resistance increases with negative top gate and decreases with positive top gate. Over 8 V, SRO13 experiences a sheet resistance change of about 10 Ω, whereas the difference is about 20 Ω in SRO32, showing that the semiconducting sample is affected more strongly by the top gate. For SRO13 both temperatures have similar slopes, whereas there is a marked difference for SRO32, further marking the larger sensitivity of the sample to both temperature and top gate. The top gate linearly alters the sheet resistance in SRO32. In SRO13, there seems to be two linear fits around -4 V at 1.5 K, or probably a more complex relation. The SRO32 30 K data was obtained for two different measurement runs. Their sheet resistances follow the same trend, but their values are offset by about 5 Ω , implying a difference magnetic state between the two measurement states. Nevertheless, the recorded data does not appear to fluctuate randomly with the top gate and the general trend has been shown to be repeatable. This can be taken as evidence that the top gate is affecting the sample and that trends are noticeable.

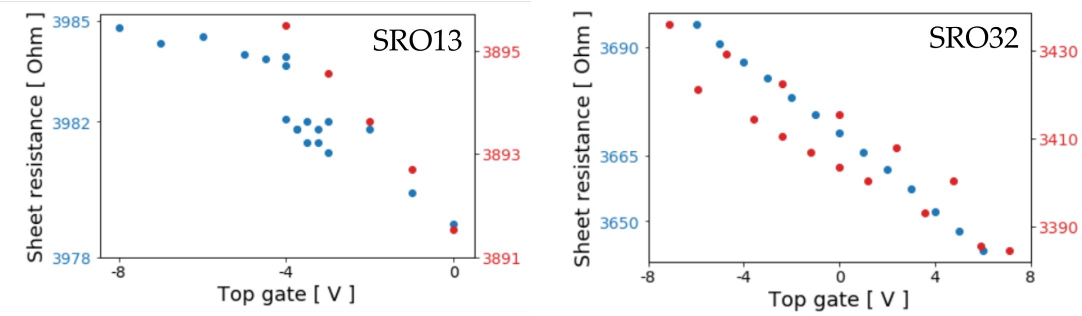

Figure 67: Sheet resistance of SRO13 and SRO32 as a function of top gate for different temperatures. For SRO13, measurements at 1.5 K are in blue, and at 10 K in red. For SRO32, measurements at 25 K are in blue, 30 K in red.

## 6.4 ORDINARY HALL EFFECT AND PENETRATION DEPTH

The OHE coefficient can be extracted from the high-field slope of the hysteresis slope, once the AHE signal has been saturated [45]. The Hall slope of SRO13, when considering only the 1.5 K data points in Fig.68, seem to follow a downward spike at around -3.75 V, with a width of about 2 V. Consecutive measurements around this area have a certain level of uncertainty, but the trend is retraceable, indicating that there is no (noticeable) gate hysteresis. This would indicate that trends are repeatable during the

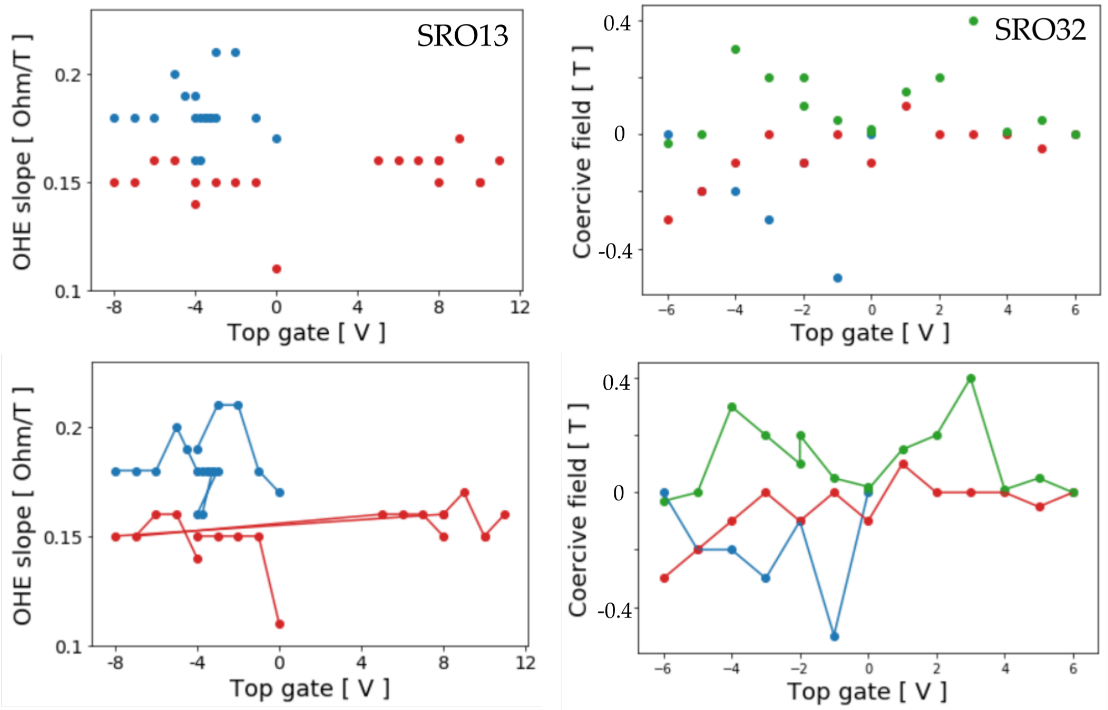

Figure 68: High-field slope data for SRO13 and SRO32. For SRO13, measurements at 1.5 K are in blue, and at 10 K in red. For SRO32, measurements at 15 K are in blue, 25 K are in red, and 30 K in green. Line plots connect consecutive measurements and are intended to help guide the eye.

same measurement set. The 10 K data also shows that measuring 5 V, -8 V then 8 V consecutively yields only a significant alteration of the signal. It's not possible to gauge whether this is due to fluctuations in the measurements or if it is linked to gate hysteresis.

There is little certainty that a general trend can be established, and even if it could, it has a nontrivial shape. For SRO13 it is apparent that the slope at 10 K has a general tendency to be lower than at 1.5 K. The slope remains virtually constant at 10 K, meaning that we cannot verify whether the changes in OHE slope at 1.5 K are due to the top gate and are washed out by competing energy scales at high temperature, or whether the changes are due to low-temperature, disorder-induced processes.

The SRO32 data features larger changes in high-field slope over a broader range, including the transition into negative slope. The data was more difficult to extract precisely in SRO32, as high field effects often perturbed the measurement of the slope. As such, the presented data serves to show that the variation with top gate is generally larger than the variation with temperature. This could serve to mark the top gate as the more important energy scale in SRO32. The SRO32 data remains inconclusive, however, due to the complex trends.

Due to some values being 0, the electron density will not be defined for SRO32. For SRO13, the calculated electron density ranges between 3 and 4 $*10^{19}$ for 1.5 K and from 3.5 to 6 $*10^{19}$ at 10 K (cf. Appendix 8.4). This indicates that localized charges that were frozen at 1.5 K have been activated at 10 K. The penetration depth is directly calculated from the carrier density using Ref.[26], and is lower at 10 K than at 1.5 K, most likely due to the additional screening charges. The penetration depth as calculated average 5 to 6 Å, corresponds to a unit cell, implying it is not immediately screened at the surface. This is a good sign not only for this experiment, but also for future $SrRuO_3$ top-gating experiments. However, the dependence in gate voltage shows no accumulation or depletion trends. This could mean that the considered voltages are not large enough to cause the desired effect.

## 6.5 LOOP HEIGHT

The loop height data has several caveats. At 1.5 K in SRO13, trapped charges led to signal surges and random noise that affected the height of the loop in patches. Some patches are inevitably found at 0 T, where the loop height is measured, causing noise to appear in the measurements. Averaging the data over neighboring points was done to reduce this. Unlike the high-field slope data, the loop heights in SRO13 revealed a trend, visible in Fig.69. Fig.69 compares the two negative top gate signals. At 1.5 K, the loop height seems to generally decrease with increasing negative top gate, which is one of the expected effects of the top gate; at the very least, the loop height does not increase above the 0 V value. This is however not the case for the data at 10 K.

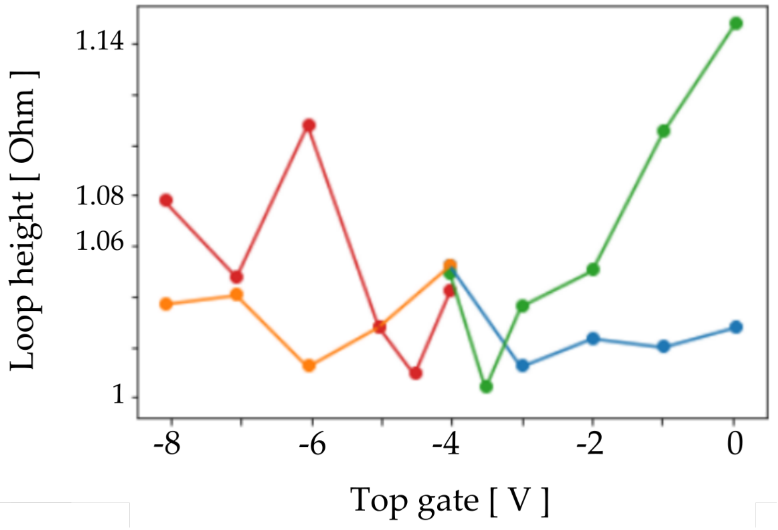

Figure 69: SRO13. Loop height as a function of top gate and temperature. In red and green are the 1.5 K datasets, in blue and yellow the 10 K datasets.

Comparing the 10 K results to the 1.5 K results, we note that the 10 K set is contained within a smaller range and the change between top gate values is smaller. This could mean that the penetration depth has been reduced by the increase in temperature, or also that there are no more signal surges from trapped charges. The global trends are quite comparable: a decrease in loop height attaining a sharp peak, followed by a dip, another peak, and a second dropoff. The most striking similarity between the datasets is close to identical value of the loop height at -4 V between all four sets. What is also interesting is that the 10 K signal has broader peaks and dips. The degree of broadening could give an indication as to the competition between the top gate and the temperature. In any case, the loop height results from 1.5 K can be considered repeatable at higher temperatures. The deviation of points recorded at the same top gate value is less than 0.1 Ω, or 10% of the signal magnitude.

The loop shapes in section 6.1 occasionally have an additional tail before closing, implying that the same field takes longer to saturate the magnetization. In turn, this change in magnetic state can affect the loop height; discontinuities at 0 T can be seen as a result in the majority of sweeps. Future experiments could sweep to larger field magnitudes and check whether the same trend can be seen. Due to even more pronounced high-field disturbances affecting the magnetic state at 0 T, loop height measurements for SRO32 proved inconclusive and are not worth considering quantitatively.

One could wonder what happens at stronger voltages. The top gate voltage was pushed to 15 V for the field cooldowns, then some sweeps were done at 10 V and higher. However, at these voltages the signal became highly perturbed (see Appendix 8.6), presumably from the dielectric layer being damaged by discharge or spikes in supplied voltage.

## 6.6 RECONCILING THE TIGHT-BINDING MODEL AND THE DOUBLE-LOOP MODEL

The experimental results seem to indicate that the numerical model is only comparable to experimental data in semiconducting $SrRuO_3$ at low temperature. At higher temperatures, features from the numerical models are washed out in favor of a more conventional hysteresis or double hysteresis shape, where the dominating contribution to the AHE signal comes from the magnetization of the sample. It could be possible that the numerical model shows the low energy limit of the single-loop and double-loop picture. In this case, the change in signal could be attributed to a strengthening of the low-temperature signal rather than a change in the double-loop domains of the sample. In order to determine whether the contribution from the low energy signal or the changing of the magnetic domains with lowering temperature is the most important, magnetic imaging experiments could be done, in parallel to further conventional transport experiments testing the low-temperature signal and its evolution with temperature.

## 6.7 PARTIAL MAGNETIC FIELD SWEEPS

The intriguing shape of the AHE signal in multi-oxide devices could be attributed to inter-oxide interface effects. However, similar non-conventional shapes have also been observed in $SrRuO_3$ films with no capping layer [75]. The effect appears to be even larger in released $SrRuO_3$ flakes stamped onto an $SrTiO_3$ substrate as in Ref.[21], and are recorded below. Relaxed $SrRuO_3$ thin films have proven to have complex loops; this same sample was used in Ref. [21], where it displays a remarkable double-loop behavior. The loops at low temperature differ from our measurements, so it is possible the device was affected or otherwise degraded since the redaction of Ref.[21]. Differences in signal also arise from the fact that 7 T do not appear to suffice to close the loop, and discontinuities arise at 0 T.

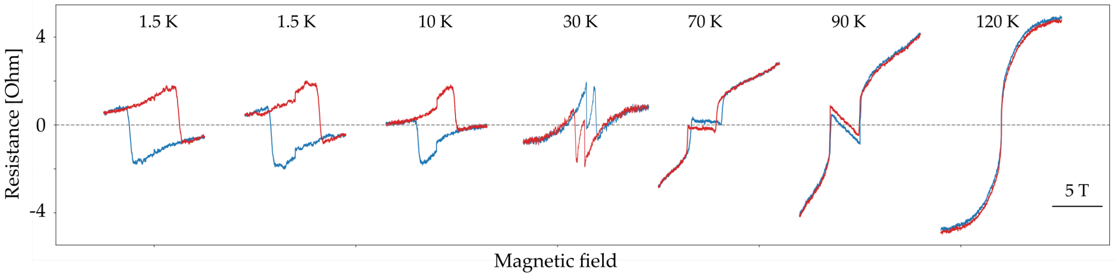

Figure 70: FM15b. Antisymmetrized anomalous Hall resistance as a function of temperature.

An important experiment in determining the magnetic states in $SrRuO_3$ is the partial sweep. It operates on the same principle as the magnetic field sweeps, but seek to under-saturate the magnetization in order to determine whether two ferromagnetic domains of opposite sign are present in the sample, as illustrated in Appendix 8.11.

Partial sweeps were performed on FM15b at 30 K. After each partial sweep from 0 T, the sweep breadth and back to 0 T, the sample is prepared for the next measurement by sweeping the field down to the maximum opposite field value and back. However, as Fig.70 shows, at 30 K, 7 T does not close the loop. Therefore, the partial sweeps were affected by this discontinuity, and the incorrect state was prepared at 0 T. From Fig.71 we see that the peak feature visible for the 1.4 T sweep disappear before the signal flattens as indicated in Appendix 8.11. This would not suggest the presence of two opposite AHE contributions, but the preparation of the magnetic state was not correct and as such no conclusions can be made.

Partial sweep experiments should be done parallel to full magnetic sweeps as a complement to understanding the final AHE signal. For example, it would have helped determine whether two loops of opposite sign were creating the complex low-temperature signal of SRO32, and how that changed between different measurements, as a sign of the fragility of magnetic states in semiconducting $SrRuO_3$ . As long as care is taken to

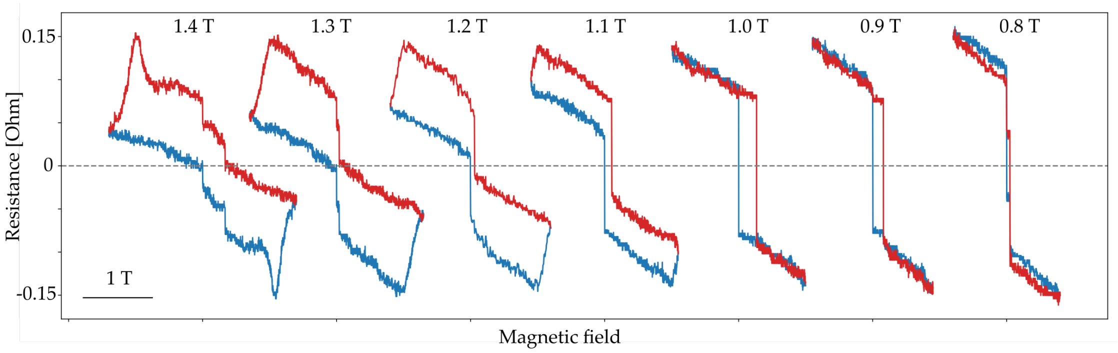

Figure 71: FM15b. Antisymmetrized anomalous Hall resistance from partial sweeps as a function of maximum field at 30 K.

ensure the correct preparation of the initial magnetic state, they can be a powerful tool to exploring the transport properties of metallic ferromagnets.

# Part IV

# APPENDIX

# 7

# APPENDIX A

## 7.1 APPENDIX A.1

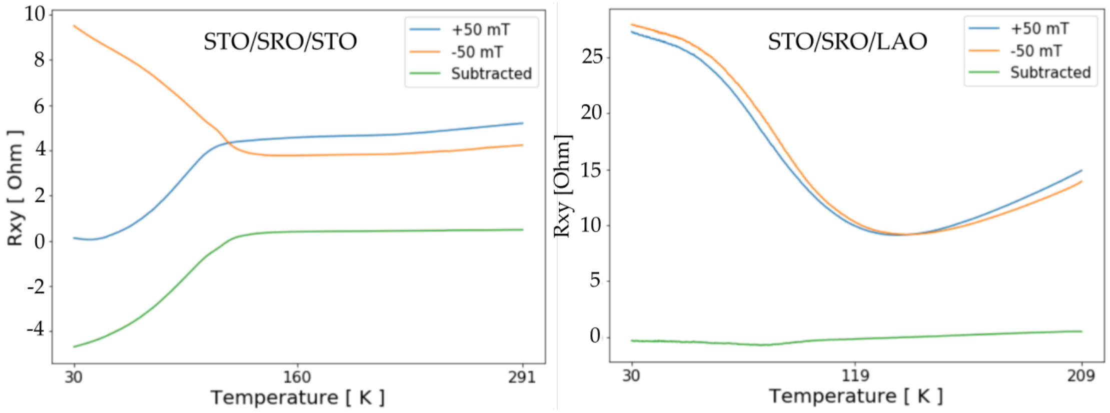

Figure 72: Field cooldowns for a STO/SRO(5 u.c.)/STO(10 u.c.) sample and a STO/SRO(4 u.c.)/LAO(10 u.c.) sample. The $LaAlO_3$ -capped sample shows higher resistance, possibly indicating a depleted layer in the $SrRuO_3$ . This makes $SrTiO_3$ -$SrRuO_3$ -$LaAlO_3$ samples more suited to top gate experiments. (We also note that the STO/SRO/LAO sample has 4 u.c. of $SrRuO_3$ , so perhaps the increase in resistance is dimensionally-driven.)

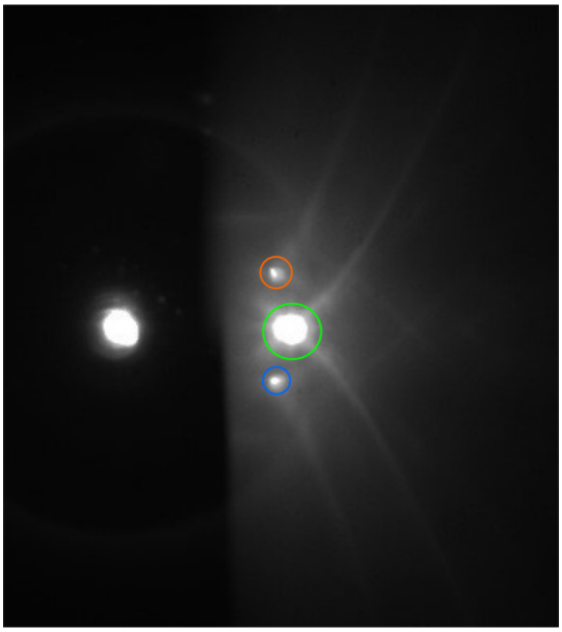

Figure 73: RHEED diffraction pattern. The spots are color coded according to their contribution in Fig.25

## 7.3 APPENDIX A.3

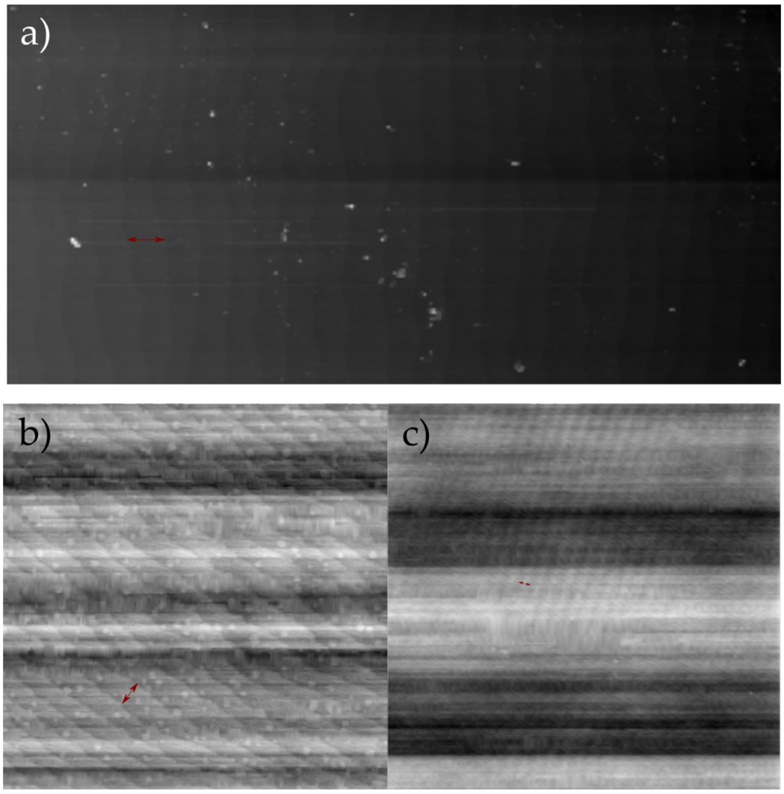

Figure 74: Atomic force microscopy (AFM) images of SRO34, a sample grown in the same conditions as SRO32. a) the $SrTiO_3$ substrate as received, b) a 5-by-5 and c) a 25-by-25 micron scan of the film surface. Red arrows indicate terrace width, showing the preservation of the step edges and the quality of the epitaxial growth.

## 7.4 APPENDIX A.4

Code used to obtain eigenvalues and eigenstates.
`https://github.com/helenespring/appendices`

## 7.5 APPENDIX A.5

Code used to determine a 2D map of coordinate points in k-space.
`https://github.com/helenespring/appendices`

## 7.6 APPENDIX A.6

Code used to obtain the Berry curvature and 2D plane contribution to the conductivity from the eigenvalues and eigenstates. It expects the externally generated coordinates and eigenvalue, eigenstate set using the previous two functions. `https://github.com/helenespring/appendices`

# 8

# APPENDIX B

## 8.1 APPENDIX B.1

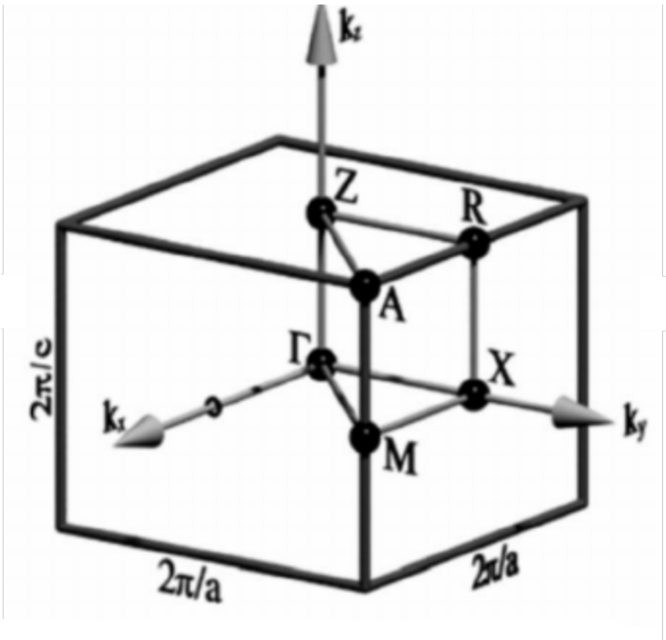

Figure 75: First Brillouin zone of a tetragonal lattice with high-symmetry points, from Ref.[44]. Since we consider a 2D model (x-y plane), $\Gamma,\ X,\ M$ are the only high-symmetry points considered.

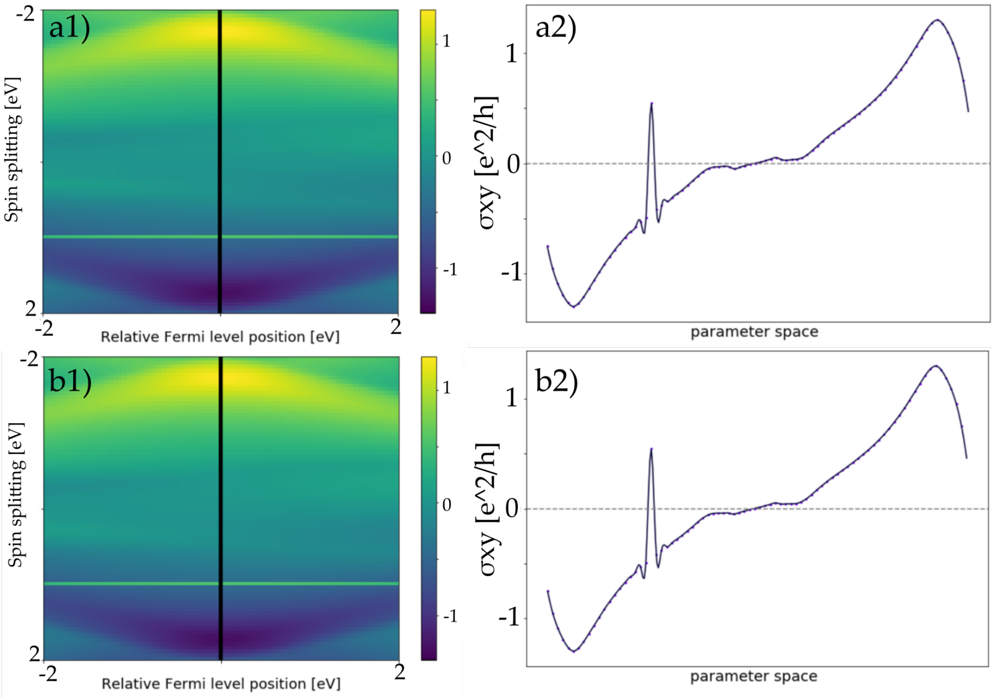

Figure 76: AHE signal as a function of exchange splitting for fixed values of the chemical potential. Black lines on a1), b1) indicate path taken in parameter space, and a2), b2) show the AHE signal strength along the paths. k-space partitioning is a) $350 * 350$ and b) $500 * 500$.

At an exchange splitting value of -1, the signal suddenly changes sign for a single data point, so over a range of 50 meV. This anomaly is also present for all considered values of relative Fermi level position, from -2 to 2 eV. Values of the AHE signal around this point are listed in Table 2 at 0 eV relative Fermi level position: The contribution

Table 2: AHE anomaly as a function of exchange splitting and k-space partition

| **Exchange splitting [eV]** | **300*300** | **350*350** | **400*400** | **450*450** | **500*500** |
|---|---|---|---|---|---|
| -1.1 | -0.533 | -0.532 | -0.532 | -0.533 | -0.533 |
| -1.05 | -0.491 | -0.491 | -0.492 | -0.492 | -0.493 |
| -1 | -0.453 | +0.546 | +0.546 | +0.545 | +0.545 |
| -0.95 | -0.416 | -0.417 | -0.416 | -0.417 | -0.417 |
| -0.9 | -0.380 | -0.380 | -0.381 | -0.382 | -0.382 |

must arise from parts of the band structure either below -2 eV or above 2 eV, or both. As it turns out, looking at the band structure for -1.05, -1, and -0.96 eV of exchange splitting yield the origin of this signal: From Fig.77 we see that bands become degenerate at Γ and at $M$. This degeneracy is symmetrically lifted around -1 eV exchange splitting. At this crossing, massive contributions arise for the single-square Γ and $M$ positions, $10^4$ times larger than contributions per square on average in surrounding bands. These degeneracies are between SOC-coupled bands; in essence, the two anti-crossings roll into one point. As mentioned previously in passing, this should result in the presence of a Dirac cone. However, since it's far below the Fermi level, this should not result in a change of signal. At the degeneracy point, the signal jumps by $1.037e^2/h$ or $1.038e^2/h$. The signal then jumps by $-0.963e^2/h$ or $-0.962e^2/h$. The linear regression between the surrounding points to has a slope of 0.755, leading to a difference of about $0.04e^2/h$. Taking this into account, the jump in signal is a quantized jump of $1\ e^2/h$.

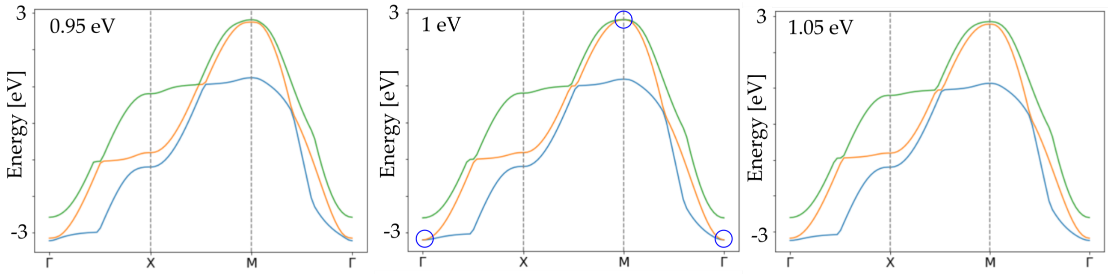

Figure 77: Scipy bands 1, 2 and 3. Blue circles indicate degenerate crossings.

This means there is a problem with the numerical calculation. It is most likely due to the two Weyl nodes meeting on corners of a single integration square yielding a quantized signal. The same thing happens at the $M$ point, but since it is above the Fermi level its signal is not registered by the conductivity calculation.

As such, the $300 * 300$ partition, which washes out this signal, will be most qualitatively relevant to the experiments.

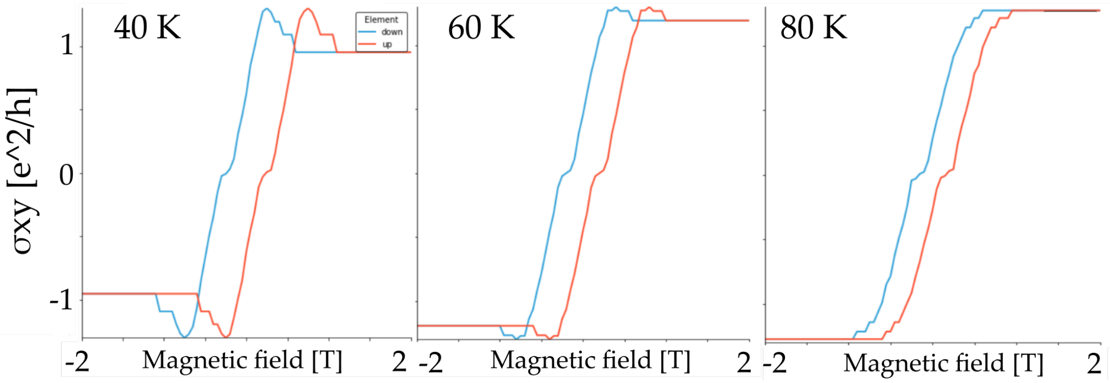

Figure 78: Change of AHE signal with temperature of the $SrRuO_3$ monolayer model.

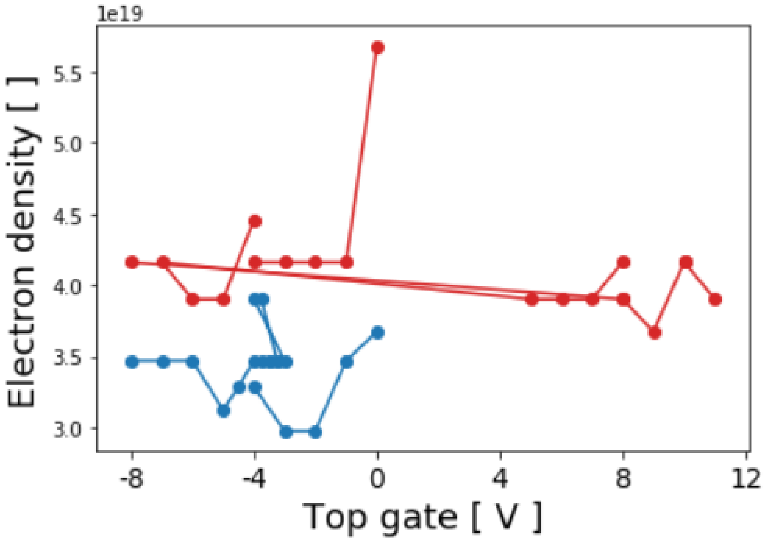

Figure 79: SRO13. Electron density at 1.5 K (blue) and 10 K (red) as a function of top gate voltage.

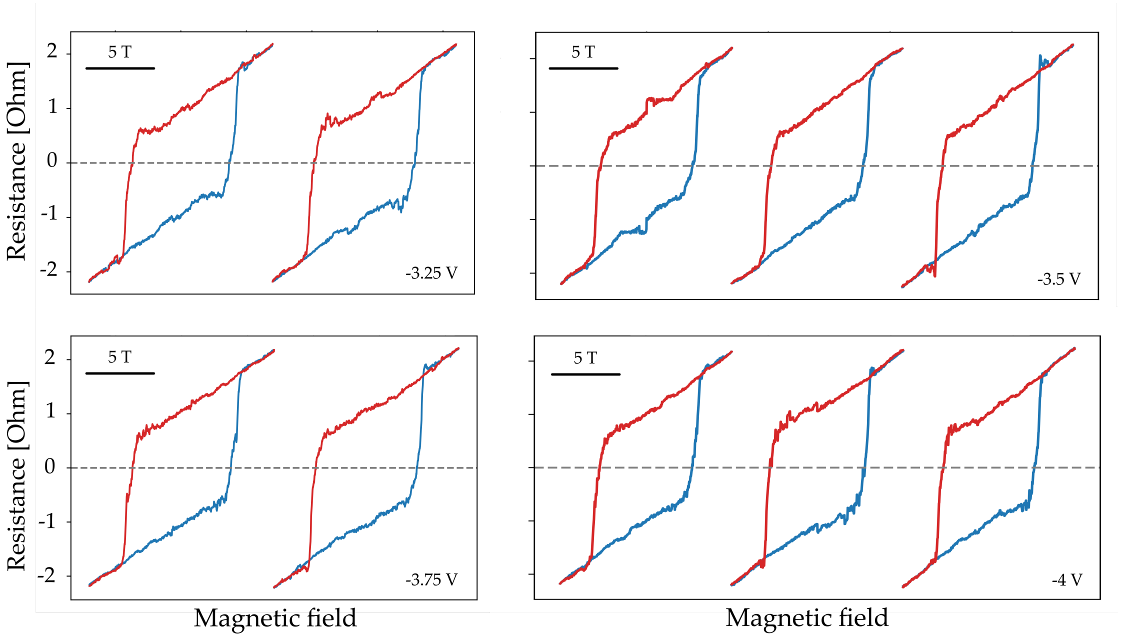

Figure 80: SRO13. Magnetic field sweeps at 1.5 K. With repeated measurements, the same loops are not obtained, and spurious features appear.

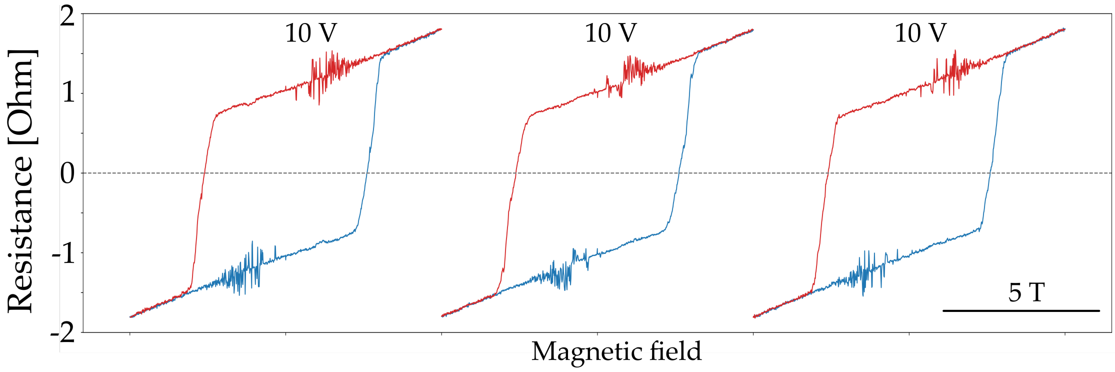

Figure 81: SRO13. Antisymmetrized AHE conductivity at 10 K.

## 8.7 APPENDIX B.7

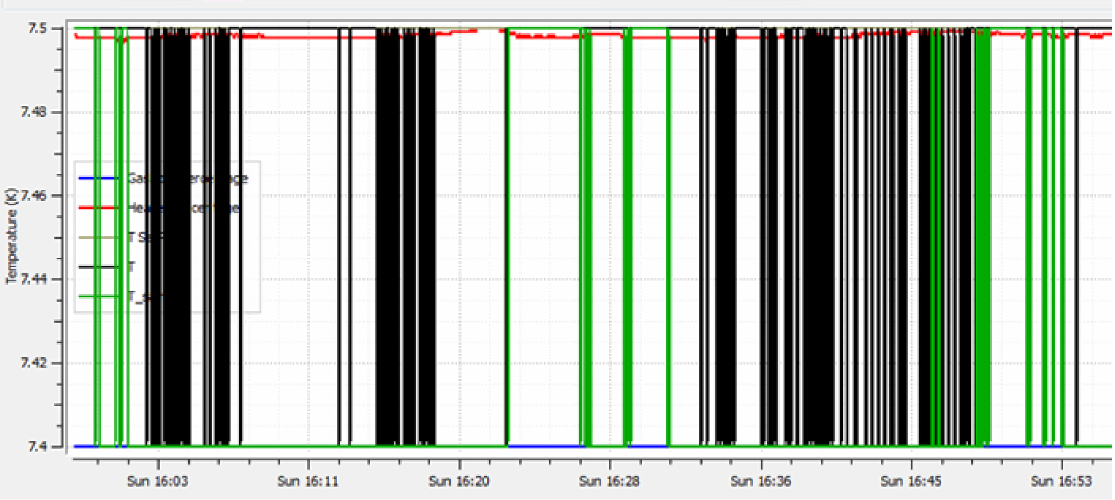

Figure 82: SRO32. Temperature drift as a function of time during a measurement at 7.5 K. The results are increasingly sensitive to changes in temperature at low temperatures, and as such this is a significant source of noise at low temperatures.

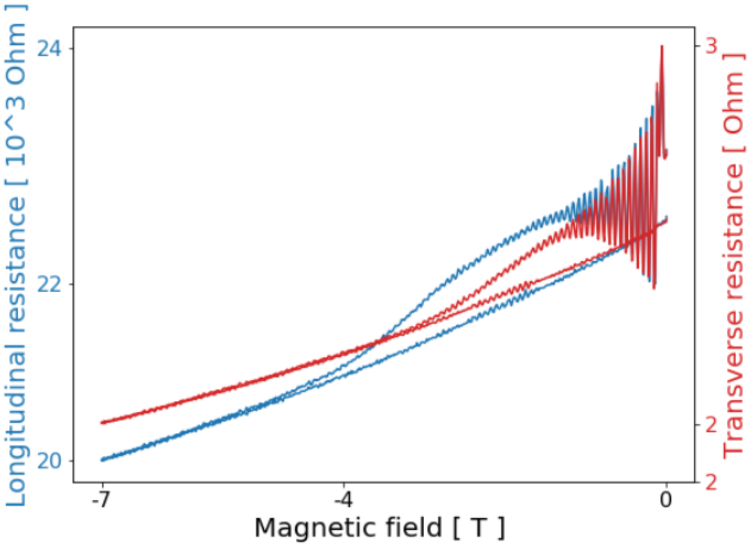

Figure 83: SRO32. Presweep at 5 K shows signal fluctuations due to temperature drift.

## 8.8 APPENDIX B.8

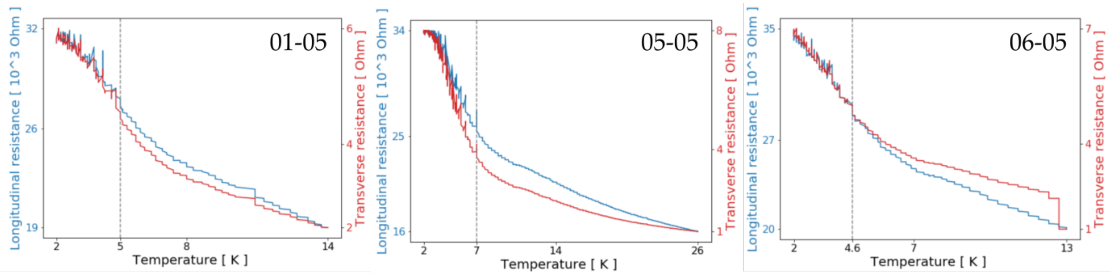

Figure 84: SRO32. Cooldowns on different days show a changing boundary for the limit of the measurement module sensitivity.

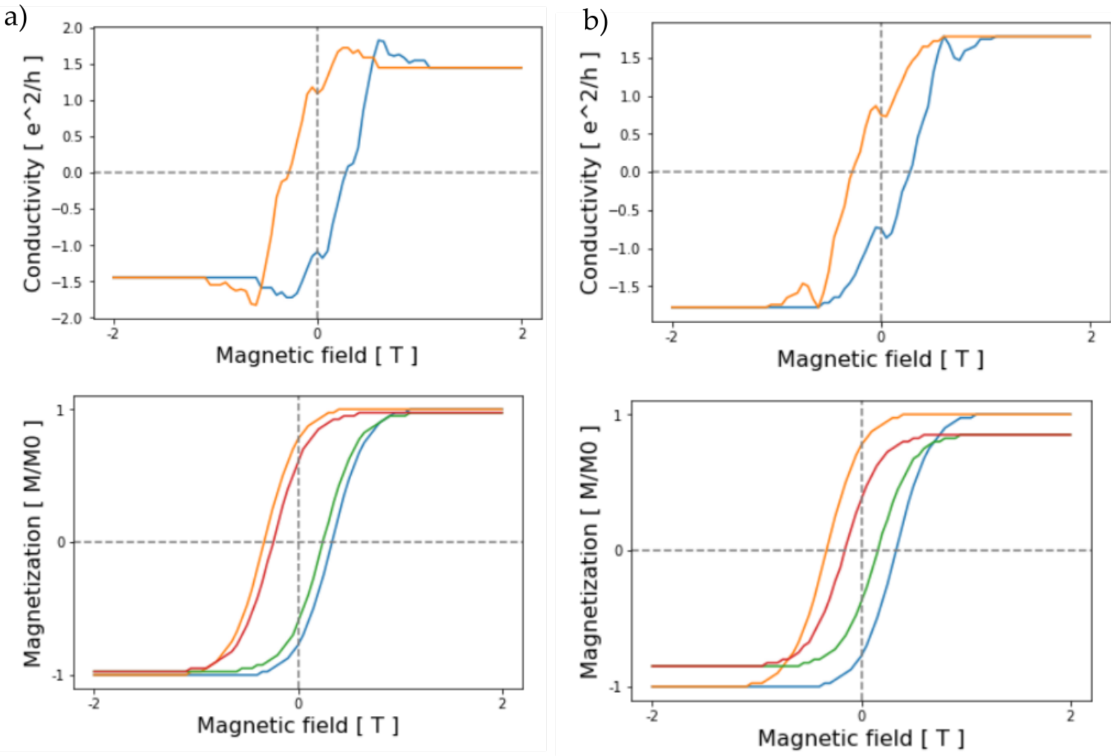

Figure 85: Two-loop signal for the $SrRuO_3$ model. a) the loop with smaller coercivity has a negative Fermi shift and b) positive Fermi shift. Since the parameter space is large (initial magnetization, coercivity, chemical potential), a large number of combinations exist.

## 8.10 APPENDIX B.10

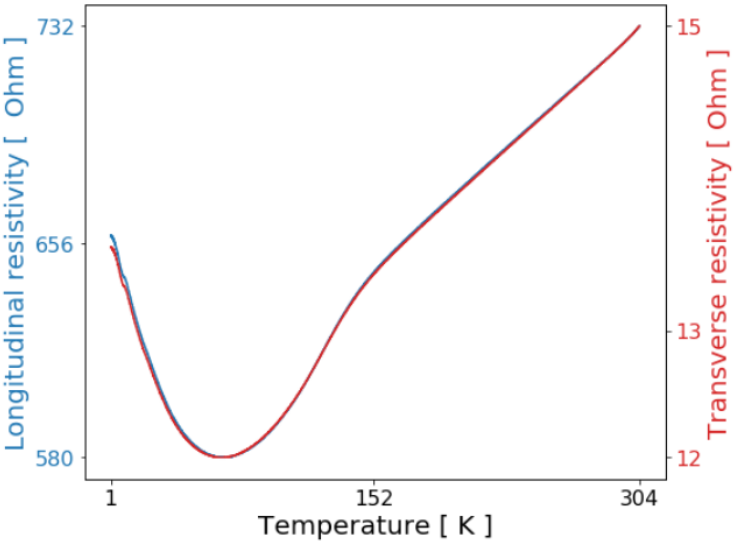

Figure 86: FM15b. Cooldown at 0 T.

## 8.11 APPENDIX B.11

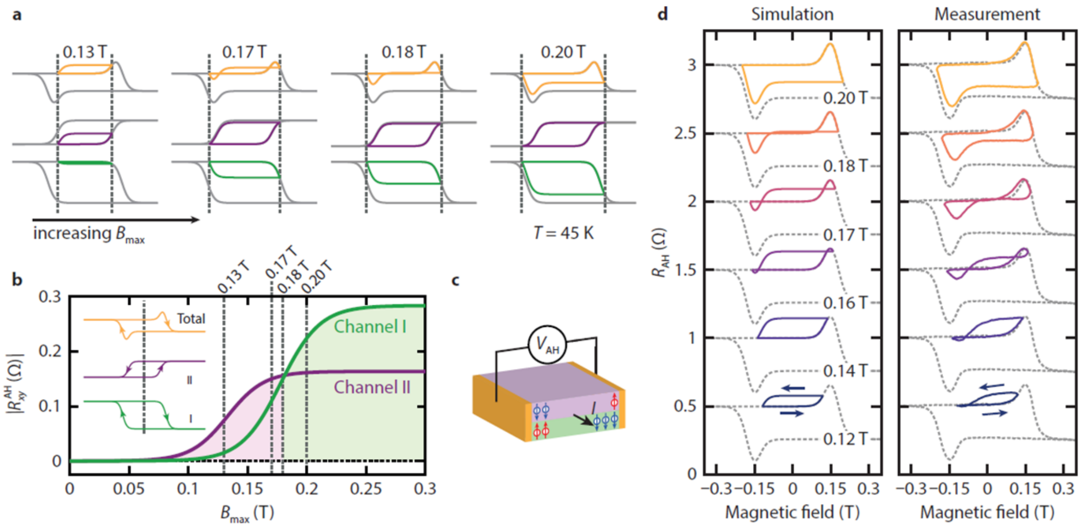

Figure 87: Taken from Ref.[45]. a) Simulations of the AHE signal for different sweep ranges. b) Magnitudes of the AHE signal for the two different channels. c) A schematic of spin accumulation on different interfaces of $SrRuO_3$ . d) Comparison of simulated and measured data for partial sweeps; curves are offset vertically.

Ref.[45] supports the double-AHE countribution argument for the conductivity peaks seen in $SrTiO_3$ -$SrRuO_3$ -$SrIrO_3$ devices by providing experimental data showing a discontinuity in coercivity when the AHE signal switches sign. This is attributable to the presence of two magnetic domains of opposite sign. Studying the coercivity of $SrTiO_3$ -$SrRuO_3$ -$LaAlO_3$ films could also give indications on the underlying magnetic domain state of the sample. Coercive fields of the SRO32 loops were measured at 30 K and 25 K. In Fig.88 a), the two separate data set seem disparate, but they share the same value at 0 V and -2 V, the two repeated measurements, and the -6 V value lies close to the -5 V value. However, the giant peak at -4 V and the zig-zag shape of the coercive field at high temperatures implies that there are differences in the magnetic state of the two data sets. Nevertheless, the yellow data set seems to follow the trend of the zig-zag at 6 V. Fig.88 a) shows the 0 V and -2 V measurements were repeatable, implying a non-random effect of the top gate on the sample. This takeaway is justifiable in that

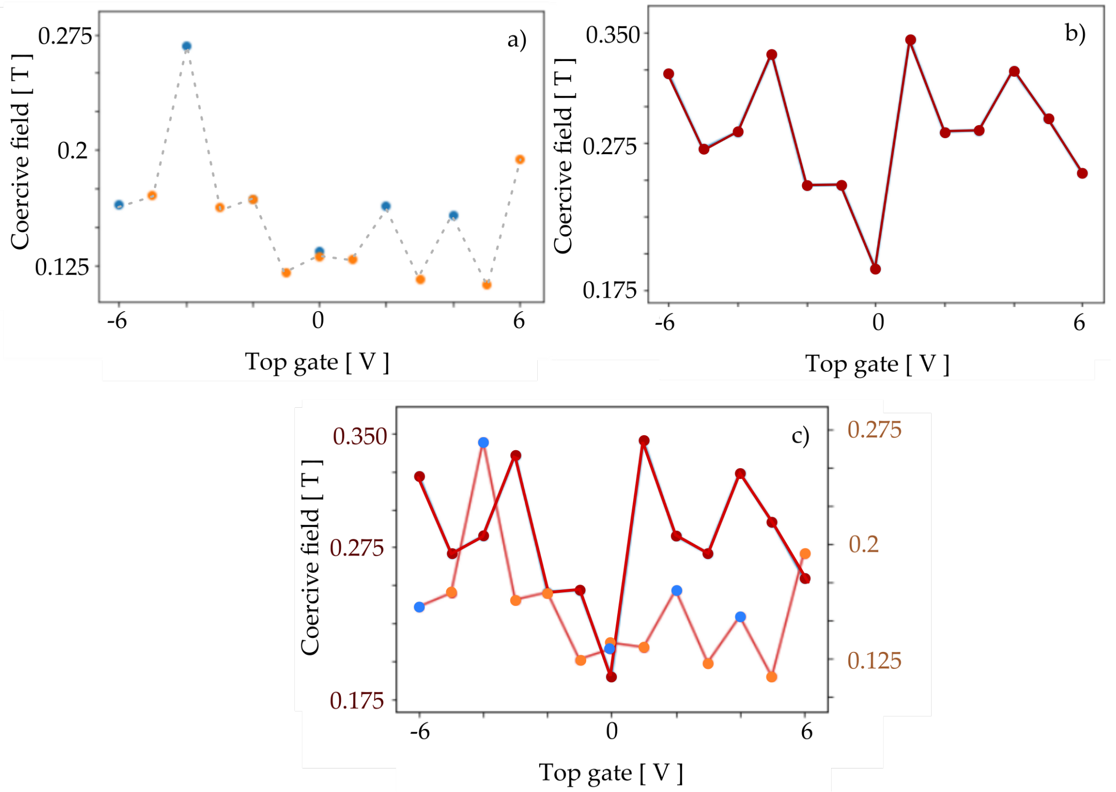

Figure 88: SRO32. Coercive field as a function of top gate voltage. a) The colors index two separate measurement sets at 30 K. The dashed line connects all adjacent values of coercivity. b) One data set at 25 K performed in one stretch from -6 V to 6 V. c) Comparison of the trends at 30 K and 25 K. The data is OHE-slope corrected.

the magnetic state was destroyed then restored between the two measurement sets, and that the second data set measured the 6 V loop before measuring the 0 and -2 V loops.

The measurements at 30 K are not sufficient to say whether the two data sets should be connected in a zig-zag pattern, or whether they should be considered separately. In order to determine this, a continuous measurement at 25 K was performed, from -6 V to 6 V, as pictured in Fig.88, and compared to the 30 K measurements in Fig.88. We see that the peaks are shifted to higher voltage magnitudes at higher temperature. While it may not be wise to analyze the shift quantitatively, a qualitative similarity remains, particularly at negative top gate voltages, implying that the coercive field signals are not behaving randomly under changing top gate voltage. Trends seem reproducible within the same sample. However, a larger data set must be acquired in order to verify this, with smaller steps in voltage, and no definite trends or conclusions can be drawn from the current dataset.

# Part V

# BIBLIOGRAPHY

[1] In: *http://www.ltlab.com/optcryo105.html* ().

[2] In: *https://www.python-course.eu/graphs_python.php* ().

[3] Kundu A.K. *Magnetic Perovskites*. Springer, 2016. Chap. Introduction to Magnetic Perovskites, pp. 1–35.

[4] N.W. Ashcroft and N.D. Mermin. *Solid State Physics*. Philadelphia: Saunders College, 1976.

[5] Chang C.-Z. and Li M. "Quantum anomalous Hall effect in time-reversal-symmetry breaking topological insulators". In: *Journal of Physics: Condensed Matter* 28.123002 (2016).

[6] Schneider C.W. and Lippert T. *Laser processing of materials*. Springer, 2010. Chap. Laser ablation and thin film deposition, pp. 89–112.

[7] Groenendijk D. "Spin–orbit coupling and geometric phases at oxide interfaces". 2019.

[8] Hall E.H. "On a new action of the magnet on electric currents". In: *American Journal of Mathematics* 2 (1879), pp. 287–292.

[9] Haldane F.D.M. "Berry Curvature on the Fermi Surface: Anomalous Hall Effect as a Topological Fermi-Liquid Property". In: *Physical Review Letters* 93.206602 (2004).

[10] Xiaodong Fang and Takeshi Kobayashi. "Characterization of thin film grown by laser ablation at temperatures above 400 C". In: *Journal of Applied Physics* 90.162 (2001).

[11] Samara G.A. "Low-temperature dielectric properties of candidate substrates for high-temperature superconductors: LaAlO3 and ZrO2 9.5 mol Y2O3". In: *Journal of Applied Physics* 68.4214 (1990).

[12] Weaver H.E. "Dielectric properties of single crystals of SrTiO3 at low temperatures". In: *Journal of Physics and Chemistry of Solids* 11.3 (1959), pp. 274 –277.

[13] Hwang H.Y. "Emergent phenomena at oxide interfaces". In: *Nature Materials* 11 (2012), pp. 103–113.

[14] Preskill J. "Magnetic Monopoles". In: *Annual Review of Nuclear and Particle Science* 34 (1984), pp. 461–530.

[15] Robertson J. "High dielectric constant oxides". In: *Eur. Phys. J. Appl. Phys.* 28.3 (2004), pp. 265–291.

[16] Chen L.-Y. “Dielectric performance of a high purity HTCC alumina at high temperatures - a comparison study with other polycrystalline alumina”. In: *Additional Conferences (Device Packaging, HiTEC, HiTEN, and CICMT)* 2014 (2014), pp. 271–277.

[17] Klein L. “Comment on ”Exchange bias-like phenomenon in SrRuO3” [Appl. Phys. Lett. 88, 102502 (2006)]”. In: *Applied Physics Letters* 89.036101 (2006).

[18] Stamokostas G. L. and Fiete G. A. “Mixing of t2g-eg orbitals in 4d and 5d transition metal oxides”. In: *Physical Review B.* 97.085150 (2018).

[19] Valdes L.B. “Resistivity measurements on Germanium for transistors”. In: *Proc. I.R.E.* 42 (1954), pp. 420–427.

[20] Kim M. and Min B.I. “Nature of itinerant ferromagnetism of SrRuO3: a DFT+DMFT study”. In: *Physical Review B* 91.205116 (2015).

[21] Monteiro M. “Quantum transport at oxide interfaces”. TU Delft, 2019.

[22] Heaney M.B. *Electrical Measurement, Signal Processing and Displays*. Ed. by CRC Press. 2003. Chap. Electrical Conductivity and Resistivity.

[23] Chang M.C. “Berry Phase in Solid State Physics”. In: ().

[24] Berry M.V. “Quantal phase factors accompanying adiabatic changes”. In: *Proc. R. Soc. Lond.* 392 (1984).

[25] Singh N. “The story of magnetism: from Heisenberg, Slater and Stoner to van Vleck, and the issues of exchange and correlation”. In: *arXiv preprint 1807.11291* (2018).

[26] Gariglio S. “Transport properties of $LaTiO_{3+\delta}$ and $REBa_2Cu_3O_{7-\delta}$ thin films: a study of correlation effects”. 2003.

[27] Ishihara T. *Perovskite Oxide for Solid Oxide Fuel Cells*. Springer, 2009. Chap. Structure and Properties of Perovskite Oxides, pp. 1–16.

[28] Kuech T. *Handbook of Crystal Growth: Thin Films and Epitaxy*. Elsevier, 2014.

[29] Moriya T. and Takahashi Y. “Spin fluctuations in itinerant electron magnetism”. In: *Journal de Physique Colloques* 39.C6 (1978), pp. 1466–1471.

[30] Zwerger W. “Itinerant Ferromagnetism with Cold Atoms”. In: *Science* 325.1179767 (2009).

[31] Allen P.B. et al. “Transport properties, thermodynamic properties, and electronic structure of SrRuO3”. In: *Physical Review B* 53.8 (1996).

[32] Asbóth J.K. et al. *A Short Course on Topological Insulators: Band Structure and Edge States in One and Two Dimensions*. Springer, 2016.

[33] Aso R. et al. “Atomic level observation of octahedral distortions at the perovskite oxide heterointerface”. In: *Scientific Reports* 3.2214 (2013).

[34] Boschker H. et al. "Ferromagnetism and Conductivity in Atomically Thin SrRuO3". In: *Phys. Rev. X.* 9.011027 (2019).

[35] Broas M. et al. "Chemically stable atomic-layer-deposited Al2O3 films for processability". In: *ACS Omega* 2.7 (2017), pp. 3390–3398.

[36] Chen Y. et al. "Weyl fermions and the anomalous Hall effect in metallic ferromagnets". In: *Physical Review B* 88.125110 (2013).

[37] Chopdekar R.V. et al. "Disorder-induced carrier localization in ultrathin strained SrRuO3 epitaxial films". In: *Journal of Applied Physics* 99.08F503 (2006).

[38] Dabrowski B. et al. "Reduced ferromagnetic transition temperatures in SrRu(1-n)O3 perovskites and Ru-site vacancies". In: *Physical Review B* 70.014423 (2004).

[39] Dauphin A. et al. "Efficient algorithm to compute the Berry conductivity". In: *New Journal of Physics* 16 (2014).

[40] Dodge J.S. et al. "Temperature-dependent local exchange splitting in SrRuO3". In: *Physical Review B* 60.10 (1999).

[41] Fang Z. et al. "The Anomalous Hall Effect and Magnetic Monopoles in Momentum Space". In: *Science* 302 (2003).

[42] Fert A. et al. "Magnetic skyrmions: advances in physics and potential applications". In: *Nature Reviews Materials* 2.17031 (2017).

[43] Fukui T. et al. "Chern Numbers in Discretized Brillouin Zone: Efficient Method of Computing (Spin) Hall Conductances". In: *J. Phys. Soc. Jpn.* 74 (2005), pp. 1674–1677.

[44] Giefers H. et al. "Phonon density of states of Sn in textured SnO under high pressure: comparison of nuclear inelastic x-ray scattering spectra to a shell model". In: *Phys. Rev. B* 74.9 (2006).

[45] Groenendijk et al. "Berry phase engineering at oxide interfaces". In: *arXiv preprint* (2018).

[46] Groth C.W. et al. "Kwant: a software package for quantum transport". In: *New J. Phys.* 16.063065 (2014).

[47] Grutter A.J. et al. "Evidence of high-spin Ru and universal magnetic anisotropy in SrRuO3 thin films". In: *Physical Review B* 85.134429 (2012).

[48] Herranz G. et al. "Enhanced electron-electron correlations in nanometric SrRuO3 epitaxial films". In: *Physical Review B* 67.174423 (2003).

[49] Itoh S. et al. "Weyl fermions and spin dynamics of metallic ferromagnet SrRuO3". In: *Nature Communications* 7.11788 (2016).

[50] Kan D. et al. "Epitaxial strain effect in tetragonal $SrRuO_3$ thin films". In: *Journal of Applied Physics* 113.17 (2013), p. 173912.

[51] Kaur P. et al. "Structural, electrical, and magnetic properties of SrRuO3 thin films". In: *Applied Physics Letters* 104.081608 (2014).

[52] Kim M. et al. "Intrinsic spin-orbit coupling in superconducting delta-doped SrTiO3 heterostructures". In: *Physical Review B* 86.085121 (2005).

[53] Kim S.S. et al. "Structural evolution of epitaxial SrRuO3 thin films grown on SrTiO3 (001)". In: *Journal of Applied Physics* 90.9 (2001).

[54] Klein L. et al. "Anomalous Spin Scattering Effects in the Badly Metallic Itinerant Ferromagnet SrRuO3". In: *Physical Review Letters* 77.13 (2006).

[55] Kolesnik S. et al. "Effect of crystalline quality and substitution on magnetic anisotropy of SrRuO3 thin films". In: *Journal of Applied Physics* 99.08F501 (2006).

[56] Koster G. et al. "Structure, physical properties, and applications of SrRuO3 thin films". In: *Reviews of Modern Physics* 84 (2012).

[57] Kunkemöller S. et al. "Magnetic anisotropy of large floating-zone-grown single-crystals of SrRuO3". In: *Crystal Research and Technology* 51.4 (2016), pp. 299–305.

[58] Liu C.-X. et al. "The quantum anomalous Hall effect: theory and experiment". In: *Annual Review of Condensed Matter Physics* 7 (2016), pp. 301–321.

[59] Liu J. et al. "Mechanically Tunable Magnetic Properties of Flexible SrRuO3 Epitaxial Thin Films on Mica Substrates". In: *Advanced Electronic Materials* 4.1700522 (2018).

[60] Lu D. et al. "Synthesis of freestanding single-crystal perovskite films and heterostructures by etching of sacrificial water-soluble layers". In: *Nature Materials* 15 (2016), pp. 1255–1261.

[61] Mathieu R. et al. "Determination of the intrinsic anomalous Hall effect of SrRuO3". In: *Physical Review B* 72.064426 (2005).

[62] Matsuno J. et al. "Interface-driven topological Hall effect in SrRuO3-$SrIrO_3$ bilayer". In: *Science Advances* 2.7 (2016).

[63] Nagaosa N. et al. "Anomalous Hall effect". In: *Reviews of Modern Physics* 82 (2010), pp. 1539–1592.

[64] Ohuchi Y. et al. "Electric-field control of anomalous and topological Hall effects in oxide bilayer thin films". In: *Nature Communications* 9.213 (2018).

[65] Onoda S. et al. "Intrinsic Versus Extrinsic Anomalous Hall Effect in Ferromagnets". In: *Physical Review Letters* 97.126602 (2006).

[66] Orgiani P. et al. "Strain effect on transport properties of SrRuO3 films grown by laser MBE". In: *The European Physical Journal B* 26 (2002), pp. 23–28.

[67] Pi L. et al. "Exchange bias-like phenomenon in SrRuO3". In: *Applied Physics Letters* 88.102502 (2006).

[68] Psiuk B. et al. “SrTiO3 surface modification upon low energy Ar bombardment studied by XPS”. In: *Vacuum* 131 (2016), pp. 14–21.

[69] Qin Q. et al. “Emergence of Topological Hall Effect in a SrRuO3 Single Layer”. In: *Advanced Materials* 31.1807008 (2019).

[70] Roy D. et al. “Field tuning of domain-wall type and chirality in SrRuO3”. In: *Physical Review B* 9.224437 (2017).

[71] Shimizu S. et al. “Gate tuning of anomalous Hall effect in ferromagnetic metal SrRuO3”. In: *Appl. Phys. Lett.* 105.163509 (2014).

[72] Siemons W. et al. “Dependence of the electronic structure of SrRuO3 and its degree of correlation on cation off-stoichiometry”. In: *Phys. Rev. B* 76.075126 (2007).

[73] Singh D.J. et al. “Electronic and magnetic properties of the 4d itinerant ferromagnet SrRuO3”. In: *Journal of Applied Physics* 79.4818 (1996).

[74] Sinwani O. et al. “Monitoring superparamagnetic Langevin behavior of individual SrRuO3 nanostructures”. In: *Physical Review B* 89.020404(R) (2014).

[75] Sohn B. et al. “Emergence of robust 2D skyrmions in SrRuO3 ultrathin film without the capping layer”. In: *arXiv preprint 1810.01615v1* (2018).

[76] Talbi F. et al. “Dielectric breakdown characteristics of alumina”. In: *2010 10th IEEE International Conference on Solid Dielectrics* (2010).

[77] Teodorescu C.M. et al. “Band ferromagnetism in systems of variable dimensionality”. In: *Journal of Optoelectronics and Advanced Materials* 10.11 (2008).

[78] Thouless D.J. et al. “Quantized Hall conductance in a two-dimensional periodic potential”. In: *Physical Review Letters* 49.405 (1982).

[79] Tokura Y. et al. “Emergent functions of quantum materials”. In: *Nature Physics* 13 (2017), pp. 1056–1068.

[80] Toyota D. et al. “Ferromagnetism stabilization of ultrathin SrRuO3 films: thickness-dependent physical properties”. In: *Journal of Applied Physics* 99.08N505 (2006).

[81] Tyagi S. et al. “Strain healing of spin-orbit coupling: a cause for enhanced magnetic moment in epitaxial SrRuO3 films”. In: *arXiv:1901.00613v1* (2019).

[82] Wang X. et al. “Fermi-surface calculation of the anomalous Hall conductivity”. In: *Physical Review B* 76.195109 (2007).

[83] Xiao D. et al. “Berry Phase effects on electronic properties”. In: *Reviews of Modern Physics* 82.3 (2010), pp. 1959–2007.

[84] Yang W.-H. et al. “LaAlO3 single crystal substrate for epitaxial superconducting thin films”. In: *Solid State Communications* 75.5 (1990), pp. 421–424.

[85] Zhong Z. et al. “Theory of spin-orbit coupling at LaAlO3-SrTiO3 interfaces and SrTiO3 surfaces”. In: *Physical Review B* 87.161102(R) (2013).

[86] Caviglia lab. “Angle-dependent field measurements, in the works.” In: ().

# ACKNOWLEDGEMENTS

A big thanks to Caviglia lab for this fabulous opportunity. Thank you Andrea for letting me join in and for the many fascinating discussions. I suspect the passion I felt for this project is due in no small part to your own strong enthusiasm to lead a field and explore new physics. Thank you Thierry for being an great supervisor, I'm very grateful that you always made sure I had realistic expectations for the physics we were studying, I couldn't have asked for better guidance. Many thanks to Edouard for enlightening discussions, and to Dima, Jorrit and Mattias as well; the future of Caviglia lab is bright.

Thank you to my committee members for reading this thesis and agreeing to ask me questions about it, I look forward to it. Thank you as well to my family for (implicitly) agreeing to read this, I will send some paracetamol for the headaches.

I would like to acknowledge Christian Prosko for acknowledging me in his thesis. Thank you for being an amazing person and an inspiration to me. We make a great team, and I look forward to our future together; what can I say but I love you.